Chapter 2

Experimental details and measurement techniques

In this chapter we introduce and describe the two beamlines used to carry out the present positron scattering measurements, as reported in the following chapters. Also discussed are the experimental techniques and measurement procedures of each apparatus, along with the methods and corrections usually employed to analyse and finalize the gathered raw data. We first focus our discussion on the positron spectrometer at the University of Trento, used to measure nearly all the total cross sections for positron scattering from the targets investigated as part of this thesis. Subsequently, we describe the atomic and molecular buffer-gas trap and beam apparatus at the Australian National University.

2.1 PAIS apparatus (University of Trento)

The positron spectrometer (PAIS) in the Atomic and Molecular Physics Laboratory at the University of Trento (Italy), is a linear transmission apparatus based on a beam intensity attenuation technique (Bederson and Kieffer, 1971) for total cross section measurements of positron and electron scattering from atoms and molecules. The idea of building this apparatus and its design date back to the late 1990's (Zecca, 1998-1999, unpublished). It was then assembled in its present form in the following years by Prof. Antonio Zecca and his collaborators (Karwasz *et al.*, 2000). At that time a good range of total cross section measurements where available in the literature (see, for instance, Kauppila and Stein, 1990; Kimura *et al.*, 2000), nevertheless, the technologies for slow positron beam production and handling had improved a lot since those pioneering studies (Zecca, 1995; Brusa *et al.*, 1997; Zecca *et al.*, 1995): so it was possible to plan experiments with an in principle better performance. At the same time, the development in theoretical techniques was such that more accurate measurements were needed to test the theories (Surko *et al.*, 2005).

The apparatus that was built and tested in the early years in the Trento laboratory (Karwasz *et al.*, 2000), was subsequently further developed and

its description provided in this chapter refers to the present status of the spectrometer.

The Trento spectrometer was designed to measure total cross sections in the energy range ~0.1-150 eV, and with an energy resolution of a few tenths of an eV. The very low energy range (below ~1 eV) is still practically unexplored in positron scattering experiments, except for just a few measurements (see, for instance, Kauppila *et al.*, 1981 and references therein). In addition the energy range below a few tens of eV is thought to be the most interesting, because it is where many of the physical processes involving the incoming positrons and the target molecules occur, namely positronium formation, direct ionisation and the discrete excitation of electronic states, just to mention a few of the most important. On the theory side of things, calculations going down in energy to well below ~1 eV, for quite a few targets (e.g. H_2, N_2, CO and C_2H_2), already exist in the literature (see Chapters 3 and 4). Therefore, to assist theoretical colleagues in validating the results of their models and in the development of positron scattering theory to produce accurate cross sections, it is fundamental that experimental low-energy data sets for those targets become available. Providing extensive, reliable and high resolution very low-energy total cross section data sets for important molecular and atomic targets is, indeed, among the rationales behind the work described in this thesis.

Attenuation measurements in this apparatus can technically be carried out only on species in their gaseous or vapour phase. Notwithstanding this fact, experiments can still be performed on targets that are liquid (or even solid) at room temperature, provided that their vapour pressure at that temperature is sufficiently high to provide a continuous source of gas. As we will see in the next chapters, in effect, quite a few of the present experiments have been conducted not only on a gas target, but also on species that are liquid at room temperature. Note that in the case of a target with an excessively low vapour pressure, a constant flow of vapour can still be obtained simply by heating the sample. However, none of the present measurements required further heating of the target sample.

Note also that this apparatus was originally intended not only for low-energy positron, but also electron collisions, since a positron beam can be exchanged with an electron beam, also produced by decay of a radioactive source, by simply reversing the polarities at the electrodes of the charged particle optics. However, in practice, during its entire life, the apparatus has been used only once in the electron mode, namely to measure the total cross sections of tetrahydrofuran in the range 2-21 eV (Zecca *et al.*, 2005). The energy resolution of the electron beam that can be achieved with this configuration is in fact quite poor, roughly of the order of 4 to 5 eV (Zecca *et al.*, 2005). This resolution is to be compared with that typically achieved with our experimental setup when a positron beam is in use, namely 0.1-0.3 eV, depending on the specific type of moderator employed (see Section 2.1.2). Since the Trento apparatus has been used to exclusively perform positron scattering measurements for this thesis, in the following we will limit our discussion on the apparatus and the measurement techniques to only the case when a positron beam is being employed.

2.1.1 Description of the apparatus

The configuration of the positron spectrometer in use at University of Trento is schematically shown in Fig. 2.1, and a picture can also be seen in Fig. 2.2. The apparatus is formed by a source stage, a moderator conditioning chamber, a main vacuum chamber containing the charged particle optics that transport the positron beam, the scattering region and the detection stage. By employing a radioactive source that emits fast positrons, a stage of positron energy moderation, some electrostatic optics, an axial magnetic field and a channel electron multiplier (CEM) detector, a collimated, well-focused and stable positron beam with suitable optical parameters and appropriate energy is produced, transported and then focussed into the scattering region. At this point the positrons interact (or do not) with the target molecules and are eventually detected at the exit of this region.

The apparatus consists of two main functional stages, that can be clearly distinguished in its design (see Fig. 2.1). In the first part, a beam of slow positrons is formed, whereas in the second one, a beam is prepared for the scattering experiment. A 90° electrostatic deflector decouples the source region from the scattering and detection regions.

The first stage extracts slow positrons from the moderator and, through the use of some electrostatic elements, these positrons are accelerated to form a positron beam at the exit plane of an electrostatic hemispherical deflector with an energy of 160 eV. From this exit plane, the positrons are then transported and focussed by the second stage (see Fig. 2.1) into the scattering region. As most of the high-energy positrons emitted by the radioactive source are able to pass through the moderator without being moderated, the main role of the deflector is to remove these high-energy positrons from the beam, in order to reduce the background at the detector. This is achieved as the high-energy positrons are not deflected and subsequently annihilate in a “dump cage” present inside the deflector.

The second stage of the spectrometer is intended to prepare the beam for the desired scattering process by means of some electrostatic optics and an axial magnetic field, that are appropriately set in order to guide the positrons towards and throughout the scattering region. In this section of the apparatus, in fact, a stable and well-focused (into the scattering region) positron beam, with the desired energy and shape characteristics, that is also tuneable over a fairly broad energy range, is formed. The apparatus in its current configuration was designed to achieve good positron beam characteristics for beam energies in the range ~0.1-150 eV. However, in general, most of the measurements have been made at energies below ~50 eV, since that is where we expect the positron-related physics is likely to be most interesting.

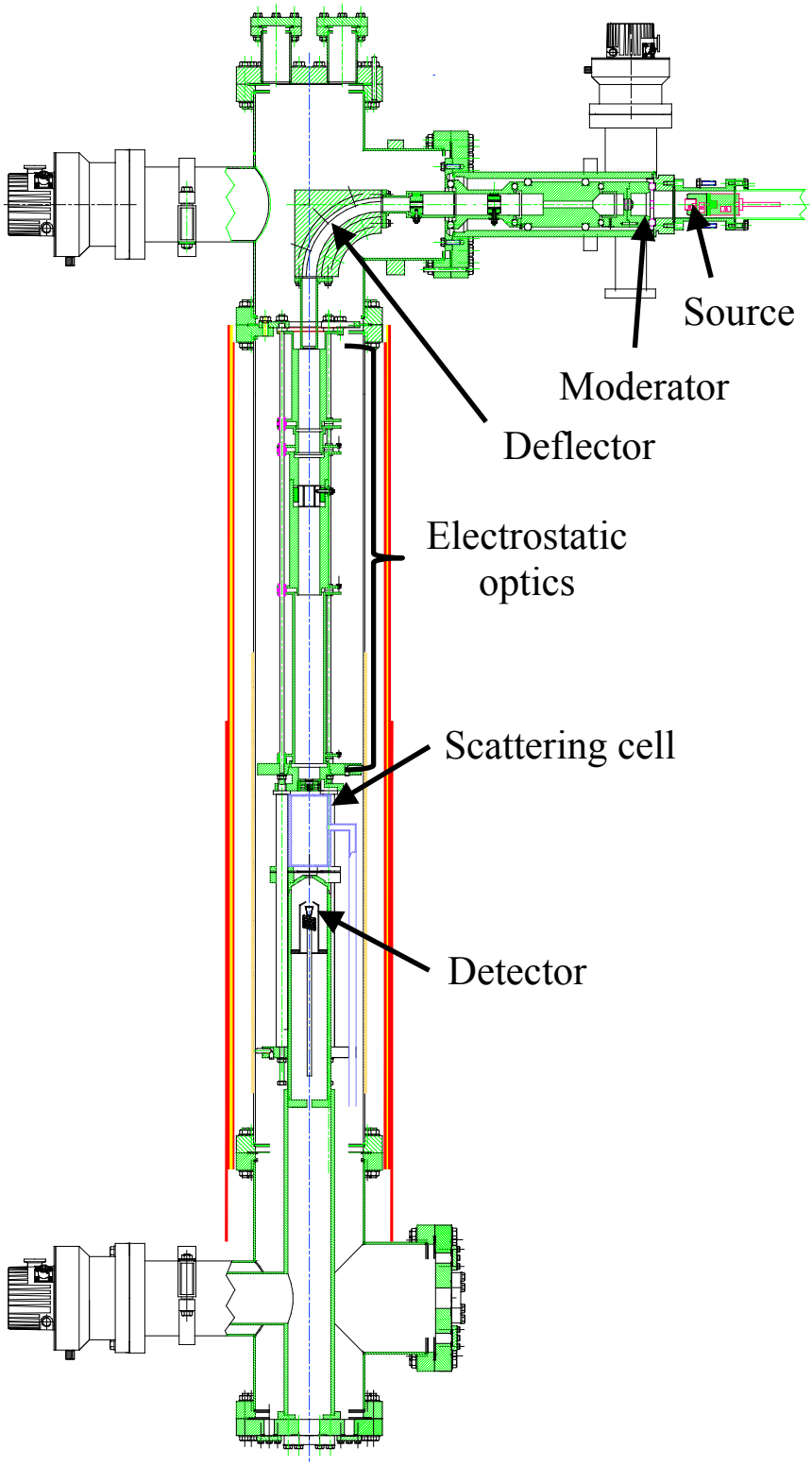

Fig. 2.1. Schematic design for the configuration of the positron apparatus at the University of Trento. The positron source, the moderator, the hemispherical deflector, the set of electrostatic optics, the scattering cell and the channel electron multiplier detector can be clearly seen.

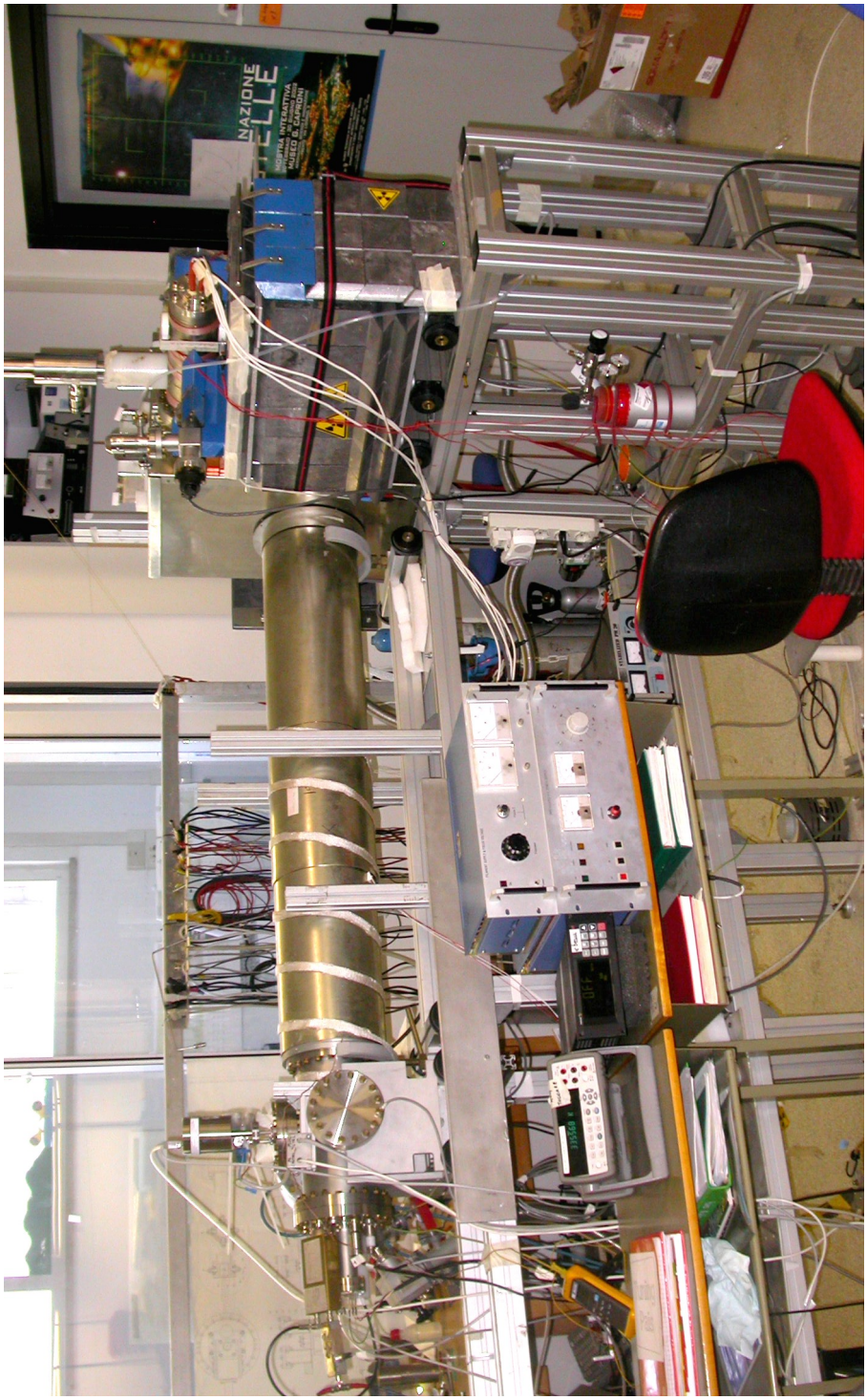

Fig. 2.2. Photograph of the positron spectrometer at the University of Trento. The sections of the apparatus, corresponding to the different stages, can be clearly observed. From right to left: the radioactive source and initial positron beam are hidden in a lead shielding; the deflector section is in the magnetic shield box behind the lead; the moderator conditioning chamber is on top of the lead bricks; the positron transport system, the scattering chamber and the detection region are inside the long cylindrical magnetic shield.

As this second section of the apparatus was designed to reach very low energies (Zecca, 2011, private communication), it is worth noting that, when planning a scattering cell experiment, some kind of low energy border is imposed by the Doppler broadening of the equivalent energy distribution of the positron beam. With the gas cell at room temperature the broadening depends on the thermal speed of the target molecules/atoms: the largest broadening is for lighter gases (~0.028 eV for helium). Even with large molecules the practical limit of gas cell experiments is in the meV range: should a measurement be planned at lower energies, a crossed beam configuration would be needed. The crossed beam approach requires much higher positron fluxes, which are still now very difficult to achieve with the present primary β^+ sources. Overall, at the time in which this spectrometer was designed, a 0.1eV lower limit for the energy range was an ambitious goal.

As in any spectrometer, a flat transmission function (see Section 2.1.2.2) is highly desirable: it is known that an ideally flat transmission function produces no distortion on the measured cross section. This requirement conflicts with the Helmholtz-Lagrange law for charged particle beams. This law states that along a positron beam path where current is conserved, the energy E, the differential solid angle $d\Omega$ subtended by the elevation angle θ and the differential beam area dA at any two beam cross sections labelled "1" and "2" are related by (see for instance Kuyatt and Simpson, 1967 and references therein):

$$E_1 d\Omega_1 dA_1 = E_2 d\Omega_2 dA_2 \tag{2.1}$$

An alternative form (King, 1995) is of more direct use when dealing with beam sections at conjugated planes, i.e when the subscripts 1 and 2 relate to planes which are images one of the other:

$$\sqrt{E_1}\theta_1 R_1 = \sqrt{E_2}\theta_2 R_2 \tag{2.2}$$

In Eq. (2.2) R_1 and R_2 are the beam radium at planes 1 and 2, respectively.

As an example, we can apply Eq. (2.2) to calculate the ratio of the positron current at 0.1 eV (scattering cell) to the current at 160 eV (positron energy at the exit of the deflector). Let us make the assumption that $R_1 = R_2$, i.e. the magnification from the deflector to the entrance of the scattering chamber is unitary. We also assume a unitary angular magnification $\theta_1 = \theta_2$. Both these assumptions are close to the real design values of the Trento spectrometer. We find that the maximum current that can reach the scattering chamber entrance aperture is 1600 times smaller than the current exiting the deflector. Various losses lead to a real ratio of the order of 2000 to 3000. This result allows us to explain an important detail of the design criteria used for the Trento spectrometer. Willing to achieve a relatively flat transmission function over the entire energy range from 0.1 to 50 eV, the only way to obey the Helmholtz-Lagrange law is to have a low counting rate over the entire range.

2.1.1.1 The source stage

The positrons used in our scattering experiments are produced by a ^{22}Na radioactive source with a 3 mm spot size (see Fig. 2.3). These positrons are emitted as the product of a β^+ radioactive decay reaction of a ^{22}Na unstable isotope, turning into a ^{22}Ne nucleus:

$$^{22}_{11}Na \rightarrow {}^{22}_{10}Ne + e^+ + \nu_e + \gamma. \tag{2.3}$$

Also released in the decay process are gamma rays with an energy of 1.27 MeV (Endt, 1990) and electron neutrinos. Note that nearly 10% of the ^{22}Na nuclei usually decay via electron capture and, therefore, do not emit positrons at all (Allen *et al.*, 1955).

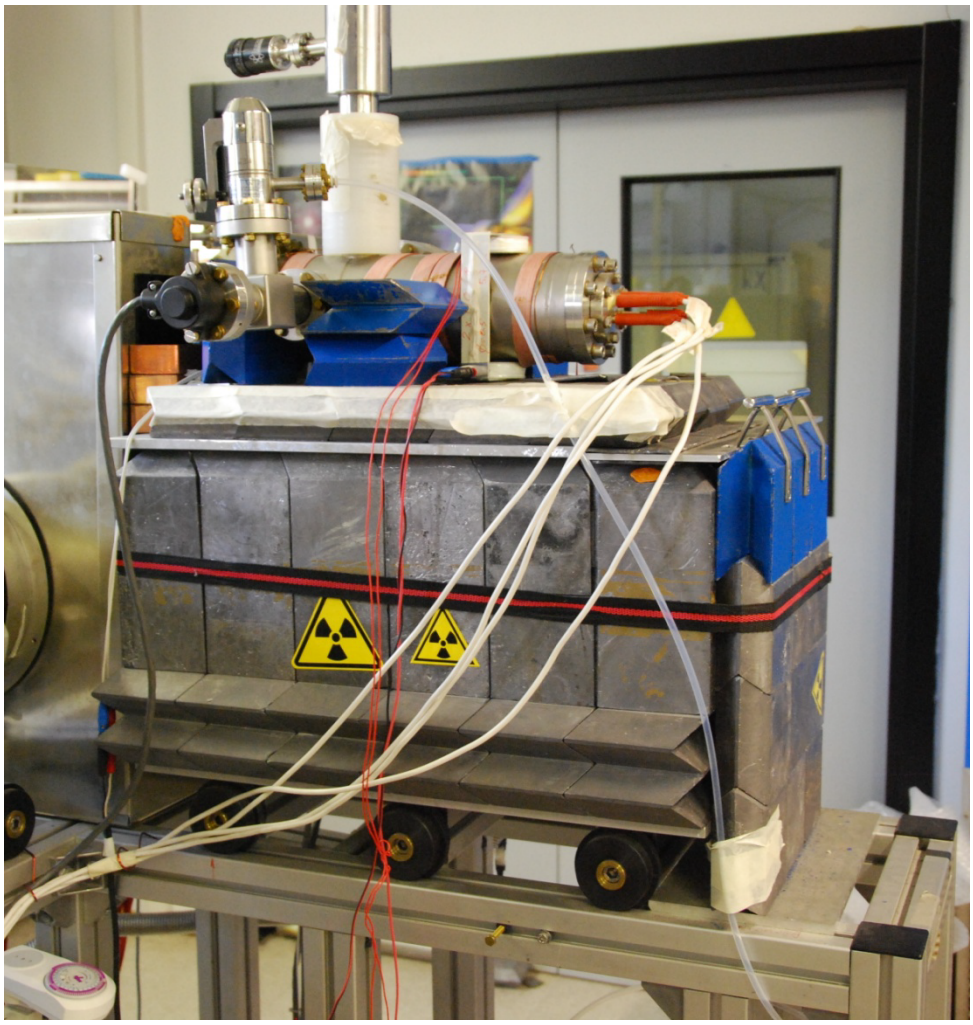

Fig. 2.3. Detail of the first stage of the positron spectrometer at the University of Trento. The assembly containing the radioactive source and the first positron optics are enclosed in a 12 cm thick lead shield. The conditioning chamber sits atop it. The manipulator, which allows one to move the moderator from the conditioning chamber to the fast positron beam, is clearly visible.

The half-life of the ^{22}Na isotope is known to be approximately $t_{1/2}$ = 2.6 years (Audi *et al.*, 2003). When purchased in mid-1999 (t_0 = 1999.5 years), the radioactive source currently employed in the Trento spectrometer had an activity of $A_0 \approx 30$ mCi. The decay of the ^{22}Na isotope can be described by an exponential process which obeys first-order kinetics:

$$A(t) = A_0 e^{-t/\tau} = A_0 (1/2)^{(t-t_0)/t_{1/2}}, \tag{2.4}$$

where $A(t)$ is the activity of the radioactive source in mCi at time t (years) and $t_{1/2} = \tau \ln 2$. By using Eq. (2.4), it is therefore possible to calculate the activity of the radioactive source as a function of time. The results of this computation are shown in Fig. 2.4, where it can be clearly seen that the residual activity of the source is currently only slightly higher than 1 mCi and is predicted to drop below the 1 mCi threshold by the middle of the first semester of 2012.

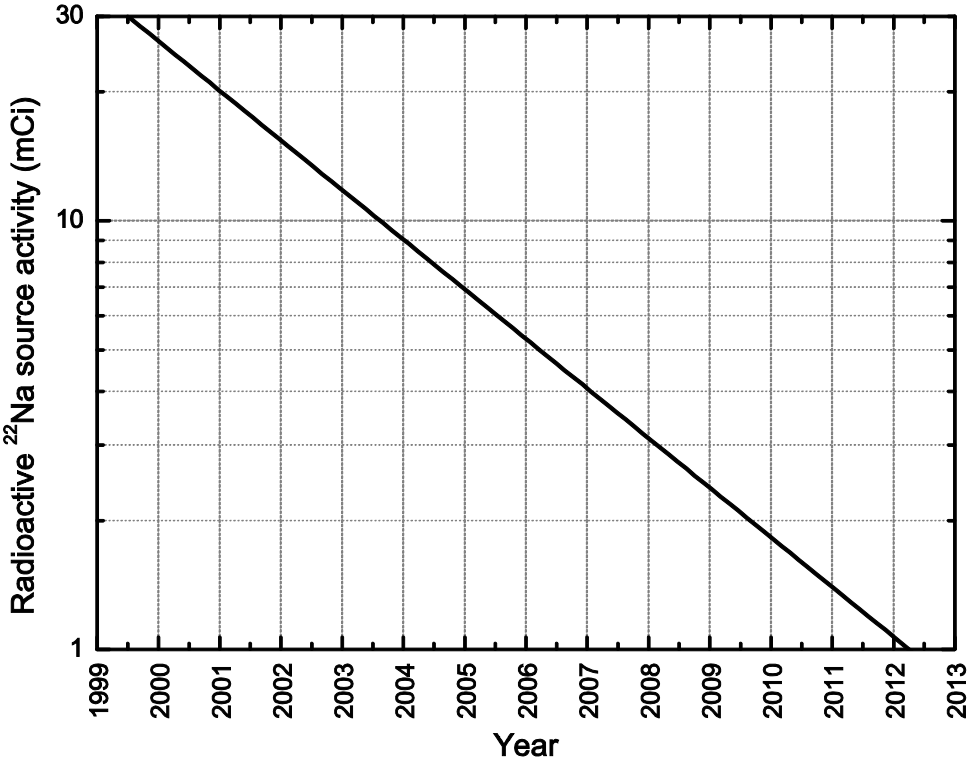

Fig. 2.4. Activity of the radioactive ^{22}Na source of fast positrons, employed in the spectrometer at the University of Trento, as a function of time (years). Note the log-scale on the y-axis.

The positrons are emitted by the source in all directions, with the typical β^+ decay spectrum, with an end point of about 546 keV. However, this energy spectrum is not suitable for the low energy scattering experiments that we are interested in. Therefore, these fast positrons need to be first slowed down in energy and "shrunk" in distribution before effectively being

employed. Currently, the most effective method of producing a slow and high resolution beam from a flux of fast positrons is a moderation procedure. This technique consists of placing a thin film of moderating material in front of the radioactive source (i.e. in a transmission geometry). The moderators typically used in low energy positron scattering experiments are thin foils of tungsten or nickel. These films are usually mono-crystals and have a thickness of just a few μm. The fast positrons emitted by the radioactive source rapidly thermalize within the moderator by losing energy in the collisions with the atoms. A small fraction of the incident positrons is eventually reemitted by the film, with a kinetic energy that depends on the specific negative positron work function of the material, that the moderator is made of, and on the moderator temperature. The electron (positron) work function $\Phi^-(\Phi^+)$ for a solid is defined as the minimum energy needed to remove an electron (positron) from the Fermi level to a point in vacuum that is immediately outside the influence of the solid (Gersten and Smith, 2001). Tungsten is known to have a positron work function ranging approximately from $\Phi^+ = -2.5$ eV to $\Phi^+ = -3.0$ eV, depending on many parameters (e.g. the microscopic conditions of the moderator surface and related contaminants), whereas that of nickel is found to be $\Phi^+ = -1.5$ eV (Hugenschmidt *et al.*, 2002). As a result, positrons are re-emitted by the moderator with an energy generally in the eV range (Zecca, 2002) and therefore they can be used for scattering experiments. In addition, the energy distribution of the moderated positrons turns out to be in the sub-eV range. Typical values reported in the literature for the full width at half maximum (FWHM) energy spread that can be achieved with a moderation process are $\Delta E \approx 0.3$ eV for nickel foils and $\Delta E \approx 0.6$ eV for annealed tungsten films (see e.g. Hugenschmidt *et al.*, 2002).

Note that while slow positrons are the main output of a moderator placed in front of the radioactive source, the same assembly generates simultaneously secondary electrons as the result of the high-energy positrons slowing down in the moderator. If needed, these secondary electrons can be used to produce an electron beam.

2.1.1.2 The moderator conditioning chamber

We have seen that low energy monoenergetic positron beams can be produced by employing a radioactive source of fast positrons in conjunction with a thin tungsten or nickel film. However, not every kind of metallic foil is suitable to act as a positron moderator. Efficient moderator materials must have a high diffusion length for positrons, this increases their probability to reach the surface, and a negative positron work function, leading to a positron emission with a certain kinetic energy (Hugenschmidt *et al.*, 2002). Since the diffusion length decreases with increasing defect concentration in the microscopic structure of the material, that is, with more positron traps, the moderation material should ideally be defect free (Hugenschmidt *et al.*, 2002). This situation of microscopic order at the atomic level can be achieved initially by exposing the material to sufficiently high temperatures and then by gradually decreasing the temperature (see Section 2.1.2.1). This very slow cooling process should normally let the atoms relax to positions

corresponding to their absolute energy minima, such as to form crystal-like structures, and avoid any possible stress in the microscopic configuration of the material or prevent the formation of structural defects. The multistep procedure of film annealing for application in positron beam production is known as moderator conditioning.

Since most of the films that can be purchased from commercial suppliers do not usually come as mono- or poly-crystal foils, annealing of the material is required, before it can be appropriately used as a positron moderator. Indeed, a few conditioning cycles are typically needed for the moderator to reach the highest emission efficiency that is achievable with that material (see Section 2.1.2.1).

The positron spectrometer at the University of Trento includes a chamber specifically designed for the in situ conditioning of the moderators (see Fig. 2.3). This chamber is on top of the source region and is oriented in a parallel position with respect to the transmission geometry. A narrow pipeline connects the main vacuum chamber to the conditioning chamber, with a valve permitting separation of the two chambers during the heat treatment. This valve is kept open during the cross section measurements. Another manual valve allows for injecting H_2 into the conditioning chamber during the treatment of the Ni moderator, as we will discuss in more detail in Section 2.1.2.1.2.

The moderator is contained in an appropriate holder made of a copper-nickel alloy (ARCAP), with a 7 mm hole which is "filled in" by the moderator film. The moderator holder is mounted on a linear feedthrough, which allows its removal from the position in front of the source into the conditioning chamber.

Heating and thermal annealing of the moderator, in the conditioning chamber, is achieved with an electron beam produced by an electron gun. Electrons, with typical energies in the range 1-6 keV, are produced via thermoionic emission from a tungsten filament placed at the left end of this gun. The electron beam is then transported towards the moderator, which is situated at the right end of the chamber, by means of some electrostatic optical elements. These electrons are implanted onto the film face opposite to that where the positrons are re-emitted, in order to reduce radiation damage and related defects close to the emitting surface. During the electron bombardment, the film temperature has occasionally been measured with an optical pyrometer. However these measurements turned out to be somewhat problematic, with possible errors larger than 300 °C. Note that we believe the electron bombardment can achieve film temperatures on the order of 2000 °C. This electron gun allows concentrating electrons on a spot smaller than 4 mm in diameter.

Fig. 2.5 shows the typical result of a ray-tracing simulation, for the moderator electron beam, as obtained with the software SIMION (Manura and Dahl, 2008). Table 2.1 gives some typical operational values for the potentials on the four electrostatic elements forming the electron gun; these voltages have been used for the ray-tracing. In that simulation three groups of five electrons each leave the tungsten filament (at the left end of Fig. 2.5) with an initial kinetic energy of 1 eV, from three different positions along

the y-axis: -0.5 mm (red group), 0 mm (green group) and +0.5 mm (blue group). In every group each of the five electrons start with a different elevation angle of 0°, ±15° and ±30° with respect to the x-axis. It can be clearly seen from Fig. 2.5 that the resultant electron beam is well-focussed onto the moderator, whose position with respect to the electron gun is indicated by the two vertical ticks at the right end of Fig. 2.5. Note that the diameter of the electron beam spot at the moderator is indeed only ~1 mm in this specific case. Further note that care must be exercised to avoid evaporating the moderator.

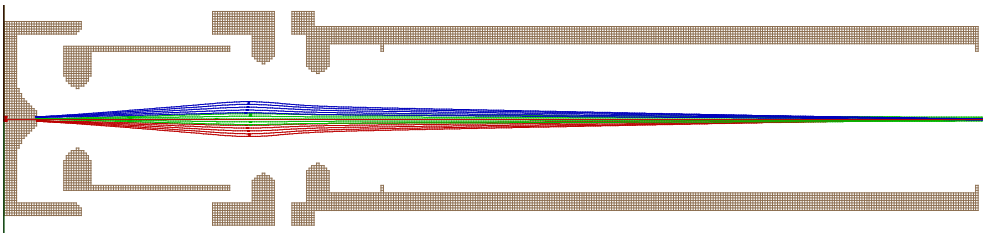

Fig. 2.5. Simulation of the electron beam ray-tracings for the moderator electron gun, as carried out with the software SIMION (Manura and Dahl, 2008) and by using the potentials of the electrostatic elements reported in Table 2.1. Cylindrical symmetry is to be assumed. Scale: 1 grid unit = 0.5 mm.

Table 2.1. Typical values of the potentials on the electrostatic elements in the electron gun, as used to produce a collimated and well-focussed electron beam onto the moderator film. All potentials are referred to earth.

Electrostatic element	Potential (V)
1	0
2	1050
3	0
4	5000

2.1.1.3 The vacuum system

The entire spectrometer is made from a non-magnetic copper-nickel alloy, while the vacuum chamber, flanges and other fittings are fabricated from AISI 316L stainless steel. The entire apparatus is shielded by an external μ-metal box, with an additional double cylindrical shield around the second stage of the apparatus reducing the stray magnetic fields to below 1×10^{-7} T in the scattering cell region.

Three turbomolecular pumps are used to achieve and maintain the vacuum in the system (see Fig. 2.1). Two small Varian TV 301 Navigator pumps (model 969-8919, N_2 pumping speed 250 l/s, rotational speed 56,000 rpm) are located at the conditioning chamber and at the hemispherical deflector, respectively. One larger Varian Turbo-V 1000HT pump (model 969-9075, 950 l/s, 38,000 rpm) is situated close to the scattering cell, to

create and maintain the vacuum in the scattering chamber and the detector region. The two small turbo pumps are coupled to an Edwards RV12 rotary pump (maximum pumping speed 12 m^3/h, motor rotational speed 1470 rpm, ultimate total pressure 2×10^{-3} mbar), whereas the Varian Turbo-V 1000HT pump is coupled to an Alcatel rotary vane pump (28 m^3/h). The multistage rotary vane pumps alone generate a vacuum in the system of the order of 2-5 $\times 10^{-3}$ mbar, as measured at each end station with an Edwards APG100 Active Pirani Vacuum Gauge (accuracy ±15%) connected to a Multi Gauge controller.

The pressure in the vacuum system is measured in the scattering chamber and in the conditioning chamber with two respective ionisation gauges, each one being linked to a Varian L8350301 Multi Gauge Controller Unit (electrometer accuracy $<10^{-10}$ Torr). When all the turbo pumps are on and fully operative, and in the absence of the target gas, the background pressure in the scattering chamber is usually in the high $\times 10^{-8}$ Torr or low $\times 10^{-7}$ Torr range. In the conditioning chamber the base pressure is typically in the low $\times 10^{-9}$ mbar range, with the decoupling valve closed, and increases up to high $\times 10^{-9}$ mbar or low $\times 10^{-8}$ mbar, when that valve is open.

2.1.1.4 The scattering region

After being transported by a set of electrostatic optics, the moderated positron beam collides with the molecules or atoms of the target. This happens in the scattering region, which consists of a scattering cell, with small circular apertures, into which the target gas of interest is admitted during the attenuation measurements. To help focus the positron beam into the scattering cell through the entrance aperture, the scattering chamber section of the apparatus is wrapped in a coil which produces a weak axial magnetic field parallel to the beam axis. The solenoid is powered by a DC power supply, with typical currents of ~0.7-2 A with a stability better than 1 $\times 10^{-3}$ A. This coil generates a magnetic field of 6 G for each 1 A of current, therefore the intensity of the magnetic field is usually in the range ~4-12 G. However, depending on the specific set of potentials on the electrostatic elements and on the energy range of the measurement, this value can vary significantly from experiment to experiment in order to obtain the best shape and characteristics of the positron beam and the highest positron count rate.

The scattering cell originally employed in the Trento apparatus had a geometrical length of 100 ± 0.1 mm. However, a few years ago this cell was replaced with a shorter one (22.1 ± 0.1 mm), which is still in use today. Note that all the measurements described in this thesis have been undertaken with the short cell in the experimental setup, except for those on 3-hydroxy-tetrahydrofuran. The scattering cell has an entrance and exit aperture, both of 1.5 mm diameter.

The storage vessel containing the sample, of the target of interest, is generally a standard metallic gas bottle or a metallic cylinder, depending on whether the state of the target is gaseous or liquid at room temperature, respectively. This container is coupled to the apparatus gas handling system via a MKS 170M-45 leak valve, and its MKS 170M-48A controller, that

allows for setting the amount of gas or vapour to be injected into the scattering chamber for a proper attenuation measurement. A set of teflon pipes, of 10 mm diameter, connects the leak valve to the scattering cell and the scattering section of the vacuum system. In addition, a two-way diverter valve controls the gas flow: the same amount of gas is routed to the scattering cell or, alternatively, is diverted directly into the vacuum system, depending on the stage of the measurement. In the first case, the attenuation of the positron beam is measured, while in the second case it provides a measurement of the positron count rate in the absence of the target gas. Such a provision makes sure that the background pressure outside the gas cell, and therefore the attenuation of the beam in the path outside the scattering cell, is the same irrespective of the particular stage of the measurement cycle. This in turn means that the measurements estimate correctly the positron beam attenuation that actually takes place only in the scattering cell. This precaution minimizes also any effects of the gas on the electrostatic lens behaviour and any possible influence on the moderator emission properties. The background pressure in the vacuum system, during the measurements, is typically 10^{-3}-10^{-4} of the pressure inside the scattering cell, when the target gas is admitted to it. In fact, the actual pressure in the scattering cell, when the target gas is routed to it, is usually in the mid-high 10^{-4} Torr range.

The pressure in the scattering cell is measured with either a MKS Baratron capacitance manometer model 627B (1 mbar full scale), which operates at 45 °C or, alternatively, an MKS Baratron capacitance manometer model 628B (1 Torr full scale) operated at 100 °C. The capacitance heads are operated at a temperature higher than room temperature in order to minimise the drift of the pressure zero. We typically observed drifts smaller than 10^{-4} mbar. A teflon pipeline of 10 mm diameter links the manometer directly to the scattering cell. Note that both MKS Baratron manometers are rated to very high stability by the manufacturer, and we have performed extensive tests to confirm the veracity of that claim.

The temperature of the target gas in the scattering cell is measured by a calibrated platinum (PT100) resistance thermometer that is in excellent thermal contact with the scattering chamber. This is considered to provide a good approximation of the target gas temperature, because, in our geometry, gas molecules thermalise with the scattering cell walls. As the area of the entrance and exit apertures is much smaller than the whole surface of the scattering cell and given that the molecule mean free path is greater than the cell length, a molecule is expected to hit several times the chamber walls before exiting the cell. These multiple collisions ensure that full thermalisation occurs. Note that the scattering chamber, and so the target gas, was always maintained at room temperature (~24 ± 2 °C) during the measurements undertaken for this thesis.

2.1.1.5 The detection stage

After having interacted (or not) with the target molecules or atoms, the positrons eventually exit the scattering cell and pass through an aperture of diameter 2 mm, situated 8 mm downstream of the scattering cell, before

colliding with a positron detecting device. This aperture acts as a skimmer-like diaphragm, reducing the gas pressure at the detector. At the same time, it also decreases the angular acceptance of the detector and, therefore, aids in reducing the angular resolution error affecting our measurements (see Section 2.1.3.4 for more details).

A retarding potential analyser (RPA) (Simpson, 1961) is also positioned post-scattering cell, in order to measure the positron count rate at the detector as a function of the positron beam energy (see Section 2.1.2.2). In the present apparatus the RPA device is a single-grid retarding potential system (Simpson, 1961).

The ion detector employed to count the positrons in the Trento spectrometer is a single channel electron multiplier (CEM), sited in a cup (Fig. 2.6) positioned downstream of the skimmer aperture. In general, an electron multiplier is a vacuum-tube containing many discrete multiplying electrodes called dynodes. If the energy of a charged particle incident on the first dynode is high enough, it can trigger the multiple emissions of secondary electrons from its surface (Allen, 1939; 1947). By applying increasingly positive electric potentials to the successive dynodes, the emitted electrons accelerate to the next electrode and cause secondary emission of even more electrons. This process can be repeated many times and as a result an electron shower can then be collected by a separate anode electrode.

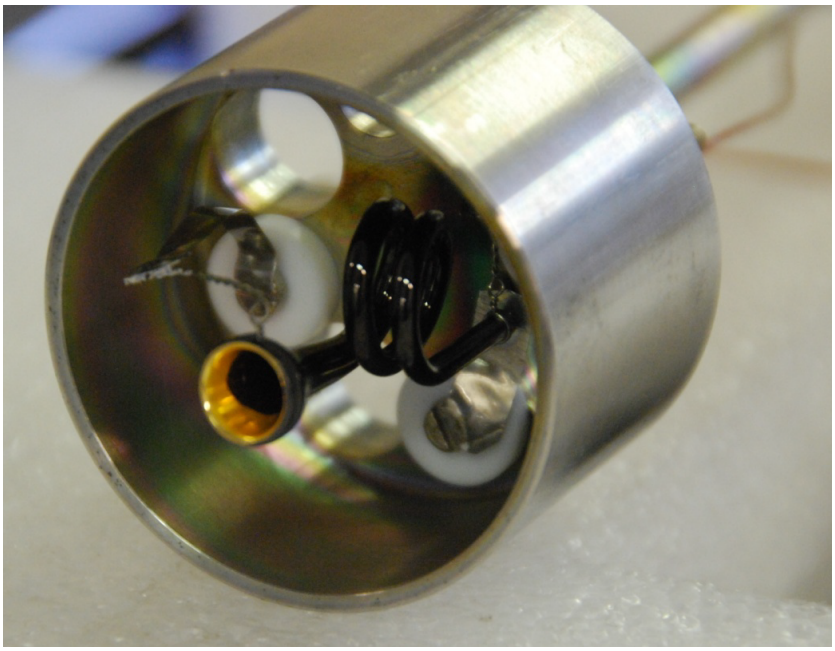

Fig. 2.6. Picture of the cup containing the channeltron used to detect the positrons.

A so-called single channel electron multiplier (commonly named a channeltron) consists of a narrow tube of glass coated internally with a thin film of semi-conducting material (see Fig. 2.6), that is the electron emissive

material. At one of its two ends, the tube widens in breadth to become a small cone (i.e. assumes a funnel-like shape, see Fig. 2.6), in order to aid the collection of the incoming charged particles with slightly different impacting angles. The other end of the tube is "coiled up" to form a spiral structure. In a channeltron, the dynodes form a continuous structure thanks to the particularly high resistance characterising the semi-conducting film (Heroux and Hinteregger, 1960). The electrons emitted at any point in the tube are accelerated a relatively short distance further down the tube, before impacting again against another side of its surface. In order to sustain the electron avalanche, a negative high voltage needs to be applied at the cone of the channeltron and a positive voltage near ground at the spiral output end.

In the experimental configuration in use in Trento, the potential at the two ends of the channeltron is provided by a stabilised high voltage power supply. A typical high voltage of AC = +2,600 V, with respect to ground, is applied to the rear of the channeltron (see Fig. 2.16) to amplify the positron signal. In addition, a smaller potential AP = -200 V is applied directly at the base of the channeltron funnel (see again Fig. 2.16), in order to attract the positrons leaving the scattering cell and moving towards the detector entrance.

The positron signal produced by the channeltron is then further intensified in amplitude, by a preamplifier circuitry coupled to an amplifier. An amplitude threshold discriminator, placed downstream of the amplification stage, is appropriately adjusted in order to remove any possible electrical noise that may be influencing the measurement and to make sure that only the positron signal of interest is being "picked up". Finally, the positron pulse is counted by a timer-counter. The shape and amplitude of the positron pulses is also periodically checked with an oscilloscope.

2.1.1.6 Computer control

The measurement procedure associated with the apparatus at the University of Trento is entirely controlled by a personal computer. The code for the data acquisition, instruments control, analysis and signal processing, was developed at the University of Trento and is written in an event-driven ANSI C programming environment within the software LabWindows/CVI by National Instruments (see http://www.ni.com/lwcvi/). In conjunction with an interface hardware board by National Instruments, connecting the computer to the various instruments, the software enables us to simply read and/or control and set the parameters of the different instruments. These tasks include many of the automatic routine functions required to complete a measurement cycle and also include gathering the relevant data needed to calculate the scattering cross sections of interest. The following operations, for instance, are entirely computer-controlled:

- control and set the positron energy with a digital-to-analog converter (DAC);

- control and set the current of the solenoid generating the magnetic field in the scattering region;
- read the pressure measured by the Baratron in the scattering cell;
- read the positron count rate measured by the channeltron together with the amplifier and the threshold discriminator;
- control the pressure of the target gas in the scattering cell by means of a leak valve that regulates the amount of gas to be admitted into the scattering chamber in order to achieve the desired beam attenuation;
- read the temperature of the target gas in the scattering cell, as measured by the platinum resistance thermometer.

2.1.2 Experimental techniques and measurement procedures

In this section we describe the experimental techniques and the measurement procedures employed at University of Trento, in order to achieve scattering cross section measurements with the positron spectrometer. These include the recipes for the successful conditioning of the moderators, producing and transporting a collimated and stable beam of low-energy mono-energetic positrons, accurately calibrating the positron beam energy scale, correctly evaluating the energy resolution of the positron beam and the preparation of the target sample.

2.1.2.1 Moderator conditioning and positron emission properties

The production of low-energy positron beams is possible thanks to the discovery of the moderating properties of certain materials, mainly metals. A small fraction of the high-energy positrons entering a moderator are, in fact, emitted from the opposite side of the film, with a quasi-thermal energy distribution, and these moderated positrons can then be used to form a beam for the scattering experiment.

All moderating materials are characterised by a negative positron work function Φ^+, a property which enables the positrons to escape from their surface. The positron work function of a certain metallic material can be traced back to other physico-chemical properties of the material. In fact, it depends on a bulk contribution, the positron chemical potential μ^+ inside the metal and a surface contribution D, called the surface dipole barrier (Rubaszek, 1995):

$$\Phi^+ = -\mu^+ - D, \tag{2.5}$$

where μ^+ corresponds to the lowest energy of the positron energy band. The positron work function can also be expressed as a function of the electrochemical potential μ^- inside the metal and the electron work function Φ^-:

$$\Phi^+ = -(\mu^- + \mu^+) - \Phi^-, \tag{2.6}$$

where μ^- is equal to the absolute value of the Fermi energy E_F. Similar to the positron work function in Eq. (2.5), the electron work function is defined as:

$$\Phi^- = -\mu^- + D. \tag{2.7}$$

The fact that the moderating materials possess a negative positron work function implies that the positrons thermalising close to the surface can leave the moderator, with an average kinetic energy on the order of ~1-3 eV, depending on the material in question and its positron work function (Zecca, 2002). In addition, the FWHM energy distribution (ΔE) and the angular spread ($\Delta\theta$) of the positrons emitted from the moderator are also related to the positron work function of the material. However, we note that the chemical/physical status of the moderator surface also plays an important role in determining these operational parameters. Indeed, the work function is known to be affected by the surface layer composition, the adsorbed layers and the crystalline status of the moderator (Mills, 1995).

The performance of a given moderator is often evaluated by means of a parameter known as the "moderation efficiency" (ε_m) (Zecca *et al.*, 2010a). It is defined in Eq. (2.8) as the ratio of the number of thermal positrons emitted by the moderator (N_{out}^{mod}) to the number of high-energy positrons emitted by the source and colliding with the moderator (N_{in}):

$$\varepsilon_m = N_{out}^{mod}/N_{in}\,. \tag{2.8}$$

Note that the moderation efficiency of a moderator can be very different depending on the material and the film thickness. Fig. 2.7 shows the moderation efficiency for three different materials as a function of the foil thickness. We see that the moderation efficiency can vary by a factor of three for different substances and that the highest efficiency is usually achieved with films of thickness around 0.7 μm (Zecca, 2002).

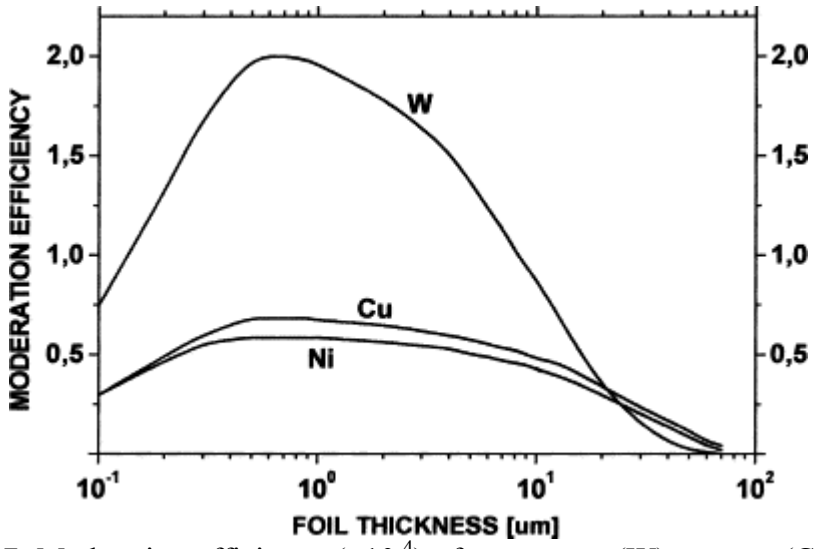

Fig. 2.7. Moderation efficiency ($\times 10^{-4}$) of a tungsten (W), copper (Cu) and nickel (Ni) moderator as a function of the foil thickness (Zecca, 2002).

While the definition of moderation efficiency appears to be quite straightforward, unfortunately it is often not feasible to directly measure ε_m in a real experiment. In most practical situations, in fact, only an overall positron beam efficiency (ε_{beam}) can be measured. The latter is defined by Eq. (2.9) as the ratio of the number of positrons reaching the detector, after having been re-emitted by the moderator and been transported by some electrostatic optics (N_{out}^{det}), to the number of high-energy positrons entering the moderator (N_{in}):

$$\varepsilon_{beam} = N_{out}^{det}/N_{in}\,. \tag{2.9}$$

Note that $N_{out}^{det} < N_{out}^{mod}$, because some of the positrons are lost during the transportation from the moderator to the detector. Hence, it is possible to define also an efficiency parameter for all the optical devices that deliver the positron beam from the moderator to the detector (ε_{opt}), which is related to ε_{beam} and ε_m via Eq. (2.10):

$$\varepsilon_{\mathrm{beam}} = \varepsilon_{\mathrm{m}} \cdot \varepsilon_{\mathrm{opt}}. \tag{2.10}$$

Typical optical transport efficiencies ranging from 40% to 80% are often achieved in linear transmission based experiments (Zecca, 2002).

From Eq. (2.10) it is clear that both the moderator efficiency and the optical transport efficiency need to be optimised in an experiment, in order to get the highest overall beam efficiency. In practice this means that both the performance of the moderator and the transmission characteristics of the charged particle transport optics have to be as good as possible, in order to maximize the number of positrons arriving at the detector. In this section we report the experimental methods employed at the University of Trento to obtain "good" moderators for application in the production of slow positron beams. We describe our standard procedures for the conditioning of both W- and Ni-moderators, that were employed for the scattering measurements undertaken as part of this thesis. We also examine the performance of these moderators, in terms of their respective ε_{beam}, ΔE, $\Delta\theta$ and operational stability and longevity. In Section 2.1.2.3 we will then discuss the electrostatic positron optics transport techniques used in the Trento spectrometer.

As we mentioned earlier in Section 2.1.1.2, annealing of a moderator is a necessary practice in order to maximize its moderation efficiency. Conditioning is achieved by heating the film with an electron beam (see Section 2.1.1.2) at high temperatures, usually not far from the melting point of the material, for a certain amount of time before subsequently bringing it back to room temperature very slowly. A slow cooling rate is essential in order to avoid mechanical stresses being induced in the cooling stage that could potentially create crystallographic defects in the microscopic structure of the material. The exposure to high temperatures has a double effect on the moderator: it aims at modifying the microscopic structure of the material by turning it into a crystalline form, and it simultaneously cleans the emitting surface of oxides and other absorbed contaminants.

In a crystalline material, such as an annealed film, the density of crystallographic defects (such as grain borders) is typically largely reduced compared to that in an amorphous compound, like a non-annealed film. A film sample might also have defects due to metal impurities. In principle high temperature annealing might enable such impurities to drift out of the sample, although we know of no studies into this effect. This means that there are typically few positron traps in the microscopic structure of an annealed film. As a consequence, the moderation efficiency of an annealed material can be much larger (by even an order of magnitude) than that of a non-annealed film (see e.g. Hugenschmidt *et al.*, 2002). This is the main advantage of employing a conditioned moderator for the production of slow positron beams.

It has previously been shown (Gramsch *et al.*, 1987; Chen *et al.*, 1985) that several consecutive conditioning cycles are normally needed to reach the optimum performance of a moderator. To validate these findings, at Trento we have tested the performance of a new moderator undergoing several conditioning treatments, which was then used for the scattering experiments. Fig. 2.8 shows the positron count rate measured by the detector, with a beam energy of 9 eV, as a function of the number of conditioning cycles for a new 1 μm-thick W-moderator. We see that the count rate seems to tend to an almost constant value after 5 to 6 treatments, therefore confirming previous observations.

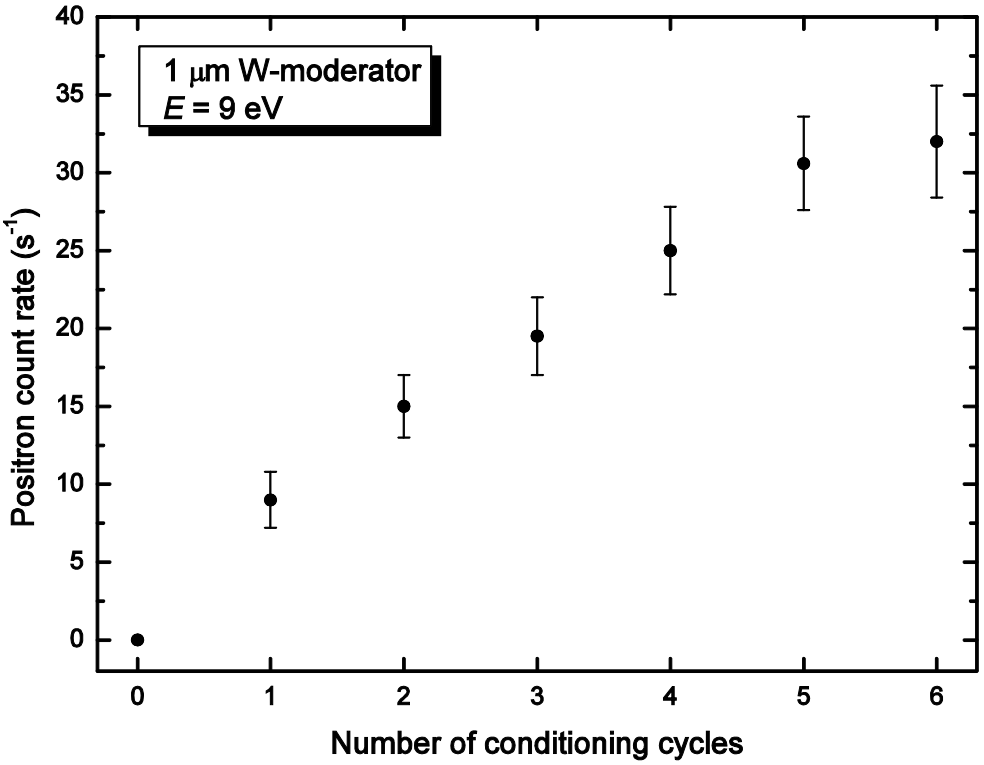

Fig. 2.8. Positron count rate, with a beam energy of 9 eV positrons, as a function of the number of conditioning cycles for a new 1 μm-thick W-moderator. The statistical uncertainties (±1σ) are also given.

Once a film has been recrystallised, in principle it should retain indefinitely this microscopic form and operate with good efficiency (unless mechanical stress is applied). In practice, however, under normal experimental conditions, the moderator emitting surface can degrade with time, e.g. by poisoning, thereby influencing negatively the positron yield. Phenomena such as oxidation or reduction, or more often gas adsorption on the emitting surface, can have an adverse effect on the positron work function of the moderator and, therefore, can significantly reduce ε_m. Note that redox or contaminant adsorption is generally not uniform over the emission surface, so that its effect shows up as a slow but steady decrease in the positron beam intensity. The actual rate of intensity degradation, however, clearly depends on the partial pressure and on the chemistry of the contaminants. Nevertheless, we have found that a further "moderate heating" of the moderator (T ~ 500 °C for W and a little lower for Ni), for a relatively long time (~1 h for W and ~1-2.5 h for Ni), is enough to restore the original moderator efficiency, without having to treat the moderator with a complete conditioning procedure again. By "moderate heating", here, we mean heating the moderator at temperatures well below those needed for recrystallisation, but still above the desorption temperatures of the respective surface contaminants. As carbon and oxygen have been observed as the major surface contaminants on the moderator foil surface, it has been believed that they can be easily desorbed as CO_2 gas through the re-heating process (Lee *et al.*, 1996). In the case of Ni this "moderate heating" corresponds to a power density delivered by the incident electron beam to the moderator (see Section 2.1.1.2) of ~8 W/cm^2.

We will now discuss in more detail the specific conditioning procedure and the achieved results for a W-moderator first, and then a Ni-moderator.

2.1.2.1.1 W-moderator

In situ conditioning of any moderator is achieved in the Trento apparatus by bombarding the moderator with a very high-energy electron beam, generated by a tungsten filament in an electron gun located in the special conditioning chamber (see Section 2.1.1.2). In Table 2.2 we give some typical operational values for one conditioning cycle of a 1 μm-thick W-moderator: the electron beam power density, the bombardment time and the approximate film temperature for six successive steps. The electron beam power density delivered to the moderator surface in both the warming and then cooling phase is also shown in Fig. 2.9, as a function of the elapsed time since the beginning of the conditioning cycle of the W-moderator.

As reported in Table 2.2 and shown by Fig. 2.9, the moderator is gradually heated up to ~2100 °C with a maximum power density of almost 190 W/cm^2. However, the final warming step in the process takes place for only a very short time, thus representing a "flashing" of the moderator. The electron power density delivered to the film is then quite slowly and progressively reduced and, therefore, its temperature gradually decreases with an approximate cooling rate of ~20 °C/min. Note that we have found that increasing the film temperature above ~2100 °C does not further

improve the positron yield, and instead can have the deleterious effect of evaporating the film.

Table 2.2. Typical parameters employed at the University of Trento during the heating stage of one conditioning cycle of a W-moderator.

Step (#)	Power density (W/cm^2)	Approximate T (°C)	Bombardment duration (s)
1	5.2	530	3600
2	26.0	1100	1800
3	42.9	1300	600
4	83.2	1600	100
5	142.9	1850	100
6	187.1	2100	10

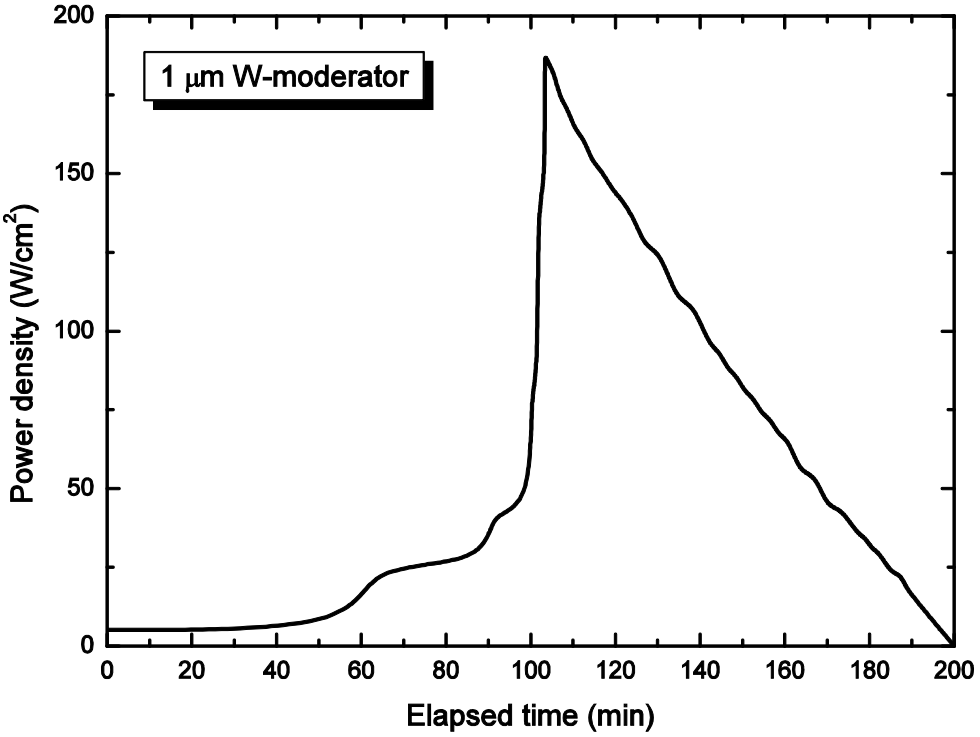

Fig. 2.9. Typical pattern of the electron power density at the moderator surface as a function of the elapsed time, since the beginning of one conditioning cycle of a 1 μm-thick W-moderator.

Very low vacuum pressures in the conditioning chamber are essential for a successful moderator treatment, with an initial background pressure usually in the low-mid 10^{-9} mbar range being needed before starting a conditioning cycle. During the treatment the pressure in the conditioning chamber can rise to the 10^{-6} mbar range, owing to the sample outgassing during the annealing stage. Nevertheless care is taken to ensure that the pressure does not rise further above that threshold, in order to avoid any

potentially dangerous effects on the moderator. This is achieved by allowing some time for the conditioning chamber pressure to stablise after each step. We also allow the pressure in the conditioning chamber to recover to the original background vacuum (~1-5 × 10^{-9} range), before starting a new conditioning cycle.

For a commercial 1 μm W-film, we have found that a maximum positron yield (i.e. the optimum ε_{beam}) is typically obtained after 5-6 complete conditioning cycles (see Fig. 2.8). This ensures that the film has been successfully recrystallised. Once the conditioning process is complete, we usually investigate its performance in terms of the energy and angular distribution of the emitted positrons, before using the moderator for the scattering experiments.

Details about our procedures for an accurate determination of the energy resolution of the positron beam will be thoroughly described in Section 2.1.2.2, therefore here we comment exclusively about the typical results that can be obtained from such a procedure. Notwithstanding that we note here that this method relies on a retarding potential analysis of the positron beam, in other words, measuring the positron count rate as a function of the positron energy (i.e. the apparatus response function). An example of the result of such a measurement is shown in Fig. 2.10, for a positron beam obtained by employing a 1 μm-thick W-moderator in conjunction with the radioactive source. The inflection point of this distribution defines the zero of the energy scale (see Section 2.1.2.2), but that can alternatively determined by establishing the position of the maximum in the derivative of the response function. This is also plotted in Fig. 2.10. In this case we see that a correction of ~-2.25 eV needs to be offset against the moderator to scattering chamber voltage in order to determine the true zero of the energy scale. The response function also contains information about the energy spread of the beam, as the derivative of this function is a rough approximation to the energy distribution of the beam. Therefore, the energy resolution of the positron beam can be estimated as the FWHM of the response function derivative (see again Section 2.1.2.2). In the case of fig. 2.10, we find for an annealed W-moderator an energy width slightly smaller than ~0.3 eV. Occasionally we have observed an energy width of 0.26 ± 0.05 eV. However, the values reported in the literature for the energy spread generally observed with W-moderators span from ~0.6-1 eV (Hugenschmidt *et al.*, 2002; Zecca, 2002). We interpret this discrepancy as being due to a more effective conditioning of the moderator in the Trento spectrometer, and possibly due to some additional energy selection being produced by the hemispherical deflector in our configuration. To support this interpretation, we stress that the measured energy distribution of our moderated positron beam (see Fig. 2.10) is found to be single peaked and quite symmetrical. This is contrary to the observation of Chen *et al.* (1985), whose energy distributions exhibited two peaks (one of higher intensity and narrower width, the other of lower intensity and wider width): we think this behaviour is due to their moderator having two surface fractions with different negative positron work functions. This is quite probably the result of an incomplete conditioning procedure, which leaves “islands” of contamination

on the moderator surface. We can also estimate the angular distribution of the positrons emitted by the moderator and we find that the positron angular spread is of the order of $\Delta\theta \sim 0.15$ rad (FWHM).

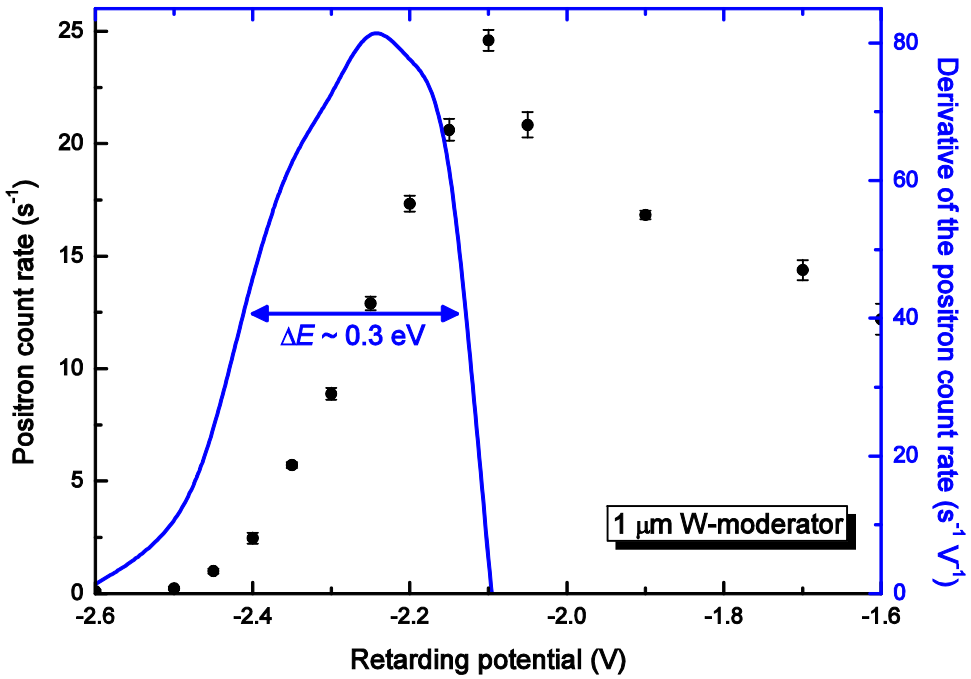

Fig. 2.10. Typical apparatus response function measured with a 1 μm-thick W-moderator in the region of retarding potentials corresponding to the "zero energy peak". The positron count rate and a fit to the derivative of the data points with respect to the retarding potential are shown. The peak of the derivative function denotes the inflection point and thus defines the "energy zero". The full width at half maximum (FWHM) of the derivative determines the energy resolution of the positron beam.

Finally, in the light of all these results, we can estimate an overall positron beam efficiency, ε_{beam}, when using the 1 μm-thick W moderator. In the middle of year 2008, our ^{22}Na source had an activity of $A \approx 2.7$ mCi (see Fig. 2.4), and we used to detect a positron intensity of $I \approx 50$ counts per second at 30 eV energy (see Fig. 2.14). Therefore we obtain:

$$\varepsilon_{beam} = \frac{N_{out}^{det}}{N_{in}} = \frac{N_{out}^{det}}{A \cdot 1\mathrm{Ci}/\Omega} = \approx 1.3 \times 10^{-6}, \qquad (2.11)$$

where 1 Ci = 3.7×10^{10} decays/s is the definition of the unit of radioactivity (1 Bq) and Ω is an angular coefficient accounting for the source-to-moderator geometry.

We note here that the measured efficiency is substantially lower than the moderator efficiency of our tungsten moderators (around 1×10^{-4}; Zecca, 2002). The "pay-off" of this choice is twofold. Firstly, we have an uncommonly flat transmission function (see Section 2.1.2.2). In addition,

this severe reduction of the efficiency is achieved during the positron optical tuning of the beam by selecting the useable positrons from a tiny portion of the beam that emerges from the deflector. This leads as a by-product to a narrow energy distribution in the beam, and to a narrow angular distribution at the scattering chamber. This in turn improves the performance of the spectrometer with regard to the angular resolution error (see Section 2.1.3.4) and to the positron effective length inside the gas cell (see Section 2.1.3.3).

2.1.2.1.2 Ni-moderator

It is well known that Ni-moderators can yield positron beams with an energy spread of 0.1-0.2 eV or better (Fischer *et al.*, 1986; Zecca, 2002). Since this is a factor of ~3 superior over that achievable with our 1 μm-thick W-moderator, Ni-moderators appear to potentially offer real advantages in terms of improving the energy resolution of our positron beam. As a consequence, we have developed a moderator conditioning recipe for a 2 μm-thick Ni film, as detailed below.

Annealing of the Ni film is also carried out by electron bombardment (Section 2.1.1.2), with a conditioning procedure that is qualitatively similar to that pursued with the W-moderator. Despite these similarities, between the conditioning processes of both materials, there are, however, also a few important differences. First of all, the typical parameters characterizing the warming phase of a conditioning cycle are somewhat different in this case (see Tables 2.2 and 2.3). The number of steps, and the film temperature reached at each step, are noticeably reduced during the Ni conditioning process compared to that employed for W. In effect, by following the advice of the late Canter (2004, private communication), the heating of the Ni-moderator is restricted to a much lower maximum temperature (1030 °C), compared to that typically reached by the W moderator (see Table 2.2). Nevertheless, this temperature was high enough to ensure crystallization of the Ni film (Hugenschmidt *et al.*, 2002), but still sufficiently far away from the melting point of Ni (1453 °C) to minimise any possible damage to the film, e.g. through film evaporation. The total warming and cooling times (~100 min each) detailed previously for W are also applicable to Ni, although the cooling rate is necessarily lower in this case (~10 °C/min).

Table 2.3. Typical parameters employed at the University of Trento during the warming stage of a conditioning cycle for a Ni-moderator. H_2 gas at a pressure of $\sim 6\times10^{-7}$ mbar is maintained in the conditioning chamber throughout the process.

Step (#)	Power density (W/cm^2)	Approximate T (°C)	Bombardment duration (s)
1	4.1	450	5400
2	11.5	820	600
3	15.6	930	120
4	18.9	1030	90

Another difference between the Ni- and W-moderators is that conditioning Ni in high vacuum, which is the usual practice with the W moderator, actually seemed to lead to a lower positron efficiency (ε_{beam}). However when the procedure is carried out in a H_2 atmosphere of pressure up to 6×10^{-7} mbar, ε_{beam} improved significantly. Note that H_2 is admitted into the conditioning chamber with a manual valve (Section 2.1.1.2), but by introducing H_2 care must now be exercised to make sure that any possible damage to the film by ion sputtering is avoided.

The energy distribution of the positrons emitted by the Ni-moderator, can be assessed exactly in the same way as that for the W-moderator. In this case, however, the energy zero is situated at a retarding potential voltage of ~-0.25 V (Fig. 2.11). Therefore here a different correction factor needs to be offset against the moderator to scattering chamber voltage in order to calibrate the energy scale. We had anticipated this result, as we had already observed earlier that the negative positron work function of the two materials is different. Another difference compared to the W-case is that the energy width of the positron beam, which is measured here to be $\Delta E \sim 0.1$ eV (FWHM), is clearly superior with the Ni-moderator (Fig. 2.11). This we had expected from the values commonly cited in the literature (see e.g. Fischer *et al.*, 1986; Zecca, 2002). The angular spread of the positron beam in this case is estimated to be a little smaller than $\Delta\theta \sim 0.15$ rad (FWHM), which is marginally superior to when the W-moderator is used.

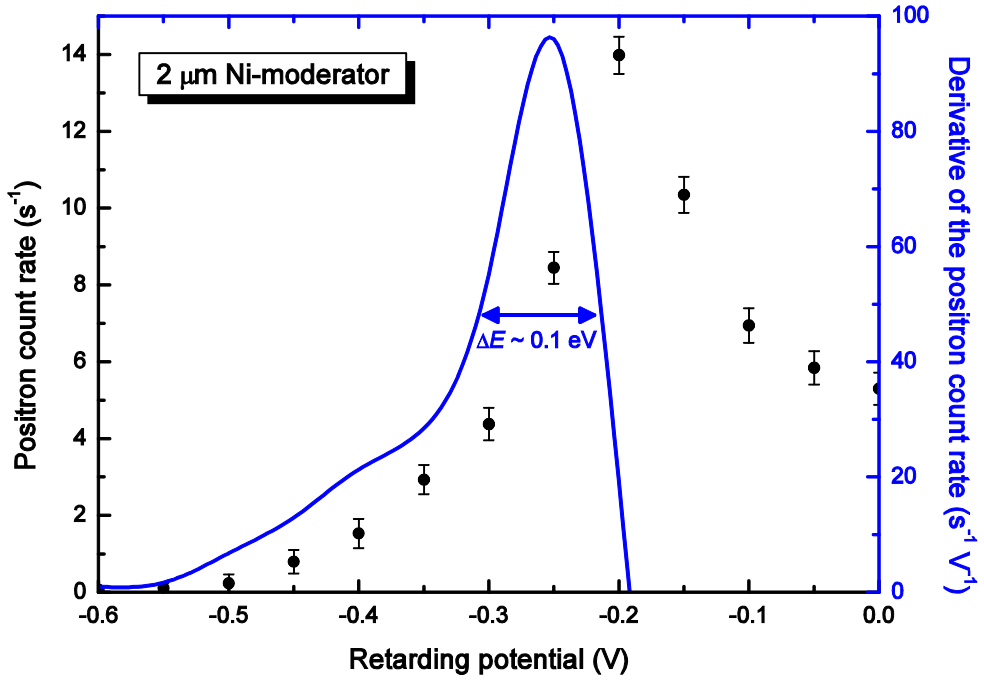

Fig. 2.11. Typical apparatus response function measured with a 2 μm-thick Ni-moderator in the region of retarding potentials corresponding to the "zero energy peak". The positron count rate and a fit to the derivative of the data points with respect to the retarding potential are shown. The peak of the derivative function denotes the inflection point and thus defines the "energy zero". The full width at half maximum (FWHM) of the derivative determines the energy resolution of the positron beam.

In a similar manner to that pursued when discussing the W-moderator, we can also estimate the positron beam efficiency ε_{beam} with the Ni-moderator. We note, however, that in this case the positron count rate detected on average was $I \approx 15$ counts per second, again at a positron energy of ~30 eV. By using Eq. (2.11) with all the other parameters being the same as in the case of the W-moderator, except for I, we obtain an $\varepsilon_{beam} \sim 0.4 \times 10^{-6}$ for the Ni-moderator. This value is a factor of ~4 smaller than the ε_{beam} estimated with the W film, however this is not a surprising result as from Zecca (2002) we find that ε_m for Ni is about a factor of 4 less than ε_m for W.

Like the W-moderator (Fig. 2.8), the Ni-moderator also requires about 5 to 6 complete conditioning cycles before reaching its optimal performance and therefore yield the maximum number of positrons. In this regard we observe that the positron count rates generally detected with the Ni-moderator are somewhat lower than those characterizing the beam produced with the W-moderator (compare Figs. 2.10 and 2.11). This effect possibly reflects a difference in the intrinsic physico-chemical properties of the two materials, which leads to their diverse moderation performances. Nevertheless, we have found that in both cases the count rates were high enough to be able to carry out the attenuation measurements, with sufficiently low statistical noise. We also note that consistent TCS results were obtained when employing either the tungsten or the nickel moderator, when carrying out measurements on the same target.

Regarding the beam stability and operational time of the moderators, we have found that the two materials behave very differently in this respect. While the positron beam intensity resulting from a W-moderator is usually stable for a period of at least 3 months, the performance of the Ni moderator deteriorates much more rapidly over time, so that some "moderate heating" at ~600 °C is needed every two weeks or so with Ni, in order to maintain sufficient (and stable) positron intensity for accurate cross section measurements. However, we have found this issue is not so problematic as to actually interfere with our measurements. In fact a TCS experiment on a given species, with the Trento apparatus, is typically completed over a time frame of 10 to 15 days, so that a moderate heating of the Ni-moderator was performed exclusively each time a new experiment was started. To put this in another perspective, the solid Ne-moderator used on the ATMOP apparatus at the Australian National University (Sullivan *et al.*, 2008b; see Section 2.2.2.1) needs to be grown again roughly every week, due to poisoning of the neon layer from the background buffer gases emerging from the trap. Hence in this sense the Ni-moderator performance represents a potentially competitive option. Finally, we note that a new conditioning of the W- and Ni-moderators, in order to gain full recrystallisation, is only required on about a yearly basis.

2.1.2.2 Energy scale calibration and energy resolution of the beam

We now describe in more detail the procedure pursued for calibrating the energy scale, and determining the positron beam energy resolution, for the

scattering experiments carried out with the spectrometer at the University of Trento (see also Zecca and Brunger, 2007). The determination of the zero point on the energy axis is not a trivial task, particularly when it comes to cross section measurements at very low energies (< 1 eV). Nevertheless, it is crucial to make such a calibration as accurate as possible in order to gather reliable data. In particular, we note here that any error in the energy zero determination affects the apparent energy dependence of the total cross sections.

To help us pursue this subject, we will refer to some diagrams that idealise the real conditions that are usually faced in these experiments. The first of these diagrams is shown in Fig. 2.12, where the configuration of a generic linear transmission technique-based experiment for positron scattering measurements is ideally represented. In that figure:

- S is the source of slow positrons (i.e. the radioactive source in conjunction with a moderator);
- L_1, L_2, L_3 represent the set of charged particle optical lenses (electrostatic elements and magnetic fields) transporting the positron beam;
- M stands for a beam monochromator (if any);
- T stands for the scattering region where the positron beam interacts with the target;
- A is an element analysing the properties of the positron beam, such as its energy distribution;
- DET is the positron detector (in our case the single channel electron multiplier).

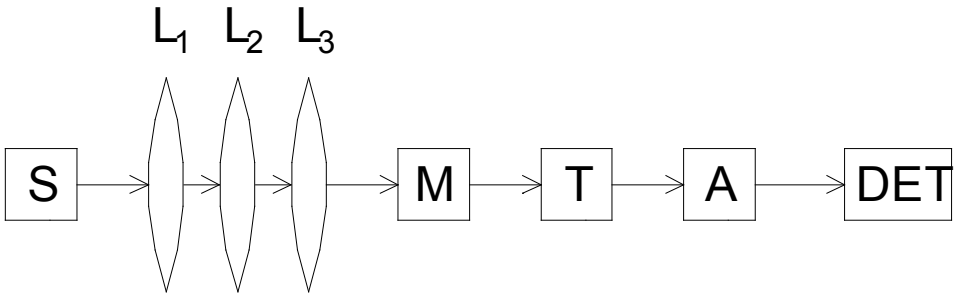

Fig. 2.12. Schematic representation for a generic positron scattering apparatus for total cross section measurements (Zecca and Brunger, 2007).

Every experimental apparatus is characterized by a distinctive response function, which is defined as the positron count rate measured at the detector as a function of the energy. This is normally obtained by performing a retarding potential analysis (RPA) of the beam, in the absence of the target species in the scattering region. Fig. 2.13 depicts the low energy range for an ideal apparatus response function for (a) an ideal monochromatic beam and (b) a "real" beam of finite energy distribution. We see in Fig. 2.13(a) that if the beam were to be monoenergetic, the apparatus response function would be a step function. However, "real"

beams have a finite energy spread and so the shape of the apparatus response function changes to the qualitative representation shown in Fig. 2.13(b). Now, note that in Fig. 2.13(a) the position of the zero of the energy scale is marked by the discontinuity of the ideal step-like apparatus response function. In Fig. 2.13(b), however, this point corresponds to the retarding potential at which the inflection point of the measured apparatus function is seen to occur (Zecca and Brunger, 2007). The full width at half maximum of the derivative of the apparatus response function represents an estimate of the energy resolution of the positron beam (see Section 2.1.2.1). Note that in the past the energy zero has sometimes been supposed to occur at the maximum value of the apparatus response function or, even more often, where the apparatus function approaches zero (Zecca and Brunger, 2007). These assumptions are both incorrect and can lead to an error in the calibration of the energy scale which is at best of the order of the beam energy width.

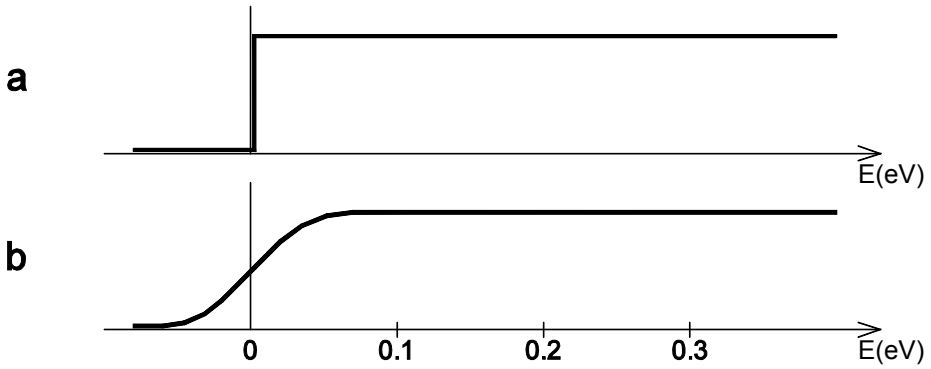

Fig. 2.13. The lowest energy region of an (a) idealised apparatus response function assuming an infinitely small energy width of the positron beam, and (b) the same function but now accounting for the finite energy width of the beam (Zecca and Brunger, 2007).

The general form of a "real" apparatus transmission function is, however, very different from that idealised in Fig. 2.13(b). The typical response function of the Trento apparatus is shown in Fig. 2.14, for almost the full range of energies usually scanned in a scattering experiment. We observe that there are several peaks, which are thought to be the effect of the convolution of the transmission function over the individual optical lenses and deflection devices (Zecca and Brunger, 2007). One of these peaks, namely the maximum that we observe at the very left of the spectrum in Fig. 2.14, was previously thought to determine the zero of the energy scale (see above and Fig. 2.13) and was therefore called the "zero energy peak". As noted earlier, we now know this was incorrect. This maximum is generated by an optical lensing action centred at very low energies, which is possibly due to fringing fields and/or residual magnetic fields in the apparatus (Zecca and Brunger, 2007). Note that such a peak in the count rate at very low energy had originally not been planned by the system designer, and

therefore was not accounted for in the analysis of the positron transport optics in the apparatus (Zecca and Brunger, 2007).

The energy profile shown in Fig. 2.14 and, in general, any apparatus transmission function, is usually obtained with a RPA of the positron beam in the absence of the target gas in the scattering chamber. Note that this is not a limitation in the energy calibration procedure, because the W- and Ni-moderators were found to be rather insensitive to the presence of any target gas in the apparatus (Mills, 1980). In principle, reactive target gases might be able to alter the emitting properties of the moderator, such as its positron work function, thus affecting the effective final energy of the particles at the target. As a consequence, the zero of the energy scale could possibly change during the measuring process. In order to check for this risk, we have carefully examined the sensitivity of the energy zero determination to the presence of gas in the apparatus, by performing RPAs with and without the target gas in the scattering chamber. However, after having investigated more than 40 atomic and molecular targets thus far with the Trento spectrometer, no measurable influence of these gases on the emission properties of either the W- or Ni-moderators has ever been detected.

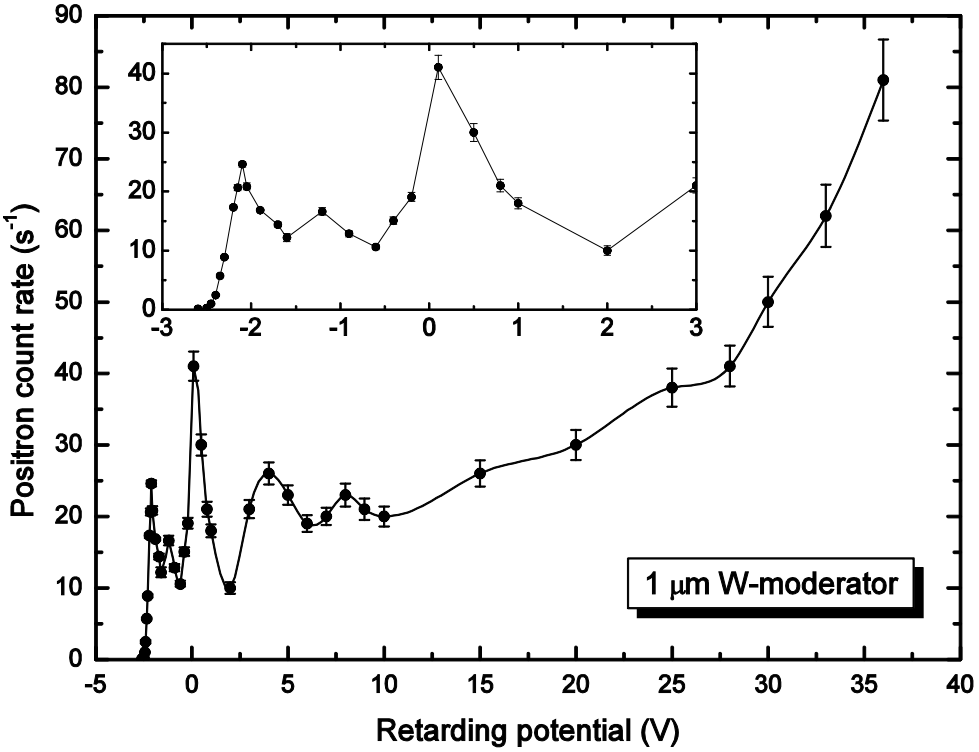

Fig. 2.14. Typical apparatus response function of the Trento spectrometer as measured with a 1 μm thick W-moderator. The inset shows the same curve but now focussing on the lowest energy region. Lines connecting the data points are indicative only.

We note that many other alternative methods for calibrating the energy scale in positron scattering experiments have been reported in the literature.

These include a time of flight procedure (Sinapius *et al.*, 1980), a technique which is known to be rather challenging. Another technique in principle comes from electron scattering experiments, and consists of calibrating the energy scale against a sharp feature in the cross section whose position is well known. However, as no strong resonances in positron total cross sections from any atom or molecule have been measured so far (Surko *et al.*, 2005), the only known relatively sharp feature that could be used as a reference for the energy scale is the onset of positronium formation (Szluinska and Laricchia, 2004). In this case, though, an accuracy in the energy zero no better than ~0.5 eV can be achieved, unless the apparatus is based on a buffer-gas technique. Such a large uncertainty matters particularly at the very low energies (< 1 eV) that are typically investigated with the Trento apparatus. The RPA procedure, instead, represents possibly the most accurate energy calibration technique currently available (Zecca and Brunger, 2007). It also has two notable advantages: it provides a direct calibration of the energy scale and it is relatively straightforward to implement. These are among the reasons why this method is employed not only at the linear transmission-based Trento spectrometer, but also in the more complex buffer-gas trap beamlines, like the one established at the Australian National University in the last few years (Sullivan *et al.*, 2008b; see Section 2.2.2.4).

Nevertheless, the energy scale calibration obtained with a RPA is not without any uncertainty. The error on the energy zero depends exclusively on the accuracy in determining the position of the inflection point in the apparatus response function. To first order this, in turn, is mainly limited by the statistical uncertainty on the positron count rate in the range of retarding potentials where the inflection point is located. By taking into account the effect of the statistical noise and by carrying out a RPA before and after each new experiment on a target species, the energy zero in the experiments performed in Trento was found to be remarkably stable with the time, being reproducible to within ~±0.05 eV (±1σ). We therefore estimate the uncertainty in the position of the energy zero to be less than ~±0.05 eV on time scales on the order of the positron beam time stability, i.e. a few months, when employing the W-moderator. Similar measurements performed on the Ni-moderator show a comparable stability. However, we recall that the energy zero is different for the Ni- versus the W-moderator (as expected from the difference in their respective work functions), so that a new calibration of the energy scale is necessary each time the moderator is changed. When comparing results from calibrations performed within a few years of each other, the energy zero uncertainty turns out to have varied at most ~±0.25 eV. We note that the typical time needed to complete the TCS measurements for an experiment on a given target species, is on the order of only a couple of weeks and that the energy scale employed in each experiment is always referred to the latest calibration that had been performed. This implies that the observed shift in time of the energy zero cannot in any significant sense affect the measurement results. Taking into account both the uncertainty on the energy zero (~±0.05 eV) and that on the energy resolution of the positron beam (~±0.03 eV for the W and ~±0.01 eV

for the Ni-moderator), we estimate an error in the energy scale of our measurements of ~±0.1 eV at most.

The accurate determination of the energy scale calibration is particularly crucial at low energies, where the total cross section is often found to rise rapidly with decreasing energy (Zecca *et al.*, 2006b). We note that in these cases even a small inaccuracy in the energy calibration can produce a significant uncertainty on the true magnitude and trend (energy dependence) of the total cross section. Such an effect, for example, would be very misleading to theoreticians trying to describe the scattering process by attempting to reproduce the experimental data. However, such an error in the energy zero calibration of previous experiments might in principle explain, at least in part, the existing observed low energy total cross section discrepancies (see, for instance, Hoffman *et al.*, 1982 and Kimura *et al.*, 1997 for the case of positron-CO_2 measurements). More details about this point can be found in Zecca *et al.* (2006b). A thorough description of these issues and, in general, of the technique used to calibrate the energy scale of the scattering experiments carried out with the Trento apparatus is given by Zecca and Brunger (2007).

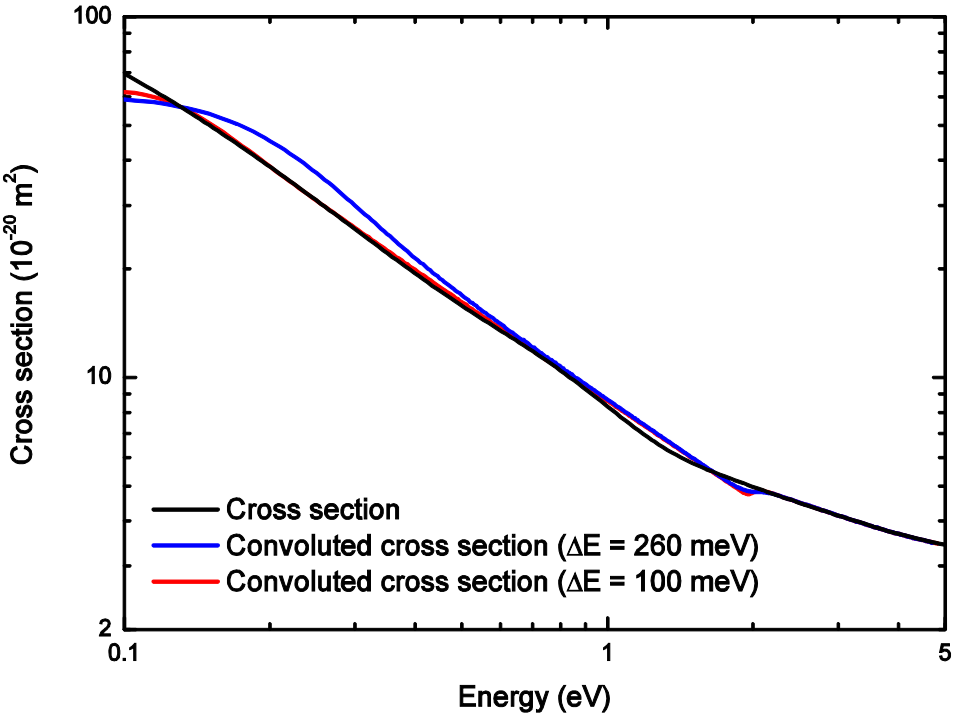

Fig. 2.15. An ideal linear (in log-log scale) cross section and the same cross section convoluted with Gaussian functions of FWHM of 260 meV and 100 meV.

Finally, note that almost all the total cross section results we report in this thesis go down in energy to ~0.1 eV, however, the lowest energy values should be considered with some caution. Owing to the finite energy resolution of the positron beam, which is in the range ~0.1-0.3 eV (FWHM)

depending on the moderator type, the measured cross sections at all energies are actually the convolution of the real (unknown) cross section over the positron energy distribution. At very low energies, typically below ~0.5 eV, where the width of the energy distribution becomes comparable to the incident energy itself, and where the slope of the total cross section as a function of the incident positron energy is also greatest, this effect on the magnitude of the measured cross sections can be significant. This is illustrated specifically in Fig. 2.15, where a linear (in log-log scale) TCS versus energy dependence is convoluted with Gaussian functions of FWHM that respectively correspond to a W- and Ni-moderator. In practice, when corrected for the convolution effect, the lowest energy TCSs should be somewhat higher in magnitude than what are reported in this thesis. Note, however, that the extent of this effect will depend on the actual shape of the total cross section versus energy dependence, and is therefore expected to be species-dependent. The results presented in this thesis are often the first to have ever been measured in the very low energy region, so that in spite of this effect we believe they warrant becoming available to the community.

2.1.2.3 Positron transport

The moderated positrons are transported and focused into the interaction region by means of a set of charged particle optics, with appropriately applied potentials. The electrostatic elements were originally designed on the basis of the tables and graphs in Harting and Read (1976), although practical tips for particle optics design from the lecture notes of Kuyatt (1967) were also used. Details on the construction and the design of the charged particle optics can be found in Zecca *et al.* (1998) and Brusa *et al.* (1997). The first part of the lens elements is made of a tungsten alloy, in order to improve the radiation shielding.

Note that in order to confine the positrons and achieve an additional tunable focussing onto the scattering cell entrance aperture, a weak axial magnetic field used in a lens-like configuration (Zecca *et al.*, 1995) is present in the scattering region. The magnetic field is produced by a solenoid, which is wrapped around the vacuum chamber in correspondence to the scattering cell and the preceding electrode E10 (see Fig. 2.16).The magnetic field applied throughout the present experiments is usually in the range 4-12 G, depending on the positron beam energy.

Fig. 2.16 shows the electrical scheme of the positron spectrometer in Trento. The electric and magnetic fields generated by the electrostatic optical elements E1-E10, the deflector AD and the coil, transport the moderated positrons into the scattering cell. The power supplies A1, A2, A7, A8 and AE set the voltages on the electrostatic elements, whereas I_{sol} controls the flux density of the magnetic field. The positron beam energy that is indicated by the digital multimeter (DMM), is set by the combination of three voltages, A1, AE and the DAC, the latter being a digital-to-analog converter (DAC) controlled by the computer.

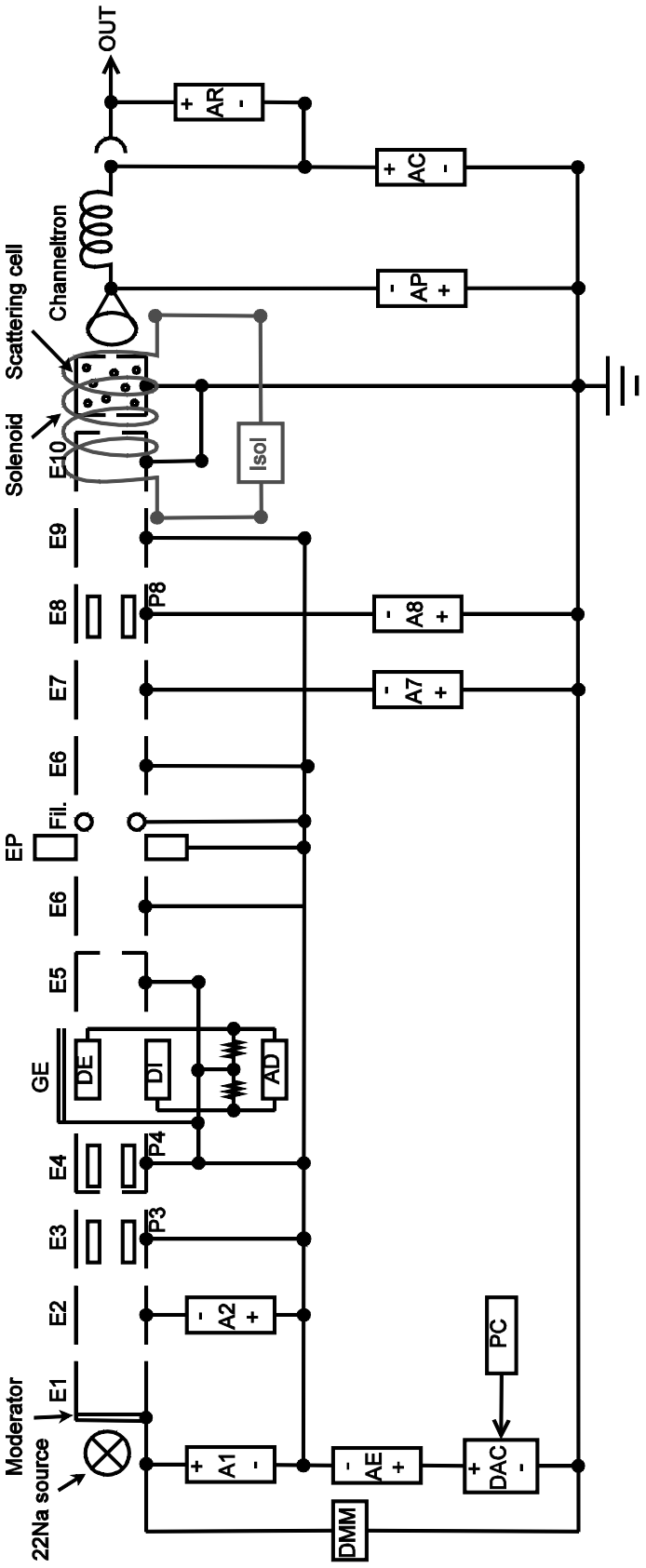

Fig. 2.16. Electrical schematic of the PAIS apparatus, depicting the various elements and their power supplies. Acronyms are defined in the text.

We distinguish two main stages in Fig. 2.16, that are separated by the hemispherical deflector (denoted by AD). The voltages of the electrodes in the first stage do not change with the beam energy. In the second stage, however, some of the potentials and the solenoid current occasionally need to be tuned when measurements at different incident positron energy ranges are performed. A tuning of the voltages of those electrostatic elements is in fact essential, in order to maintain a collimated beam.

Since the first stage of the charged particle optics is typically unchanged, we discuss more in detail what happens in the second stage. The second stage of the spectrometer allows one to select the beam characteristics for the desired scattering experiment, by means of the electrostatic optics and the axial magnetic field. The positrons which exit the hemispherical deflector at the end of the first stage, with an energy of 160 eV, at the output aperture of the deflector, act as the object for all the subsequent electrostatic optics. The aim of this section of the apparatus is to form a stable and well-focused positron beam, with the desired energy and shape characteristics, tunable over a broad energy range. This can be achieved precisely by scanning the positron count rate as a function of the potential applied at the various optical elements, at a given energy, and then setting those potentials that optimise the count rate. Ideally, this should be accomplished by changing the least number of lens potentials, in order to use the same set of voltages for a quite wide range of energies. However, in reality, a fine tuning of the optics is typically needed for the various positron impact energies.

In Figs. 2.17 and 2.18 we provide two examples of such tuning procedures for two of the spectrometer optical elements, namely the solenoid and the hemispherical deflector. Fig. 2.17 thus shows the positron count rate as a function of the solenoid current, using the 1 μm-thick W moderator, and at 18 eV positron energy. Plotted in Fig. 2.17 is also a Gaussian fit to that data. We see that the positron beam is transmitted only in a limited range of currents ~0.1-1.2 A, and that the count rate is maximised if the solenoid current is set to ~0.65 A. This means that, once the other optical elements are set, the value of magnetic field that delivers the largest number of moderated positrons to the scattering cell is B = 0.65 A × 6 G/A = 3.9 G.

Fig. 2.18 now shows the results for the tuning of another optical element, namely the deflector. In this figure the positron count rate is plotted as a function of the deflecting potential, for the 1 μm-thick W moderator at 9 eV positron energy and also the 2 μm-thick Ni moderator at 50 eV energy. Again we see a Gaussian-like distribution in both cases, with a peak in the count rates located at 63.7 V and 62.75 V, respectively. This difference in the position of the two peaks contains some information about the difference in the work function of the two materials. The main result of Fig. 2.18 is that the positron beam is transmitted only in a very narrow potential range of less than 1.5 V width.

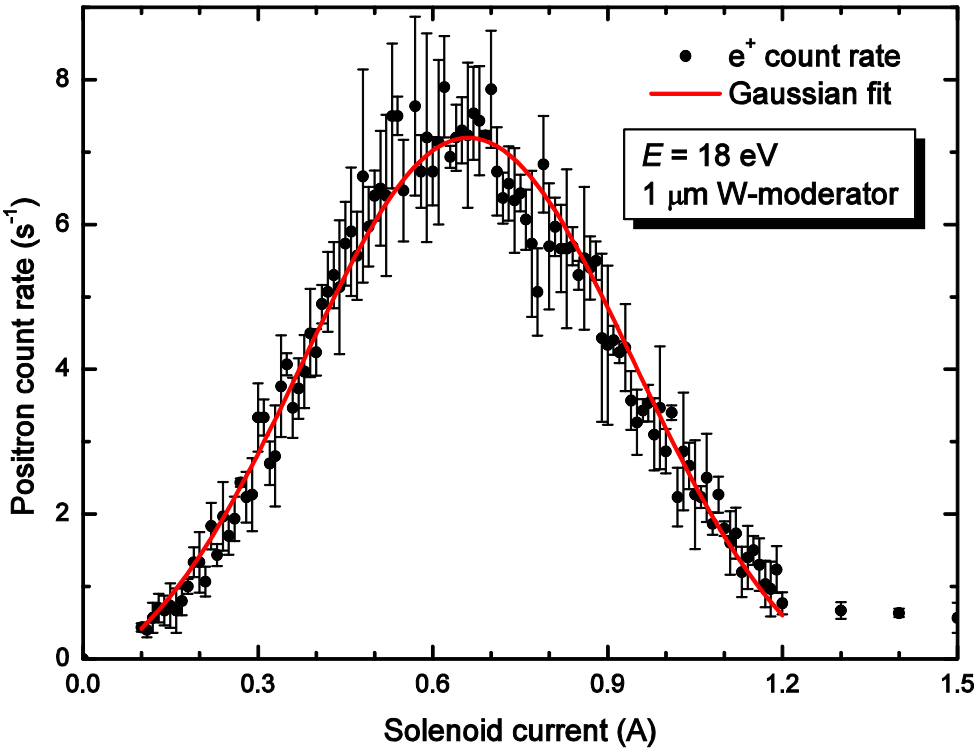

Fig. 2.17. Positron count rate against solenoid current, with a 1 μm-thick W-moderator at 18 eV positron energy. Shown also is a Gaussian fit to the data.

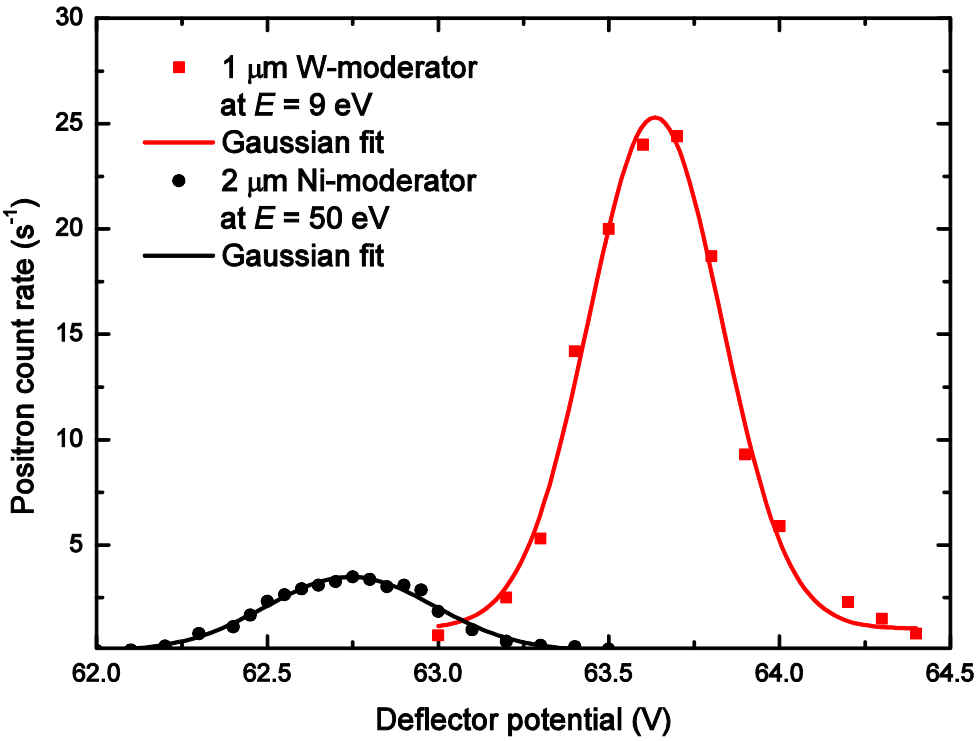

Fig. 2.18. Positron count rate with respect to the deflector voltage for a 2 μm-thick Ni-moderator at 50 eV positron energy and a 1 μm-thick W-moderator at 9 eV energy. Shown also are Gaussian fits to the data.

The original design criteria for positron transport in the Trento spectrometer have been checked and verified using the ray-tracing facility of SIMION (Manura and Dahl, 2008), a commercial charged-particle optics software package. However, as SIMION does not allow one to create joint electrostatic and magnetic arrays, we have driven our simulation including only the electrostatic elements (E1-E10) present in the apparatus and neglecting the effect of the magnetic field generated by the coil in the region corresponding to the electrode E10 and the scattering cell (see Fig. 2.16).

In Fig. 2.19 we therefore present our ray-tracing results at (a) 0.1 eV, (b) 1 eV and (c) 10 eV positron energy at the scattering cell entrance aperture. In each frame seven positrons are assumed to leave from the exit plane of the hemispherical deflector (E5), with an energy of 160 eV, and are transported into the scattering cell (SC) by the electric fields generated by the subsequent electrodes. In each case the positrons start with elevation angles of 0°, ±0.5°, ±1° and ±1.5° with respect to the axis of cylindrical symmetry. These angles correspond to the maximum angular divergence of the positron beam at E5, as obtained from the results of simulations for the positron optics transport in the first stage of the spectrometer (not shown). The potentials applied to the various electrodes in this second stage of the spectrometer (E5-E10), in order to obtain the ray-tracings shown in Fig. 2.19, are reported in Table 2.4. These voltages are largely equivalent to those employed in the actual experiments.

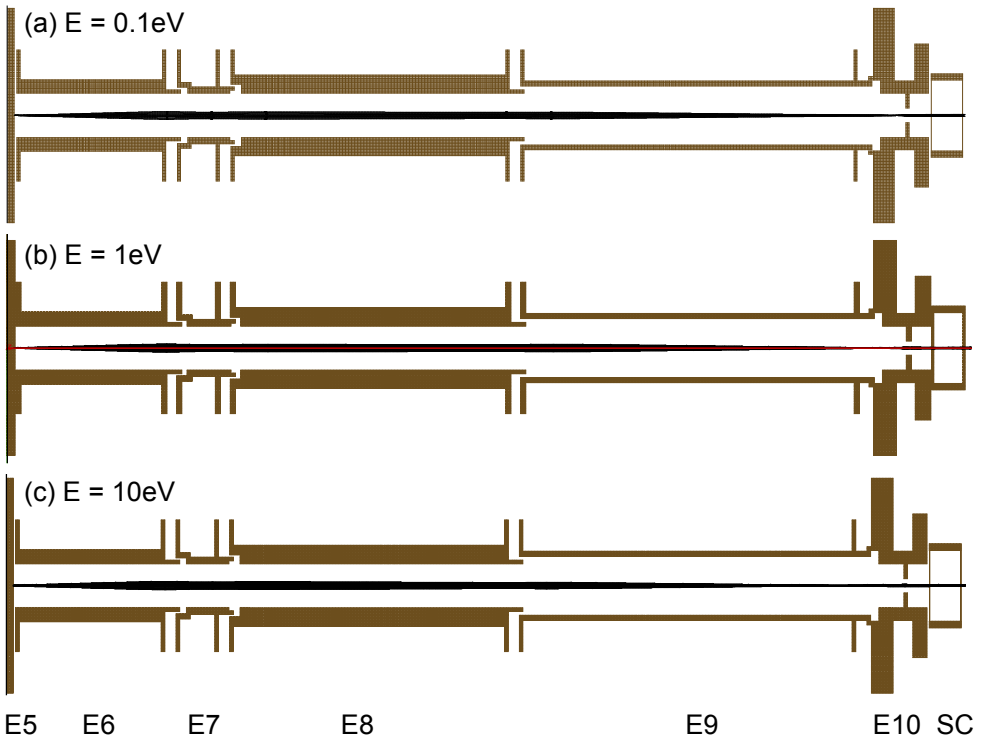

Fig. 2.19. Schematic diagram showing SIMION ray-tracing outputs for positron energies at the scattering cell of (a) 0.1 eV, (b) 1 eV and (c) 10 eV. 3D cylindrical symmetry is to be assumed. See text for further details. Scale: 2 grid units = 1 mm in each case.

Table 2.4. The set of potentials applied at the electrodes E5-E10, in order to obtain the ray-tracing results shown in Fig. 2.19, for each of the three selected scattering energies. Also given is the estimate of the width (*D*) of the positron beam at the scattering cell entrance aperture.

Electrode	**Potential w.r.t. moderator (V)**		
	E = 0.1 eV	**E = 1 eV**	**E = 10 eV**
E5, E6	-160	-160	-160
E7	-594	-600	-620
E8	-349	-401	-370
E9	-160.1	-160.1	-160.1
E10, SC	-0.1	-1	-10
D (mm)	1.2	0.6	1.3

The results of the ray-tracing simulations (Fig. 2.19) indicate that a well collimated and focussed positron beam, with good angular divergence characteristics, is formed at the entrance aperture of the scattering cell over the range of positron energies of typical interest in our studies (~0.1-50 eV). At each energy shown in Fig. 2.19, in fact, the positron beam width at the scattering cell entrance aperture is found to be always less than the corresponding (entrance and exit) aperture diameter (1.5 mm). Note that if the present simulations were to account also for the confining magnetic field present in the scattering region, the characteristics of the positron beams represented in Figs. 2.19(a-c) would only improve.

These results also prove that this experimental configuration can reach a very high transmission efficiency of the positron beam under proper conditions (Zecca *et al.*, 1995). Moreover, as it is clearly feasible to obtain a well-focussed beam with a diameter smaller than the scattering cell apertures, we can confirm that the choice of reducing the size of the scattering cell apertures in the present apparatus compared to those usually employed in other beamlines (see, for instance, Sullivan *et al.*, 2008b) turned out to be judicious. A scattering cell with very small apertures, in fact, assists one to minimise, for example, the angular discrimination error and the error related to so-called end effects (see Section 2.1.3.4 and 2.1.2.5, respectively).

We finally note that, despite the fact that most of the measurements with the Trento spectrometer were undertaken at energies below ~50 eV, where we suspect most of the interesting positron-related physical processes take place, the positron transport optics were originally designed to produce a stable and well-focused positron beam with energies spanning from ~0.1 to 150 eV. From the results shown in Fig. 2.19 and the operational performance of the Trento spectrometer, over many years now, we can conclude that those original design criteria appear to have successfully been met.

2.1.2.4 Preparation of the target sample

Throughout the various cross section measurements described in the present thesis, only high-purity target samples were used. Our aim is to make scattering experiments on a specific molecule, so that only very pure substances are eligible.

All the samples that are a liquid at room temperature were subjected to several freeze-pump-thaw cycles, before being employed in the experiments, to ensure they were appropriately degassed and to remove any possible impurities that may affect the results of our measurements. All the liquid targets examined in our studies were found to be sufficiently volatile at room temperature to allow us to achieve the required beam attenuation.

When the target of interest was a gas, the tubes connecting the sample to the scattering chamber were flushed with the target gas at a pressure, as measured in the scattering cell, 10^4 times larger than the background vacuum pressure, before starting the experiment. This operation helps cleanse the pipes from any potential residual molecules that we investigated in a preceding experiment.

In addition, our sample holder was thermally insulated during each experiment, in order to "damp down" the effect caused by any short-term fluctuations in the room temperature. We note that such fluctuations, however, were typically small (±2 °C).

2.1.2.5 Experimental precautions and measurement practices

Before describing in detail our standard procedure for total cross section measurements, at the University of Trento, we note that several important precautions need to be taken and great care must be exercised during the measurements. Some of these considerations are now described.

"End effects" might influence the measured cross section. Owing to the target gas emerging from the scattering cell through the entrance and exit apertures, the positron path in the region of interaction tends to be actually somewhat longer than the geometric length of the scattering cell. Conversely, as a consequence of the gas pressure being a little lower immediately inside the cell near the entrance and exit apertures, the geometrical length of the scattering cell is effectively decreased. These two effects are basically the result of having apertures of finite diameter at the entrance and exit of the scattering cell. However it is known that these effects can be minimised by having entrance and exit apertures in the scattering cell of the same size, and they become negligible if these apertures also have a relatively small diameter (Dalba *et al.*, 1979; Blaauw *et al.*, 1977), as in the present experimental configuration. The "end effect" contribution to the uncertainty in the positrons path length is estimated to be possibly less than 0.2%.

A further experimental consideration that needs to be taken into account, when making attenuation measurements, is to ensure that the measured total cross sections are independent of the target vapour pressures in the scattering cell. To achieve this, it is a standard practice to check for the linearity of the plots of $\ln(I_1/I_0)$ against gas pressure at selected energies

(Kennerly and Bonham, 1978), where I_1 and I_0 represent the positron count rate in the presence and in the absence of the target gas in the interaction region, respectively. This is equivalent to saying that we need to minimise double scattering events, and we certainly try to keep their number below the few percent limit. We have found experimentally that double scattering can be minimised by operating at target pressures, in the scattering cell, such that the beam attenuation factor $A = I_1/I_0$ remains typically in the range 0.6-0.8.

To start a set of measurements, the details about each run, and some of the experimental parameters, need to be input into the software that manages the measurements cycle. These include the desired positron energy of each measurement and the solenoid current at that energy. The file of the experimental parameters specifically contains the desired beam attenuation A, the gate times for the measurement of the positron count rates and pressures, the number of pressure and positron count rate sampling cycles, the opening times for the Baratron valve (VL), a failsafe upper limit for the gas pressure (P_L) and some delay times to allow for system stabilisation in between the various operations.

The aim is to measure the values of the following quantities, at each investigated incident positron energy E, which are relevant for the calculation of the cross section:

- the positron count rate in the absence (I_0) and in the presence (I_1) of the target gas in the scattering region;
- the pressure in the scattering cell in the presence (P_1) and in the absence (P_0) of the target gas in the scattering region;
- the temperature (T) of the target gas in the scattering cell.

In addition, the background pressures in the vacuum system, before starting the measurement (P_a) and after it is completed (P_b), are also measured. This is done to make sure that no drift in the background vacuum pressure occurs in the interim. If a drift in the vacuum pressure has occurred, then the other pressure readings can be corrected for this effect.

The operations driven by the apparatus manager program, during a standard measurement cycle, are schematically summarised in the flow chart shown in Fig. 2.20. Note that there are five stages in each measurement cycle:

1. Initialisation of the measurement.
   1.1. The input file containing the list of measurements to be carried out is read. For each measurement the incident positron energy E and the solenoid current I_{sol} must be specified.
   1.2. The beam energy E and the solenoid current I_{sol} are set.
   1.3. The background pressure of the vacuum (P_a) is measured before starting the measurement.
2. Calibration of the target pressure in the scattering cell, in order to achieve the required attenuation of the beam intensity.
   2.1. The count rate I_a in the absence of the target gas in the scattering region is measured.
   2.2. The Baratron valve (VL) progressively opens, first for a long time (~7-10 s), in order to inject the target gas into the scattering cell.

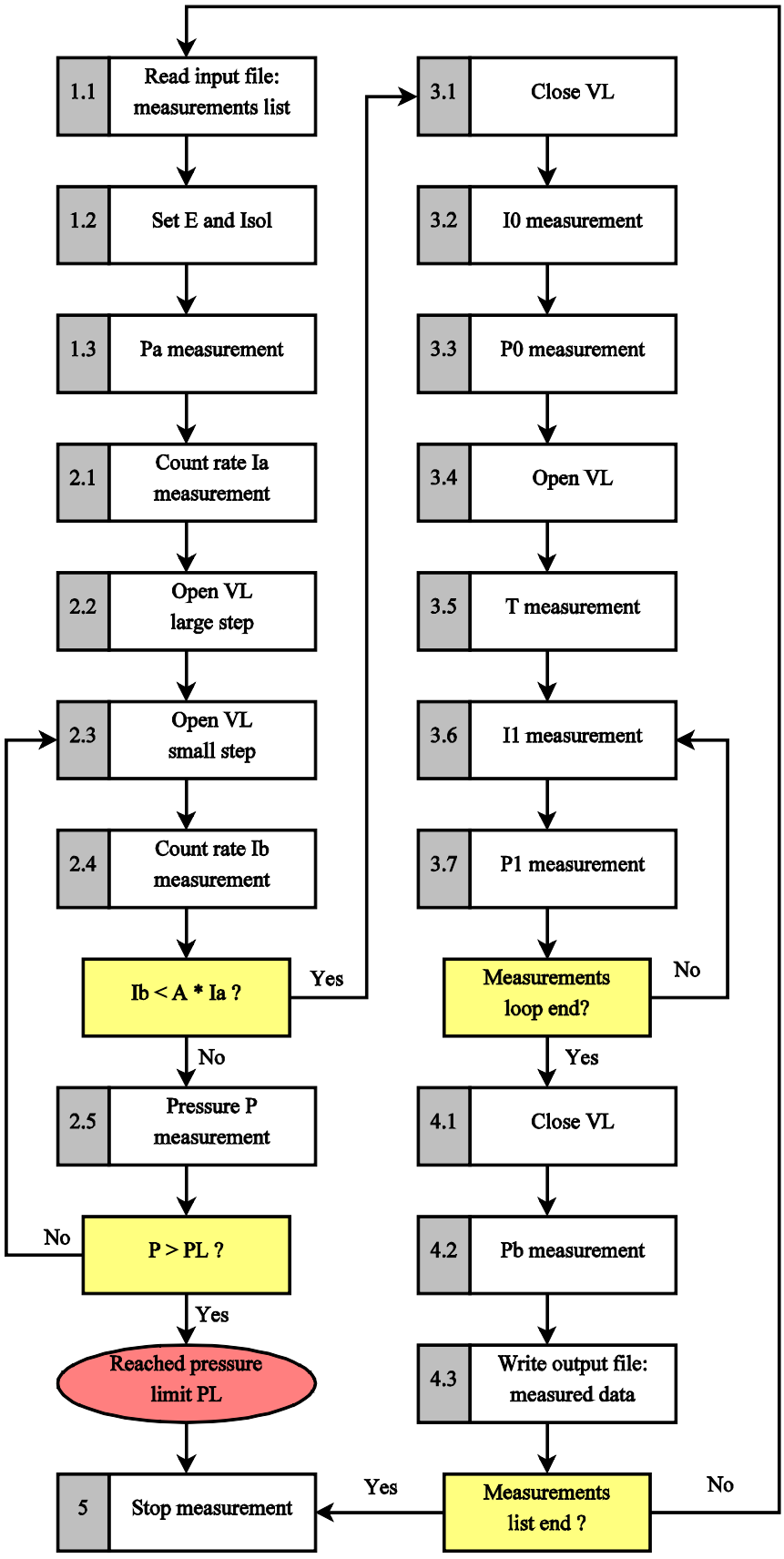

Fig. 2.20. Schematic flow chart of the software-driven events during a standard measurement cycle.

2.3. The Baratron valve (VL) might open again for a short time (~0.2-0.5 s), in order to inject further gas into the scattering cell.
2.4. The count rate I_b, now in the presence of the target gas, is measured. If $I_b < A \times I_a$, i.e. the beam intensity attenuation has achieved at least the desired minimum value A, then the measurement can start (3.1).
2.5. Otherwise, the pressure is read in order to check whether the amount of gas in the scattering cell is too great after the first opening of the valve. If this is the case, then the measurement is stopped (5), for safety, because the pressure is too high. If the pressure, however, is still below the limit, then it means that the amount of gas in the cell is not yet high enough to achieve the required minimum beam attenuation. In this case the valve opens for another short time (2.3).

3. Execution of the measurement.
3.1. The Baratron valve is closed so that the measurement in the absence of the target gas, in the scattering cell, can be started.
3.2. The positron count rate I_0 in the absence of the gas is measured.
3.3. The pressure of the vacuum P_0 in the scattering cell is measured.
3.4. To start the measurement with the target gas in the scattering cell, the valve gradually opens for the time determined by the calibration procedure (2), so that the desired beam attenuation is met.
3.5. The temperature of the target gas is measured.
3.6. The positron count rate I_1 with the gas in the cell is measured for a pre-determined number of times.
3.7. The pressure of the target gas P_1 in the scattering cell is measured for a pre-determined number of times.

4. Conclusion of the measurement.
4.1. The Baratron valve is closed to pump out the scattering chamber.
4.2. The background pressure of the vacuum (P_b) is once again measured after the measurement has finished, in order to check whether any drift has occurred.
4.3. The output file containing the relevant measured data is written. If this measurement is the last in the input file list (1.1.), the experiment is terminated, otherwise the next measurement in the list is started (1.2).

5. The experiment is over.

The measurement time is typically about 30 min for each discrete energy point, with each point being the average of several individual determinations. All the measurements were carried out with a stable positron beam, with the count rates at a given energy typically varying just within a few percent over times on the order of months.

2.1.3 Data analysis and corrections

Once the relevant information has been gathered from an experiment, as described in Section 2.1.2.5, the raw data needs first to be analysed and in some cases also corrected to account for instrumental effects that inevitably

affect the measurements. These factors are now discussed in more detail below.

2.1.3.1 Calculation of the total cross section

The basis of all linear transmission experiments is the Beer-Lambert law, which is defined by:

$$I_1 = I_0 e^{-\frac{(P_1 - P_0)L\sigma}{k_B T}}, \tag{2.12}$$

where σ is the total cross section of interest at a given incident positron energy E, I_1 is the positron beam count rate at P_1, the pressure measured in the scattering cell when the relevant target gas is routed to the scattering cell, and I_0 is the positron beam count rate at P_0, the pressure in the scattering cell when the relevant target gas is diverted into the main vacuum chamber, i.e. away from the scattering cell. We recall that in this latter configuration, the attenuation in the scattering chamber is negligible (10^{-3} of the attenuation with P_1). Finally, k_B is Boltzmann's constant, T is the temperature of the target gas in the scattering region (in K), and L is the length of the scattering cell (22.1 ± 0.1 mm). Therefore, from Eq. (2.12) the total cross section is:

$$\sigma = -\frac{k_B T \ln(I_1/I_0)}{L(P_1 - P_0)}, \tag{2.13}$$

and thus can in principle be determined after all the relevant quantities have been measured in an experiment (see Section 2.1.2.5).

2.1.3.2 Thermal transpiration

We recall that the pressure of the target gas (or vapour) within the scattering cell is measured with one of the two MKS Baratron capacitance manometer models available in the laboratory. Those manometers operate at either 45 °C (model 627B) or 100 °C (Model 628B), and are connected to the scattering cell via a tube of 10 mm diameter. As the vacuum chamber is always at room temperature (24 ± 2 °C) during the experiments, so are the target gas molecules in the scattering region. Hence the gas molecules tend to drift from the cold to the warm end of the linking pipe, an effect known as thermal transpiration. In fact if two vessels at different temperature T_a and T_b are connected by a narrow tube, and if the pressure of the gas in the system is so low that the mean free path of the gaseous molecules is several times larger than the diameter of the linking pipe, then the ratio of the pressures in the respective vessels is proportional to the square root of the ratio of their temperatures (Knudsen, 1910):

$$P_b/P_a \propto \sqrt{T_b/T_a}. \tag{2.14}$$

Consequently the pressure measured by the relevant manometer needs to be corrected for this thermal transpiration effect, in order to reflect the actual pressure of the target gas within the scattering cell, before it can be used in Eq. (2.13). This correction is calculated by employing the empirical model developed by Takaishi and Sensui (1963), which is basically a modification of the original formula found by Liang (1951; 1952; 1953; 1955). According to the empirical equation given by Takaishi and Sensui (1963), the thermal transpiration correction factor for the pressure measured by the manometer (P_b) compared to the actual pressure of the target gas in the scattering cell (P_a), both in units of Torr or mmHg, is given by:

$$\frac{P_b}{P_a} = \frac{Ax^2+Bx+C\sqrt{x}+\sqrt{T_{man}/T_{SC}}}{Ax^2+Bx+C\sqrt{x}+1}, \tag{2.15}$$

where T_{man} is the operating temperature of the manometer (K) and T_{SC} the temperature of the target gas in the scattering cell (K). The parameter x is equivalent to:

$$x = P_b d, \tag{2.16}$$

with d being the diameter of the tube connecting the manometer to the scattering cell (in our case d = 10 mm). The coefficients A, B and C are functions of the average temperature $\bar{T}$ between that of the manometer and that of the scattering cell:

$$\bar{T} = \frac{T_{man}+T_{SC}}{2}, \tag{2.17}$$

and they also depend on the hard-sphere molecular diameter D (Å) of the target species. Specifically:

$$A = A^*\bar{T}^{-2} \quad \text{with} \quad A^* = 1.4 \times 10^4 e^{0.507D}, \tag{2.18}$$

$$B = B^*\bar{T}^{-1} \quad \text{with} \quad B^* = 5.6e^{0.607D}, \tag{2.19}$$

$$C = C^*\bar{T}^{-1/2} \quad \text{with} \quad C^* = \left(\frac{110}{D}\right) - 14. \tag{2.20}$$

Note that the correction to the pressure readings is to be calculated for the difference of the pressure with and without the target gas in the chamber, i.e. P_1-P_0, and not separately for the two pressures.

Two examples for the results of a typical thermal transpiration correction are shown in Fig. 2.21. In that figure the correction factor to the pressure, as a function of the measured pressure, is given for the data of two experiments undertaken as part of this thesis. The first of those experiments was on molecular nitrogen (N_2) and the second on carbon monoxide (CO) (see Chapter 4). In the experiment on N_2 the manometer model 628B, operating at T_{man} = 100 °C was used, whereas for CO the other manometer which

operated at T_{man} = 45 °C was employed. In both cases, the respective target gas in the scattering cell was assumed to be at the same room temperature (T_{SC} = 24 °C). To calculate the thermal transpiration corrections, hard-sphere diameters of 3.75 Å (Khakoo *et al.*, 2008) and 3.6 Å (Skowronek and Alayli, 1979) were used for the N_2 and CO molecules, respectively.

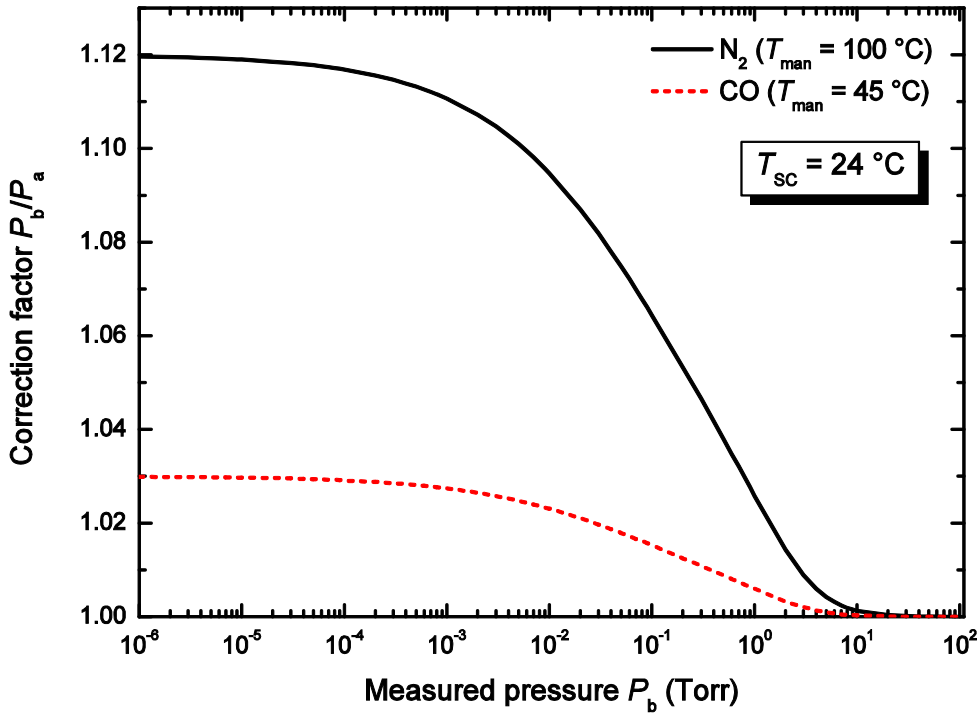

Fig. 2.21. Typical thermal transpiration correction curves. The correction factor P_b/P_a is shown as a function of the measured pressure P_b, where P_a is the corrected pressure, for the measurements on N_2 and CO (see Chapter 4). Those measurements were carried out with two different manometers operating at 100 °C and 45 °C, respectively. In both cases the target gas in the scattering cell was assumed to be at the same room temperature (24 °C). The molecular diameters used to calculate the corrections are 3.75 Å for N_2 (Khakoo *et al.*, 2008) and 3.6 Å for CO (Skowronek and Alayli, 1979).

In Fig. 2.21 we see that, for the range of pressures commonly measured in the scattering cell when the target gas is present (~10^{-3}-10^{-4} mbar), the thermal transpiration correction to the pressure readings can be as high as ~12%, when the manometer operating at 100 °C is in use. Whereas, when the other manometer operated at 45 °C is employed, the same correction turns out to be smaller (~3%), as we would expect.

Note that as the effect of the thermal transpiration correction is to effectively reduce the pressure compared to the value measured by the manometer, this causes the total cross section to increase somewhat in magnitude with respect to the "raw" measured value.

2.1.3.3 Positron path length increase

Another effect that the raw data has to be corrected for, is the positron path length increase within the scattering cell caused by their gyration due to the focusing axial magnetic field present in the interaction region. In practice, this means that the exact value of L to be used in Eq. (2.13) is slightly larger than the geometrical length of the scattering cell. This effect arises because, although the positron beam in the apparatus is well-collimated, not all the positrons in the beam move exactly in the direction of the applied magnetic field lines.

In general a particle with electric charge q moving with velocity $\vec{v}$ in a magnetic field $\vec{B}$, will experience a Lorentz force $\vec{F}$ given by:

$$\vec{F} = q\left(\vec{v} \times \vec{B}\right). \tag{2.21}$$

If the particle velocity is exactly parallel to the magnetic field, then the vector product is zero. However, if the velocity component perpendicular to the direction of the magnetic field is finite (i.e. $v_\perp \neq 0$), then the Lorentz force will be non-zero and thus the particle will move in a spiral motion. The radius r of this circular motion is defined as the gyro-radius and is given by:

$$r = \frac{mv_\perp}{|q|B}, \tag{2.22}$$

where m is the mass of the particle. Note that the time t_0 of one full gyration is:

$$t_0 = \frac{2\pi m}{qB}. \tag{2.23}$$

If we define a pitch p as the path length of one gyration in the direction parallel to the magnetic field, i.e.:

$$p = v_\parallel t_0, \tag{2.24}$$

where $v_\parallel$ is the parallel component of the velocity, then the length L_0 of one turn in the spiral is:

$$L_0 = \sqrt{(2\pi r)^2 + p^2}. \tag{2.25}$$

The number (n) of gyrations completed when covering the path length L parallel to the magnetic field is given by:

$$n = \frac{L}{v_\parallel t_0}. \tag{2.26}$$

For the typical experimental conditions of our measurements, with a magnetic field of B = 10 G, an analytical calculation based on Eqs. (2.21-2.26) yields a correction (increase) of 5% in the path length when the angle of the incoming positron is 0.05 rad. The angular divergence in our charged particle optics is most probably smaller than 0.05 rad, and therefore a 5% increase in the positron path can be assumed as the upper value.

In order to assess this correction (increase) in L, we have also carried out some ray-tracing simulations with the software SIMION (Manura and Dahl, 2008). For this purpose we have created a magnetic potential array, with a dimension equivalent to the geometrical scattering cell length, and have assumed magnetic fields in the typical range employed in our experiments (~4-12 G). Fig. 2.22 shows the outputs of these simulations, for a magnetic field flux of 10 G and for three selected positron beam energies: (a) 0.1 eV, (b) 1 eV and (c) 10 eV. In each case the positrons are assumed to enter the magnetic field region with divergence angles of θ = 0 rad, ±0.05 rad and ±0.1 rad, with respect to the magnetic field vector.

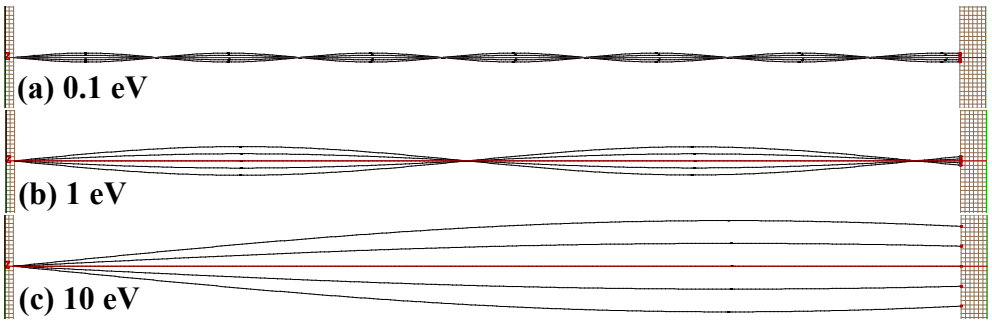

Fig. 2.22. Schematic diagrams showing SIMION ray tracing simulations of the gyration of the positrons in the focussing axial magnetic field in the scattering region. Magnetic field strength B = 10 G. Scattering cell length L = 22.1 mm. Positrons enter the scattering cell with divergence angles of θ = 0, ±0.05, ±0.1 rad. Scale: 1 grid unit = 0.1 mm. Results are shown for three selected incident positron energies: (a) 0.1 eV, (b) 1 eV and (c) 10 eV.

The results from these simulations suggest that, irrespective of the incoming positron energy in the range 0.1-50 eV and of the magnetic field spanning 4-12 G, the effective positron path length increase varies from zero, of course when θ = 0 rad, to +0.13% for θ = 0.05 rad and reaches +0.5% at θ = 0.1 rad. The fact that the positrons path length does not depend on the magnetic field is essentially due to a compensating effect between the gyro-radius and the number of gyrations. This follows as when the magnetic field is low, the gyro-radius is large (Eq. 2.22) and the number of gyrations is high (Eq. 2.26), whereas when the magnetic field is high, the gyro-radius is small (Eq. 2.22) but the number of gyrations is low, so that the positrons path length is effectively the same in both cases.

As a consequence, mainly of the analytical calculation, but having in mind the ray-tracing results, the effective length correction we usually apply

to the positron path length L is ~+5%, with a magnetic field of 10 G, at all positron energies.

2.1.3.4 Forward angle scattering effects

All linear transmission scattering-cell based experiments invariably suffer from some angular discrimination limitations, due to their inability to distinguish between positrons that are elastically scattered at small angles from those of the primary unscattered beam. This effect results in the directly measured TCSs being somewhat smaller than the "true" value. The extent of this effect essentially depends on two factors: the specific geometry of the scattering and detection regions in the experimental setup and the nature of the elastic differential scattering cross section in that forward angular range, which is target-species dependent (Sullivan *et al.*, 2011).

From a consideration of the size of the entrance and exit apertures of our scattering cell, and their separation, and the presence of a further skimmer before the CEM detector, the angular acceptance of the positron detector employed in the Trento apparatus is estimated to be no worse than $\Delta\theta \approx 4°$, corresponding to a solid angle of $\Delta\Omega \approx 4 \times 10^{-3}$ sr. This value compares favourably with those of the spectrometers at Yamaguchi University ($\Delta\theta \approx 7°$) (Makochekanwa, 2010, private communication) and Wayne State University ($\Delta\theta \approx 16°$) (Kauppila *et al.*, 1981). The gyration of the positrons, due to the axial magnetic field present in the interaction region, can potentially influence the angular discrimination (and, therefore, also the associated correction) compared to that of the no-field case (Hamada and Sueoka, 1994). In effect when a positron is scattered at some angle, as a consequence of the collision with a target atom or molecule, the scattered particle starts spiralling because of the presence of the axial magnetic field (see Section 2.1.3.3). This circular motion then increases the probability that the particle passes through the exit aperture and is ultimately detected. We have used some of the analytic formulae detailed in Kauppila *et al.* (1981) to estimate the energy-dependent angular discrimination θ_s of the Trento apparatus (see Table 2.5). Specifically, the most crucial equation is:

$$\theta_s = \sin^{-1}\left(\frac{qrB}{\sqrt{2mE}}\right), \tag{2.27}$$

where q is the particle charge, r is the orbit radius (Eq. 2.22) at the exit aperture, B the magnetic field, m the particle mass and E the particle energy. By applying Eq. (2.27) to the typical experimental conditions of our measurements, we find that the angular discrimination varies from ~71.6° at 0.1 eV positron energy to ~2.4° at 50 eV (Table 2.5). The present estimates for the angular discrimination of the spectrometer at the University of Trento compare very well to those of the positron beam at the Australian National University (see Table 2.9), in spite of the two spectrometer having very different configurations. The estimates cited in the literature for the angular discrimination of the earlier positron scattering measurements vary considerably, but typical values range from 6.5° (Charlton *et al.*, 1984) up to

13°-20° (Stein *et al.*, 1978; Kwan *et al.*, 1984) and can even be as large as 40° (Canter *et al.*, 1973).

Table 2.5. The angular discrimination (θ_s) of the spectrometer at the University of Trento, at selected positron energies, as calculated using Eq. (2.27) for the typical conditions of the present experiments.

Energy (eV)	θ_s (°)	Energy (eV)	θ_s (°)	Energy (eV)	θ_s (°)
0.1	71.6	1	17.5	10	5.4
0.2	42.1	2	12.2	20	3.8
0.3	33.2	3	10.0	30	3.1
0.4	28.3	4	8.6	40	2.7
0.5	25.1	5	7.7	50	2.4
0.6	22.8	6	7.0		
0.7	21.0	7	6.5		
0.8	19.6	8	6.1		
0.9	18.4	9	5.7		

An alternative approach to using the formulae from Kauppila *et al.* (1981) and the method of Hamada and Sueoka (1994), in order to estimate the forward angle scattering effect, would be to conduct a Monte Carlo simulation of the behaviour of the positrons in the scattering cell. Preliminary results of simulations run with a modified version of a Monte Carlo code, that was originally employed for studying E × B discharges in swarm physics (Brennan *et al.*, 1990), are found to be in quite good agreement with those predicted using Eq. (2.27) and the method of Hamada and Sueoka (1994), thereby giving us more confidence in their validity. We note that this test pertains only to argon and krypton, for which complete cross section sets (theory) exist (see later.)

The forward angle scattering effect can, in principle, be corrected for, if the angular discrimination of the apparatus is known and provided appropriate elastic differential cross sections for the target of interest are available at each energy (Sullivan *et al.*, 2011). To achieve this, it is enough to integrate the elastic differential cross section $d\sigma_{el}(\theta)/d\theta$ of the species in question at a given energy in the range 0-θ_s:

$$\sigma'_{\mathrm{el}} = 2\pi \int_0^{\theta_s} \frac{d\sigma_{\mathrm{el}}(\theta)}{d\theta} \sin\theta \, d\theta \,, \tag{2.28}$$

where θ_s is the angular discrimination at that energy (as given in Table 2.5), and in the full angular range 0-180°:

$$\sigma_{\mathrm{el}} = 2\pi \int_0^{\pi} \frac{d\sigma_{\mathrm{el}}(\theta)}{d\theta} \sin\theta \, d\theta \,. \tag{2.29}$$

The ratio of the cross section of Eq. (2.28) to that of Eq. (2.29) represents the desired correction factor to the measured total cross section at that positron energy, accounting for the forward angle scattering effect. By repeating this calculation at all measured energies, a table of the forward angle scattering corrections as a function of the scattering energy can, thus, be obtained.

However, unfortunately, absolute differential cross sections, either theoretical or experimental, are typically unknown for the targets investigated in this thesis, so that a correction for this effect cannot be made at this time. The total cross sections we report in this dissertation, therefore, represent a lower bound on the exact values, particularly at the lowest energies where the angular discrimination is largest (see Table 2.5).

To highlight the important role played by forward angle scattering effects on the measured total cross sections, the ANU group showed in a recent paper (Sullivan *et al.*, 2011) that earlier measurements from the Detroit group (Kauppila *et al.*, 1976; Dababneh *et al.*, 1980), on argon and xenon, could be reconciled with their own, if the Detroit data was corrected for the forward angle scattering effect due to an angular discrimination of 20° at each energy. While this is a crude approximation, as the angular discrimination is actually energy-dependent, it nonetheless makes the point for the importance of this effect. In another paper, again by the ANU group (Makochekanwa *et al.* (2011), estimates of the angular discrimination, here affecting their measurements on krypton, were used together with cross sections from the relativistic optical potential method (Chen *et al.*, 2008) to quantify the forward angle scattering effect on their measured total cross sections. That correction turned out to vary between 19% at 0.5 eV and 5% at 8 eV. Makochekanwa *et al.* (2009) also calculated that the same correction for the ANU data on formic acid is ~45% at 4 eV, but becomes negligible (i.e. <1%) above 15 eV. In the same paper they further reported that the correction for water, instead, amounts to ~67% at 0.5 eV and is still 12.5% at 60 eV. In a subsequent paper by the same team (Jones *et al.*, 2011), a similar approach was undertaken with argon and neon as the targets. The corrections in this case ranged from 16.3% at 0.3 eV to 2.4% at 8.5 eV, for the experiment on argon, and varied between 24% at 0.3 eV and 0.6% at 12 eV for those on neon. This clearly demonstrates that the correction for the forward angle scattering effect can be fairly large, especially at the lower energies, so that uncorrected measured data can be much lower in magnitude than their real cross section.

We note here that corresponding measurements, for some of these atomic targets, were carried out with the spectrometer in Trento and that they agree with those reported by the ANU group (uncorrected) to within typically ~±3% over almost the entire common range of investigated energies (see Section 2.1.4 for the present data on argon and krypton). This suggests that the angular discrimination correction for the measurements undertaken with the Trento apparatus, must be very close to that for the experiments conducted with the ANU beamline in the common energy range (compare Table 2.5 and Table 2.9). We reiterate that this is a quite remarkable result given that the two spectrometers have very different designs (Surko *et al.*,

2005). It is probably not unreasonable to assume that the Trento apparatus might also show a similar performance with other targets, although in reality this would need to be studied further.

A more quantitative and thorough discussion for the experimental angular discrimination, and its effect on the measured TCSs, can be found in Sullivan *et al.* (2011).

2.1.3.5 Overall uncertainties

In this dissertation all the cross section results, that are plotted in the figures and listed in the tables, are always provided along with their corresponding uncertainties. However, these uncertainties represent only the statistical component of the overall error. Here, we therefore note that the absolute uncertainties on our measurements are usually evaluated as the square root of the quadratic sum of all the contributing errors. These include:

- the statistical uncertainties on the data, estimated as one standard deviation of the average TCSs from each run. These are usually smaller than ~10%, and are ~5% on average. However, we did sometimes find them to span the ~2-12% range, depending on the positron energy, with the largest errors typically occurring at the lowest energies.
- the uncertainty in the thermal transpiration corrections (<1%).
- the uncertainty related to the value of L and its correction for the effective positron path length increase (<2%).
- the accuracy in the measured value of T (error <0.4%).
- the resolution of the absolute pressure readings (error ~0.3%, as per the manufacturer's specification).

A full discussion of the origin, and of the evaluation techniques, for these contributions can be found in Dalba *et al.* (1979) and in the references cited therein.

The overall uncertainties are estimated to be generally within the ~5-15% range, and are normally lower at higher energies and higher at the lower energies. From the set of uncertainties listed above, we see that the most important contribution to the total uncertainty on the TCS data stems from the statistical uncertainty. We stress that this could be readily improved by simply using a radioactive source with a higher activity, if funds for the purchase of such a source were available. The present apparatus is designed to accept sources up to 50 mCi, while most of the results presented here have been performed when the activity of the source was ~2 mCi. Therefore, all else being equal, a 50 mCi source would reduce the statistical count rate noise, over what we can typically now achieve, by a factor of ~5. Secondary uncertainties, such as those related to the correction for the effective path length increase and that in the thermal transpiration correction, are treated as additional sources of systematic error. They do not, however, contribute significantly to the overall systematic error on the total cross section measurement. Taking all these considerations into account, a 50 mCi source might lower our present errors by around a factor of 4 if it were available.

2.1.4 Validation of our experimental techniques and apparatus performance

As a standard practice in the Trento laboratory, in order to check for the validity of our measurement techniques and procedures, the performance of the spectrometer is periodically verified by carrying out preliminary measurements on target systems, whose positron total cross sections are considered to be well known or might even have been benchmarked. Such "well-characterised" or standard systems might be drawn from the noble gases (Jones *et al.*, 2009; 2011; Makochekanwa *et al.*, 2011), such as argon and krypton. In addition, N_2 has also been used as an internal reference gas for routine self-consistency checks of the apparatus performance, from the validity and reproducibility of its absolute cross section as measured over a time frame of months or even years apart.

In the following two subsections we report on the present total cross sections for positron scattering from two of these gases, namely argon and krypton. The results for N_2, instead, will be discussed later in Chapter 4.

2.1.4.1 Positron scattering from argon

The measurements on argon were carried out with a 1 μm-thick W-moderator, at a time when the activity of the radioactive source was ~1.5 mCi. A high-purity sample (≥99.998%), provided by Air Liquide, was used as our argon source. The manometer model 627B, operating at 45 °C, was employed during these measurements to read the gas pressure in the scattering cell which typically spanned the 5-9 × 10^{-3} Torr range. As the target gas in the scattering cell was at room temperature (~22.5 ± 1 °C), the thermal transpiration correction to the data amounts to ~+3% at most. This was calculated by using a value of 3.41 Å for the argon hard-sphere diameter from Liang (1953). In addition, for incident positron energies from 0.3 to 30.2 eV, the magnetic field was B ~ 11 G, so that the increase in L was ~+5.5%, whereas for energies between 35.2 and 50.2 eV, B ~ 4 G, leading to an increase in L of ~+2%.

The present total cross section results for positron collisions with argon are given in Table 2.6, for energies in the range 0.3-50.2 eV, together with the statistical uncertainty at each energy. Those uncertainties typically lie in the interval 0.5-3.3% (1σ) throughout the range of investigated energies, whereas the overall uncertainties are between 5-12%. The present data is also shown in Fig. 2.23, where it is compared with (a) previous experimental results and (b) a selection of the available calculations.

Firstly, we observe in Fig. 2.23 that the present total cross section strongly decreases (monotonically) in magnitude as the positron energy increases up to about 1 eV. We believe that this low-energy behaviour is likely due to the relatively large dipole polarisability α = 11.07 a.u. (Hohm and Kerl, 1990) of the argon atom, leading to a strong attractive scattering potential for the incident positron. This, in turn, enhances the probability of scattering that is manifested by the increasingly larger magnitudes of the total cross section towards the lowest energies. The opening of the

positronium formation channel is also evident in Fig. 2.23, as a dramatic increase in the magnitude of the total cross section in the vicinity of its threshold Ps = 8.96 eV. The subtle change in the total cross section slope near the first ionisation potential IP = 15.76 eV (Carman, 1989), instead, is believed to be indicative for the opening of that direct ionisation channel.

Previously, positron-argon scattering has been experimentally investigated many times (Canter *et al.*, 1973; Jaduszliwer and Paul, 1974; Kauppila *et al.*, 1976; Coleman *et al.*, 1976; 1980; Sinapius *et al.*, 1980; Charlton *et al.*, 1984; Kauppila and Stein, 1990; Jones *et al.*, 2011). By comparing now in Fig. 2.23(a), the present results with those from the previous measurements, we find only a fair or, in some cases, even marginal

Table 2.6. The present total cross sections for positron scattering from argon, along with the corresponding statistical uncertainties (±1σ).

Energy	TCS (10^{-20} m^2)		Energy	TCS (10^{-20} m^2)	
(eV)	Average	Error	(eV)	Average	Error
0.30	14.86	0.33	2.95	3.63	0.05
0.35	12.87	0.16	3.20	3.75	0.07
0.40	11.56	0.02	3.45	3.72	0.03
0.45	10.94	0.36	3.70	3.59	0.04
0.50	9.85	0.17	3.95	3.70	0.12
0.60	8.03	0.08	4.20	3.81	0.12
0.70	6.73	0.09	4.45	3.61	0.32
0.80	6.11	0.00	4.70	3.74	0.13
0.90	5.46	0.04	4.95	3.73	0.08
1.00	5.13	0.07	5.20	3.61	0.12
1.10	4.62	0.09	6.20	3.55	0.09
1.20	4.30	0.07	6.70	3.61	0.05
1.30	4.14	0.06	7.20	3.62	0.01
1.40	3.95	0.07	8.20	3.81	0.02
1.45	4.05	0.10	9.20	4.16	0.06
1.50	3.98	0.04	10.20	4.86	0.09
1.55	4.09	0.12	11.20	5.26	0.29
1.60	3.91	0.05	12.70	5.86	0.08
1.70	3.95	0.07	15.20	6.43	0.13
1.80	3.93	0.05	17.70	6.59	0.06
1.90	3.88	0.05	20.20	6.63	0.05
1.95	3.77	0.08	22.20	6.85	0.11
2.00	3.76	0.06	25.20	6.98	0.10
2.05	3.83	0.10	27.20	7.14	0.03
2.20	3.91	0.05	30.20	7.26	0.06
2.30	3.74	0.04	35.20	7.44	0.15
2.45	3.89	0.10	40.20	7.93	0.37
2.60	3.69	0.10	45.20	8.03	0.07
2.70	3.73	0.08	50.20	7.72	0.05

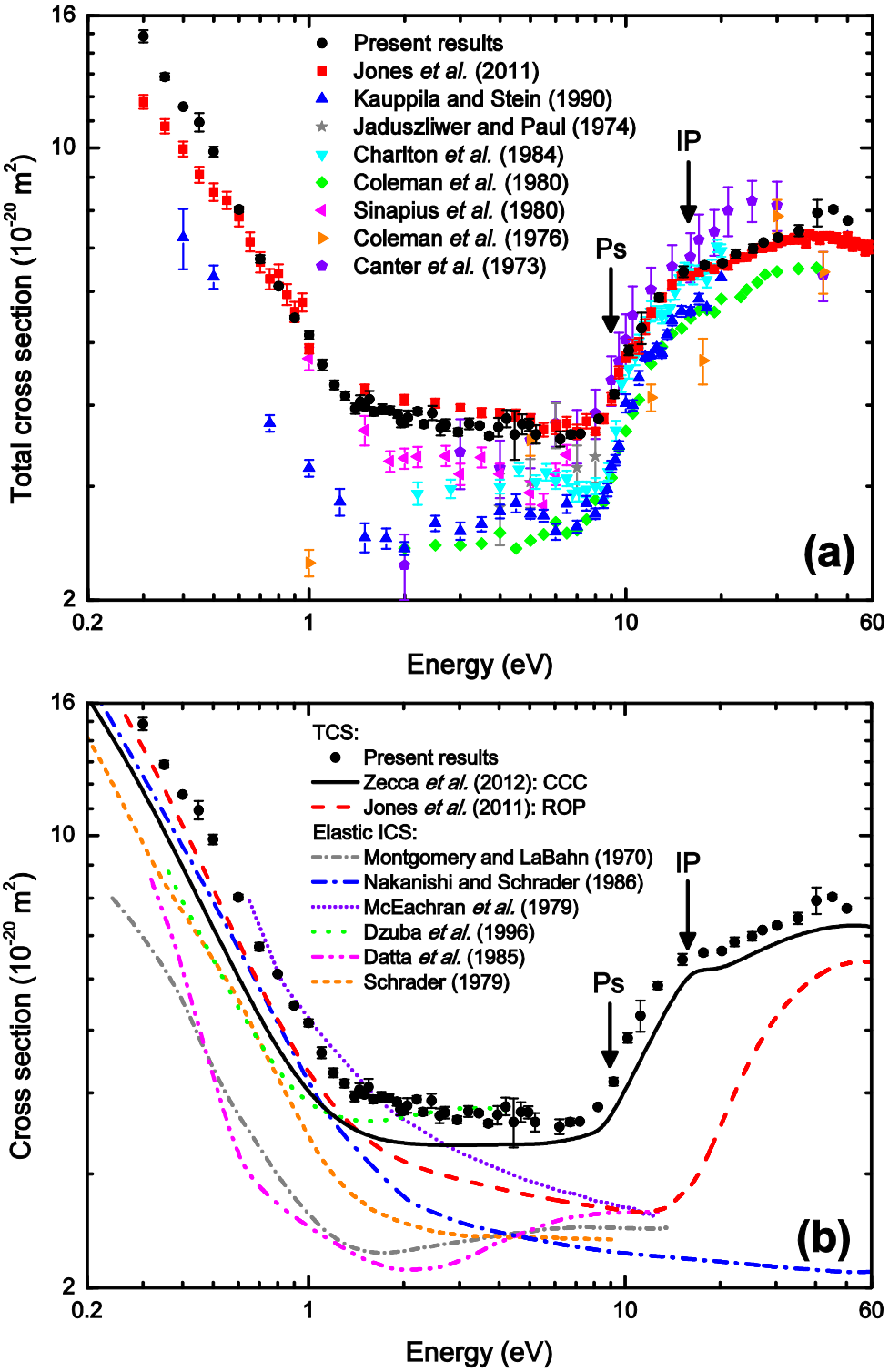

Fig. 2.23. The present positron-argon total cross section results compared with (a) previous experiments and (b) calculations. The black arrows labelled "Ps" and "IP" denote the positronium threshold and the first ionisation potential of argon, respectively.

level of agreement over the common energies. The only real exception to this general statement, however, is when we compare to the data of the ANU group (Jones *et al.*, 2011) (see below). In general the level of accord between the various groups is better above Ps, but it does progressively worsen towards the lower energies. We believe this discrepancy with the previous low-energy data can be explained as being due to those earlier measurements suffering from a larger angular discrimination correction compared to the present results, or a component due to an incorrect beam energy calibration by the earlier experiments cannot also be ruled out.

Positron collisions with argon have also been extensively studied from a theoretical perspective, with calculations of the elastic integral (Massey *et al.*, 1966; Montgomery and LaBahn, 1970; McEachran *et al.*, 1979; Schrader, 1979; Datta *et al.*, 1985; Nakanishi and Schrader, 1986; Jain, 1990b; Nahar and Wadehra, 1991; Baluja and Jain, 1992; Dzuba *et al.*, 1996) and total cross section (Jones *et al.*, 2011; Zecca *et al.*, 2012) having been reported in the literature. The selection of those results plotted in Fig. 2.23(b) differs mainly in the magnitude of the respective computations, but their low-energy shape is fairly similar. In effect, almost all of them can qualitatively reproduce the trend of the present total cross section below the positronium threshold, although they are usually somewhat lower in magnitude compared to our data. We note that the theory of Nakanishi and Schrader (1986) fits quite well the present TCS below ~1 eV, to within the overall error bars, however, the only model that appears to do quite a good job at reproducing the shape of the present data, over its entire energy range, particularly above the positronium formation, is the CCC calculation by Zecca *et al.* (2012).

Let us now comment in more detail about the interesting comparison between the present data and that from the ANU group (Jones *et al.*, 2011). This is justified since it is clear from Fig. 2.23 that they are the only data sets which, in general, are in very good agreement over most of the common energy range and to within their respective overall errors. Note that the present data are uncorrected for the forward angle scattering effect, whereas those of the ANU group have been corrected for it (see Section 2.1.3.4). Of course we could correct the present data for this by following the approach outlined in Section 2.1.3.4, and on doing so we estimate an increase in our measured total cross sections of ~12% at 0.3 eV, ~4% at 10 eV and ~2% at 30 eV. However, the problem is that currently there are no experimental measurements of the elastic differential cross sections for argon, so that the validity of the available theoretical results (Zecca *et al.*, 2012; Jones *et al.*, 2011) cannot be independently verified. Therefore, whether theory is to be preferred to experiments at the differential cross section level still remains an open issue. In addition, which theory is to be preferred (they give different results) is an open question. As a consequence, we prefer to leave the present measurements uncorrected until this matter has been resolved.

Nonetheless, given the actual level of accord in Fig. 2.23(a) between the current total cross sections and those of the ANU group is really very good, a case might well be made for considering the positron-argon scattering total cross sections to have been experimentally "benchmarked". Hence this

scattering system is a good choice for validating the apparatus and our techniques.

2.1.4.2 Positron scattering from krypton

We present in this section the current total cross section results for positron impact on krypton. These measurements were undertaken on a high-purity krypton sample (≥99.998%), purchased from Air Liquide, and by employing a 1 μm-thick W moderator in conjunction with the radioactive ^{22}Na isotope source (activity ~1.5 mCi). The pressure in the scattering region during the experiment was measured with the model 627B manometer and was in the 2-7 × 10^{-3} Torr range. This manometer operated at 45 °C, which is different to the room temperature at which the gas in the cell was held (~22.5 ± 1 °C). Therefore a thermal transpiration correction of up to ~+3%, calculated with an estimate of 3.57 Å (Barker *et al.*, 1974) as the hard-sphere diameter of krypton, was applied to the total cross section data. The correction for the effective positron path length increase was estimated to be ~5.5%, for energies between 0.2 and 30.15 eV (B ~ 11 G), and ~2% for energies above 30.15 eV (B ~ 4 G).

The present positron-krypton TCSs are listed in Table 2.7, and plotted in Fig. 2.24 along with results from (a) previous experiments and (b) computation results. The energy range of the current measurements is 0.2-50.15 eV. In Table 2.7 and Fig. 2.24 only the statistical uncertainties on our data are given: these are in the range 0.7-4.7% (1σ). However, we estimate the overall uncertainties to be in the range 5-10%, with the highest errors occurring at the lowest energies.

Similar to what we observed when argon was the target (see previous subsection), here too the total cross section increases significantly in magnitude as the incident positron energy decreases below the positronium formation threshold (Ps = 7.35 eV). As before, this behaviour of the low-energy cross section is ascribed to the moderately strong dipole polarisability α = 16.8 a.u. (Horbatsch *et al.*, 1983) of the krypton atom. The marked increase in the total cross section magnitude near the positronium threshold, is of course due to the positronium formation channel becoming open.

By comparing the present TCSs with the earlier ones (Dababneh *et al.*, 1980; Sinapius *et al.*, 1980; Charlton, 1985; Canter *et al.*, 1973; 1974; Jay and Coleman, 2010, Makochekanwa *et al.*, 2011) in Fig. 2.24(a), we find that the level of accord is, in general, fairly good at energies above Ps, to within the respective total uncertainties. Below that energy, in fact, the agreement remains quite good with the data of Sinapius *et al.* (1980), Charlton (1985) and Makochekanwa *et al.* (2011), but it is now very poor when compared against the results from Dababneh *et al.* (1980), Canter *et al.* (1973; 1974) and Jay and Coleman (2010). These discrepancies might again be explained, at least in part, in terms of the present measurement being affected by a somewhat smaller angular discrimination correction compared to some of those earlier experiments.

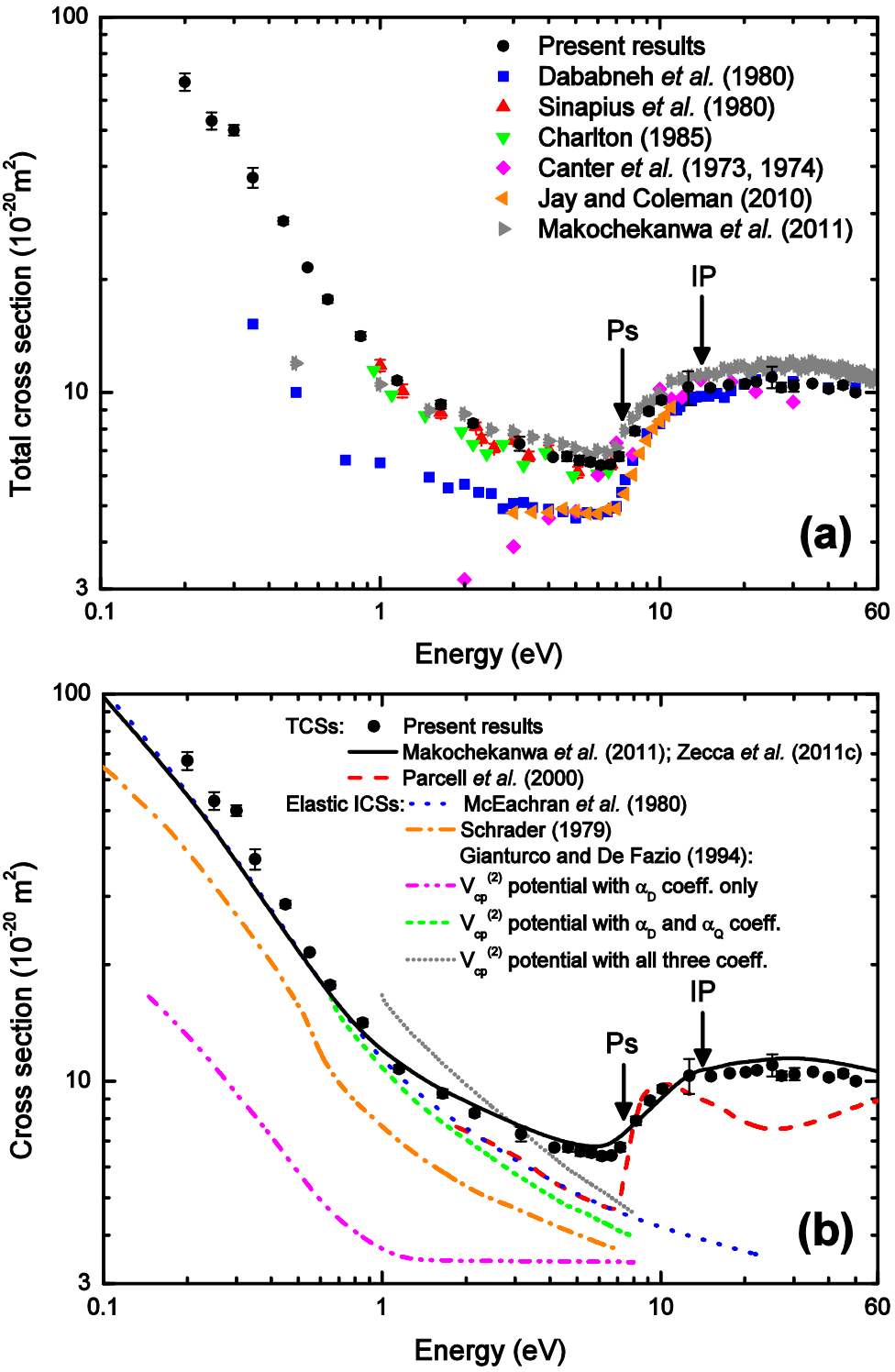

Fig. 2.24. The present total cross sections for positron scattering from krypton compared with (a) previous experimental results and (b) model calculations. The energy thresholds corresponding to the opening of the scattering channels of positronium formation and direct ionisation are indicated by the black arrows labelled "Ps" and "IP", respectively.

Table 2.7. The present positron-krypton total cross sections. Given also are the statistical uncertainties at the one standard deviation level.

Energy	TCS (10^{-20} m^2)		Energy	TCS (10^{-20} m^2)	
(eV)	Average	Error	(eV)	Average	Error
0.20	67.17	3.61	6.65	6.43	0.03
0.25	52.90	2.77	7.15	6.75	0.17
0.30	49.97	1.59	8.15	7.90	0.20
0.35	37.38	2.27	9.15	8.90	0.18
0.45	28.62	0.59	10.15	9.54	0.21
0.55	21.53	0.14	12.65	10.33	1.07
0.65	17.70	0.37	15.15	10.29	0.14
0.85	14.14	0.33	17.65	10.48	0.11
1.15	10.76	0.22	20.15	10.54	0.03
1.65	9.29	0.24	22.15	10.67	0.12
2.15	8.27	0.17	25.15	10.99	0.72
3.15	7.30	0.31	27.15	10.32	0.28
4.15	6.73	0.07	30.15	10.42	0.37
4.65	6.75	0.19	35.15	10.56	0.04
5.15	6.59	0.19	40.15	10.22	0.16
5.65	6.53	0.16	45.15	10.45	0.21
6.15	6.40	0.14	50.15	10.00	0.15

Note that the current data plotted in Fig. 2.24 and tabulated in Table 2.7, are uncorrected for forward angle scattering effects. Of course we could correct our data for this effect, in a similar manner to that pursued by Makochekanwa *et al.* (2011), by adopting the approach described in Section 2.1.3.4. On doing so we determine that the measured total cross sections should be increased by ~15% at 0.2 eV, ~6% at 10 eV and ~3% at 30 eV to account for the forward angle scattering effect. However, the agreement between the currently available experimental and theoretical elastic differential cross sections for krypton (Makochekanwa *et al.*, 2011) is not uniformly good at all energies and in some cases it is actually rather poor. Hence, we believe it is premature to use these elastic differential cross sections in order to make that correction. However, once this issue is resolved in the future, there is no reason why the present TCSs could not be corrected for the forward angle scattering effect.

Among the experiments shown in Fig. 2.24(a), we observe that the results of the ANU group (Makochekanwa *et al.*, 2011) are in pretty good agreement with the present data, notwithstanding the fact that their TCSs are corrected for forward angle scattering effects, whereas the present data are not. This is why the present total cross sections are systematically lower than those of the ANU group by ~5-10% in the energy range ~3-50 eV. However, allowing for the total errors on the measurements of both groups, these differences are not so significant and will lessen even further when our TCSs are corrected for the previously described forward angle scattering effect.

With respect to the available computations on positron-krypton collisions (Schrader, 1979; McEachran *et al.*, 1980; Gianturco and De Fazio 1994; Parcell et al., 2000; Makochekanwa *et al.*, 2011; Zecca *et al.*, 2011c), we observe that there is quite a large discrepancy among the different theories. However, the calculation that does the best job at reproducing the present total cross sections is clearly the CCC theory by Makochekanwa *et al.* (2011) and Zecca *et al.* (2011c), which falls within the uncertainty on our data throughout most of the range of energies investigated in this experiment.

The main outcome of these comparisons is the pretty good accord achieved between the present results, the ANU data (Makochekanwa *et al.*, 2011) and the CCC theoretical results (Makochekanwa *et al.*, 2011; Zecca *et al.*, 2011c). As a consequence a case might well be made for considering positron-krypton scattering total cross sections to have been "benchmarked". This is why this system also makes a good choice for validating the apparatus performance and our techniques.

2.2 Atomic and molecular buffer-gas trap and positron beam apparatus (Australian National University)

The beamline facility at the Australian National University (ANU) was developed in order to investigate positron scattering from atoms and molecules (Sullivan *et al.*, 2008b). The experiment is based on a transmission technique, in which the positron beam is formed in a strong magnetic field by means of a modified version of a Penning-Malmberg trap (Murphy and Surko, 1992). The design of this apparatus is based on the experimental ideas developed by Cliff Surko at the University of California in San Diego, however, unlike other equipment employing this scheme (see e.g. Clarke *et al.*, 2006; Cassidy *et al.*, 2006), this is the first to have been planned specifically for low-energy positron scattering measurements. For this reason some of the aspects of the ANU spectrometer have been expressly designed in order to optimise its operation for this purpose.

Experimental systems using a buffer-gas trap in a strong magnetic field, to produce a pulsed beam, present several practical advantages. For example, positron scattering in intense magnetic fields enables the direct measurement of cross sections for specific scattering states and also their angular distributions (Sullivan *et al.*, 2002). In addition, the implementation of a buffer-gas trap also allows cross section measurements with a very high energy resolution, that, in principle, can be as low as 18 meV (FWHM) and be tunable over a quite wide positron energy range (from ~0.05 eV up to 200 eV) (Gilbert *et al.*, 1997; 2000; Kurz *et al.*, 1998). Earlier experimental configurations, instead, used to employ solid moderators to generate the slow positrons, and use weak magnetic fields (up to ~10 G) to confine and transport the beam, which resulted in a lower positron intensity and a somewhat poorer energy resolution (~0.3 eV or worse) (see e.g. Charlton and Humberston, 2001 and references therein). These constraints in the previous experimental investigations, limited to some extent their capability of making very accurate measurements of scattering cross sections and precluded also some specific types of studies.

Given the advantages that a "Surko-type" apparatus offers, it is quite likely that future positron-based devices, for both fundamental research and commercial application, will be based on buffer-gas positron accumulators in conjunction with a high magnetic field (Murphy and Surko, 1992; Surko *et al.*, 2000). However this technique is not without its experimental limitations, as we will see shortly. Nonetheless, the successful operational performance of the positron beamline at the ANU has been demonstrated by some recent publications on positron scattering from quite a few atomic and molecular targets (Sullivan *et al.*, 2008a; 2008c; Caradonna *et al.*, 2009; Makochekanwa *et al.*, 2009; 2011; Jones *et al.*, 2011), and we now describe its essential elements in the remainder of this chapter.

2.2.1 Description of the apparatus

The experimental apparatus at the ANU, that was used for a few of the measurements undertaken as a part of the present thesis (see Section 6.3), has been described in detail in the paper by Sullivan *et al.* (2008b) with its original design being shown in Fig. 2.25. This beamline is formed in several sections, which are clearly discernible in Fig. 2.25, each having a specific role in the operation of an experiment: the source and moderation stage, where the slow positrons are produced, the buffer-gas trap, which accumulates the positrons and prepares a pulsed positron beam, the scattering region, where the positrons interact with the target atoms or molecules, the retarding potential analyser, which examines the beam energy distribution, and finally the detection system that counts the positrons exiting the scattering cell.

The low energy positrons are produced by a radioactive ^{22}Na source in conjunction with a solid neon (Ne) moderator and are then confined in their radial direction by the strong and typically uniform magnetic fields (~500 G) that are present in the main sections of the experimental setup. The magnetic fields also aid in guiding the positron beam into a set of electrodes containing a small amount of a buffer-gas mixture, a configuration now widely known as a Surko trap (Murphy and Surko, 1992). In this three-stage trap the positrons are first trapped in a potential well structure, then cooled to room temperature by means of inelastic interactions with the molecules of the primary buffer gases N_2 and CF_4, and at last are released as an almost monochromatic pulsed beam with some well-defined energy (Gilbert *et al.*, 1997). After passing through a first small retarding potential analyser (RPA), the positrons subsequently enter a cell containing the target of choice, where they undergo collisions with the atoms or molecules of the target gas. Finally, before being collected by a micro-channel plate detector, the positron beam is analysed in terms of its energy distribution by a second, larger, retarding element. This electrode is placed downstream from the scattering cell but is still within another strong magnetic field (generally ~500 G), which is different to and independent from that present in the rest of the spectrometer. Note that this second magnetic field is also adjustable in magnitude depending on the specific desired measurement. A central computer controls all the operations occurring during a standard experiment.

As we will see later on more in detail, it is precisely by taking advantage of the peculiar energy properties of beams in a high magnetic field (Sullivan *et al.*, 2002), and by determining the RPA spectrum of the transmitted positron beam intensity, that it is eventually possible to determine the cross section of interest for a range of scattering processes (Sullivan *et al.*, 2008b). As the positrons are in a magnetic field B their energy can be split into two components, parallel ($E_\parallel$) and perpendicular ($E_\perp$) to the direction of the magnetic field itself. The quantity $E_\perp/B$ is an adiabatic invariant in a uniform magnetic field and, therefore, a slow increase or decrease of the magnetic field will, in turn, either enhance or reduce the $E_\parallel$ energy spread. As a consequence, by varying the intensity of the respective magnetic fields

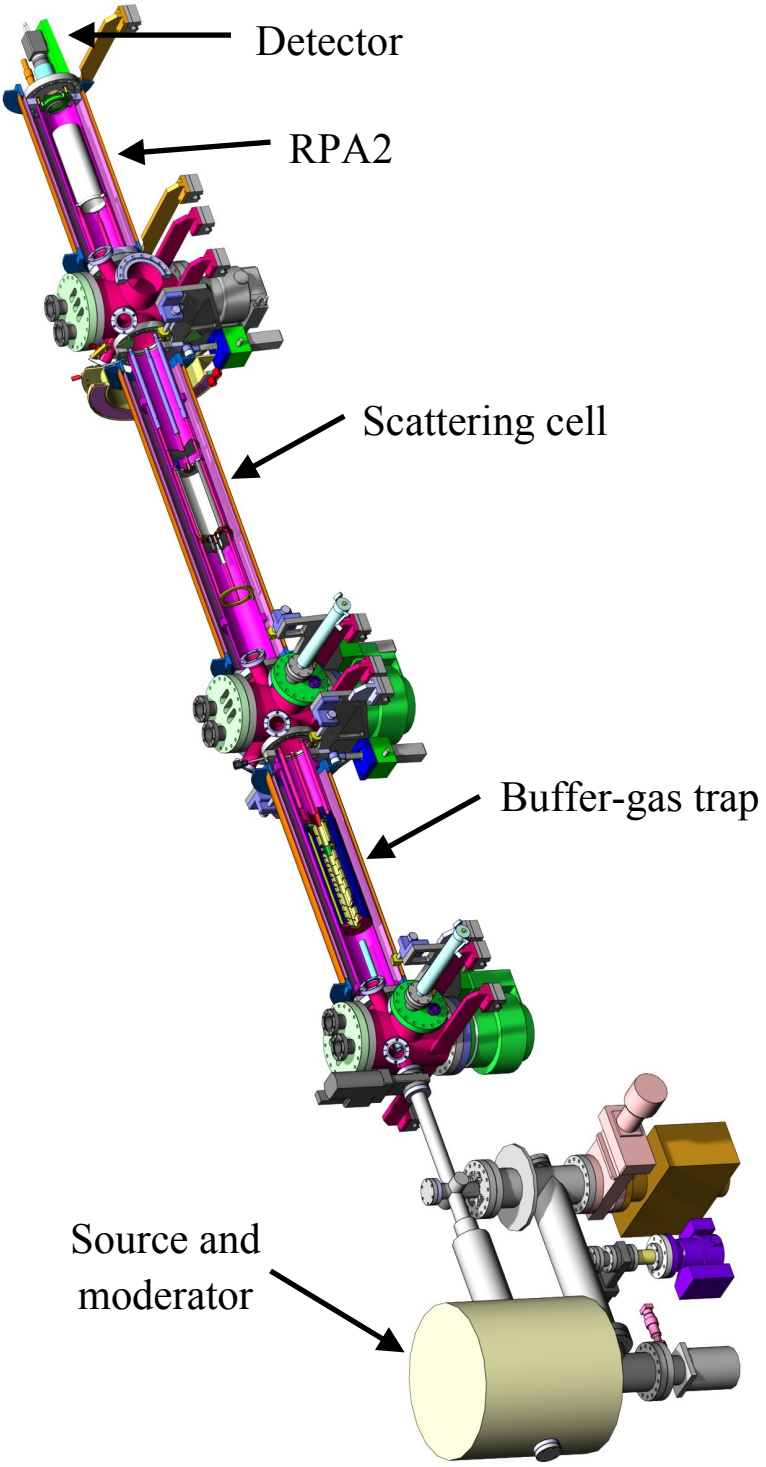

Fig. 2.25. Schematic diagram of the positron beam apparatus at the Australian National University. The various stages of the spectrometer are clearly visible; from left to right: the source and the moderator, the buffer-gas trap, the scattering cell, the retarding potential analyser (RPA2) and the detector.

between the scattering and the RPA region it is in principle possible to separate out the elastic and inelastic scattering channels.

We illustrate and describe now in more detail each section of the apparatus, with the operational functions and the experimental techniques employed during the measurements being outlined in the following section. Note that some of the experimental methods and devices outlined in the description of the Trento spectrometer (Section 2.1) are the same as those for the ANU beamline. Therefore, we do not repeat those details again here, rather we refer you to the relevant earlier section in this chapter of the present thesis.

2.2.1.1 The source and moderation stage

The positron source in this experimental facility is also a radioactive ^{22}Na isotope, that had an activity of ~35 mCi at the time of the measurements undertaken for this thesis (see Section 6.3). The isotope is held in a specifically designed mounting arrangement, mounted on top of a coldhead, and is surrounded by elkonite blocks (Fig. 2.26) in order to provide primary shielding from the high energy gamma rays produced by the β^+ decay reaction (see Section 2.1.1.1). Elkonite, which is a very dense material, is a copper-tungsten alloy.

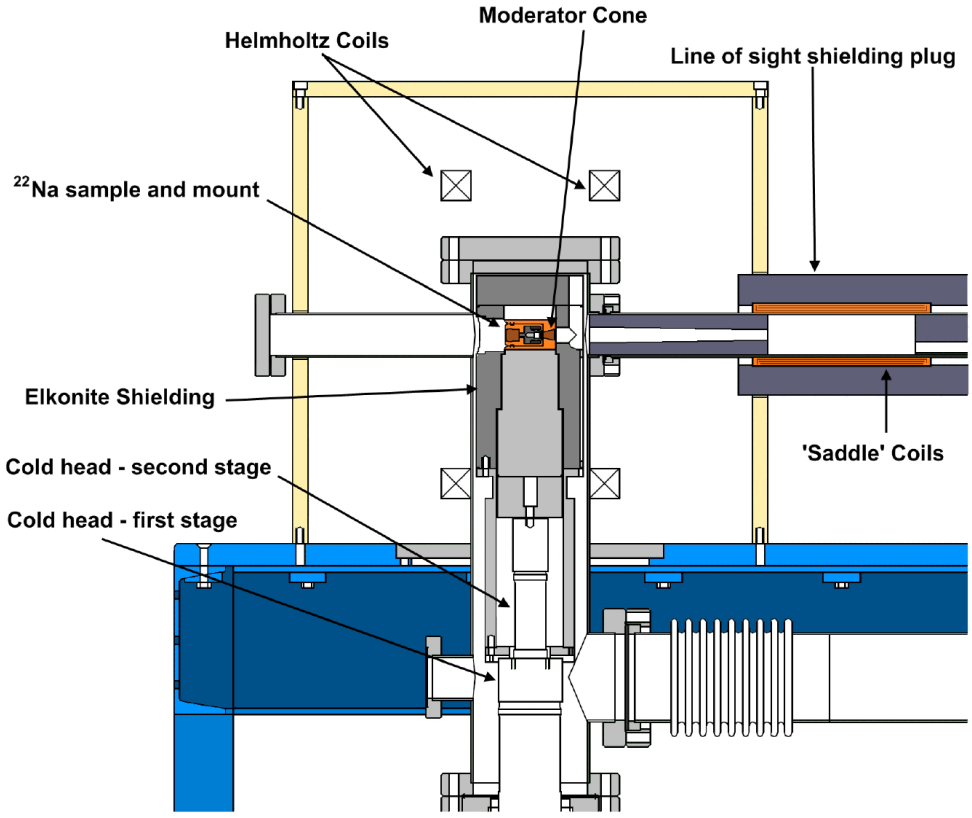

Fig. 2.26. A schematic drawing of the section of the beamline containing the radioactive source and the moderator (Jones, 2010).

As noted previously, the positrons are emitted by the isotope with a wide range of energies, so that the positron beam needs to be slowed down and made as monochromatic as possible, before it can effectively be used for the low-energy scattering experiments we are interested in. To this end, a solid neon moderator (Mills and Gullickson, 1986) is used. A cone-shaped copper block, placed on the cold head unit, in front of the radioactive source forms the surface for the moderator. As the melting temperature of neon is ~9.5 K under vacuum, it has to be maintained at a very low temperature and this is achieved by means of a cryogenic coldhead unit (T ~ 6-8 K). The present coldhead is a DE-204 cryo-cooler, as built by Advanced Research Systems, with a high cooling capacity such as to reach a ~5 K base temperature. The cryo-cooler is a system based on the compression and expansion of high purity, high pressure helium gas. Due to the large thermal inertia of the assembly that the coldhead is in physical contact with, the lowest achievable temperature is usually ~7 K, which is low enough to grow a solid neon moderator. A heating element of adjustable power (~0.1-10 W), is used in order to maintain the temperature of the coldhead as stable as possible to within a few tenths of a degree.

The section of the system consisting of the moderator, the source container and the gas handling system for growing the moderator is commercially available and was purchased from First Point Scientific Inc. (http://www.firstpsi.com/). This assembly is housed in a cylindrical containment vacuum chamber, together with the radioactive source and the cold head, to form one endstation of the beamline (see Fig. 2.26). A thick lead layer surrounds the entire assembly to provide protection from the ionising gamma radiation. The vacuum in this stage of the apparatus is generated by a Pfeiffer TMU 071P turbomolecular pump (N_2 volume flow rate 60 l/s, rotational speed 60,000 rpm) coupled to a rotary vane vacuum pump. This backing pump can generate an initial vacuum of ~10^{-3} Torr in standard operating conditions. A Gamma Vacuum TiTan 30 ion-pump (pumping speed 100 l/s), also helps in producing the final vacuum. A typical background pressure in the 10^{-9} Torr range is achievable, with this pumping system in this section of the apparatus. However, under operating conditions, owing to the presence of the Ne gas used for growing the moderator, the pressure rises into the low 10^{-7} Torr range.

The positron beam is radially confined by a magnetic field of ~80-100 G, generated by two Helmholtz coils present in the source and moderator stage (see Fig. 2.26). The positrons leave the moderator with an energy that can be precisely set with some electrostatic elements, and then enter a narrow tube surrounded by a solenoid, producing a ~30 G field, which leads to the trap stage.

2.2.1.2 The buffer-gas trap

The moderated positron beam is now guided to the following stages of the apparatus, by means of magnetic fields generated by solenoid coils placed around the vacuum chambers. These solenoids are made of thick copper wire with a high current (~15 A) flowing through them, that produces a quite significant amount of heat owing to the Joule effect. In

order to avoid overheating and prevent potentially adverse effects on the apparatus and therefore the experiments, the solenoids are cooled using a chilled water jacket. The coils are thus maintained at a reasonably constant temperature of ~50 °C during the measurements.

The buffer-gas trap is formed by nine hollow cylindrical gold-plated copper electrodes that are electrically isolated from each other (see Fig. 2.27). In the first stage of the trap PEEK spacers located between the various elements are used to form a cylindrical sealed unit. The electrodes in the second stage are, instead, spaced by ruby balls in order to allow the buffer gas to diffuse into the trap from the outer housing. Despite all having similar geometrical shapes, the various electrodes have different lengths and internal diameters. The first three electrodes have an internal diameter of 1 cm, the length of the first element is 2 cm, whereas that of the other two elements is 4 cm. The electrodes *E*4 to *E*8 all share the same size: a larger internal diameter of 2 cm and a length of 3 cm. Lastly, the ninth electrode has an internal diameter of 2 cm, but its length is 6 cm. Each electrode is provided with its own electrical pins, to connect them to the external electronics supplies and the central computer. The voltages on the various elements can be conveniently set, so as to obtain a variable potential structure throughout the length of the trap, similar to a potential well. The entire trap assembly is supported by three stainless steel draw bars.

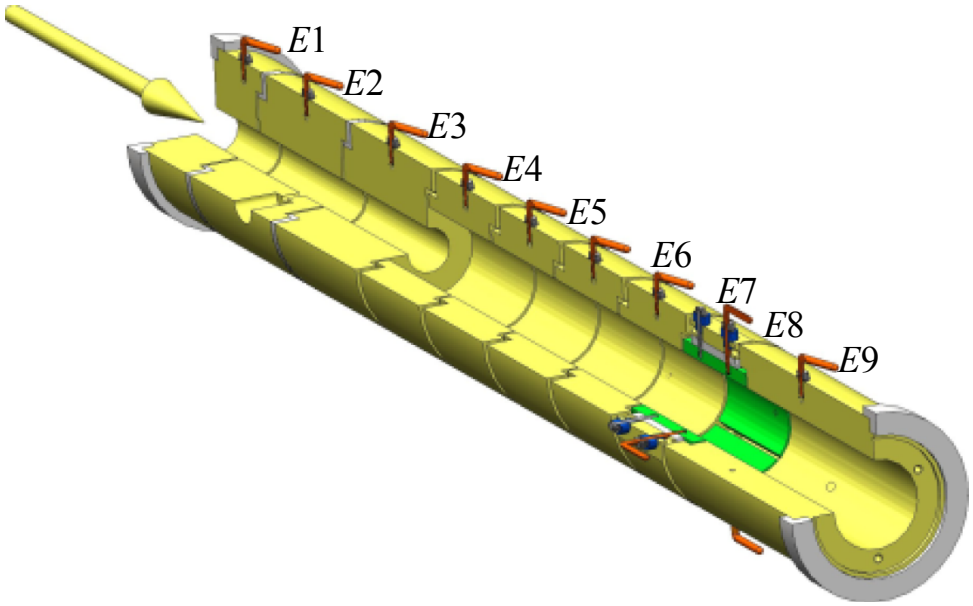

Fig. 2.27. Schematic design of the ANU buffer-gas trap (Sullivan *et al.*, 2008b). The trap consists of nine distinct electrodes (*E*) that are yellow coloured in the figure. The electrode corresponding to the rotating wall element is coloured green and is in position 6. The arrow indicates the direction of the positrons entering the trap.

A “rotating wall” electrode (Greaves and Moxom, 2008) is also included in the present configuration of the trap. This device is fabricated so that one of the elements has its inner wall azimuthally segmented into four parts, so that it is formed by four independent electrodes. By appropriately applying a rotating potential to the four inner segments of this electrode (*E*6), a rotating electric field is obtained. It was shown previously that in doing so, it is possible to radially compress the positrons that are confined in a cylindrical Penning-Malmberg trap (Greaves and Surko, 2000). If the frequency and amplitude of the rotating wall are properly set, in order to optimize the compression phase, this technique improves significantly the properties of the positron beam, such as its spatial distribution and the number of positrons per pulse (Greaves and Surko, 2002). The present location of the rotating wall element in the ANU trap was kept in position 6 throughout the current measurements.

Buffer-gases are admitted into the trap to define two distinct pressure regions, in order to trap and cool the positrons down to room temperature (Murphy and Surko, 1992). The buffer-gases used to achieve this effect are a mixture of molecular nitrogen (N_2) and carbon tetrafluoride (CF_4). N_2 is injected through an inlet present in *E*2, directly into the first part of the trap (*E*1 to *E*3) and then spreads into the other larger diameter electrodes (*E*4 to *E*9). The N_2 pressure at the entrance of the trap is ~0.1-1 mTorr, whereas the pressure of the gas reaching *E*9, by diffusion, is reduced by almost an order of magnitude. So, successively lower pressures of N_2 gas are found within the trap as you go from *E*1 to *E*9. The other buffer gas (CF_4), is admitted from the opposite side of the trap by diffusing into the chamber from the outer housing. The CF_4 pressure inside the trap is on the order of 0.01 mTorr. The pressure of the buffer-gases has to be optimised in order to maximise the cooling efficiency. Note also that the typical pressures of the “cooling gases”, in the last stage of the ANU trap, are somewhat higher compared to those usually employed in other conventional three-stage traps. As a consequence, the lifetime of the trapped positrons here is comparably shorter. Nevertheless this is not a shortcoming in the traps performance, since under normal operational conditions the trap cycles at a comparably higher frequency, as we will see in more detail in Section 2.2.2.2.

A solenoid generates a magnetic field of ~530 G in the trap region and confines the positrons in the radial direction. This magnetic field is known to be relatively uniform in intensity, to within a few percent, throughout the entire length of the trap. The vacuum in this part of the apparatus is achieved by means of two Pfeiffer TMU 521 P turbomolecular pumps (N_2 volume flow rate 510 l/s, rotational speed 33,000 rpm) situated at either endstation of the buffer-gas trap. Each turbo pump is coupled to a Pfeiffer DUO 20 rotary vane vacuum pump (pumping speed 20 m^3/h), producing a fore-vacuum of ~5×10^{-3} mbar. Differential pumping capillary tubes are present along the trap and between both the turbo pumps, in order to reduce the pressure gradient between both endstations of this stage of the system. This experimental precaution is required to try and avoid the trap gases leaking into the contiguous sections of the beamline (that is to the moderator and the scattering cell). However, in effect, a small amount of buffer-gas

(mostly N_2) penetrates into the upstream end of the trap, thereby causing some contamination of the Ne moderator over time (see Section 2.2.1.1). The background vacuum pressure in the trap section of the beamline is in the 10^{-10} Torr range in the absence of the trap buffer-gases. During the experiments, when the latter are injected into the trap, the pressure increases to ~10^{-6} Torr and ~10^{-5} Torr at the entrance and the exit ends of the trap stage, respectively. Finally, retractable "beamflags" are present within each endstation of the trap chamber. These elements are gold-plated copper discs, with a diameter of about 10 cm, that can be progressively inserted into (or pulled out of) the system to prevent part or the entire positron beam being transmitted. The aim of doing this is to occasionally check for the spatial distribution of the positron beam, by measuring the positron intensity as a function of the "beamflag" position. Another function of the "beamflags" is to check for the overall beam intensity.

2.2.1.3 The scattering region

In the next two stages of the beamline, the positron beam undergoes interactions with the target of interest and then an analysis of its energy distribution (see Fig. 2.25). These processes occur in the scattering cell and the second retarding potential analyser, respectively. Each of these elements is also immersed in a separate uniform magnetic field, generated by an independent solenoid, whose intensity can be varied. Note, however, that it is usually kept equal to that of the magnetic field in the trap stage, i.e. ~530 G. Vacuum in this part of the system is maintained by a turbomolecular pump (pumping speed 520 l/s), positioned at the junction between the trap stage and the scattering region, and by a further turbo pump (pumping speed 210 l/s) lying between the interaction chamber and the final vacuum chamber containing the RPA and the detector.

The design of the scattering cell assembly is schematically shown in Fig. 2.28. Also included in this figure are two other important features. The first, positioned just before the entrance of the scattering cell, is a small mesh cylinder of 15 mm diameter and 45 mm length (Fig. 2.28), whose potential can be set independently to that applied to the scattering cell. This electrode serves as a retarding element, with the aim of making a first energy scan of the positron beam immediately before the interaction region. The purpose of this is to check whether any background scattering events have occurred in the transmission region, between the trap and the scattering cell. If this is the case, it is possible to discard those positrons that have lost part of their energy in the parallel component after having left the trap, as a result of the elastic or inelastic collisions with the buffer gases emerging from the trap. With this experimental precaution any background scattering potentially influencing the cross section measurements is minimised.

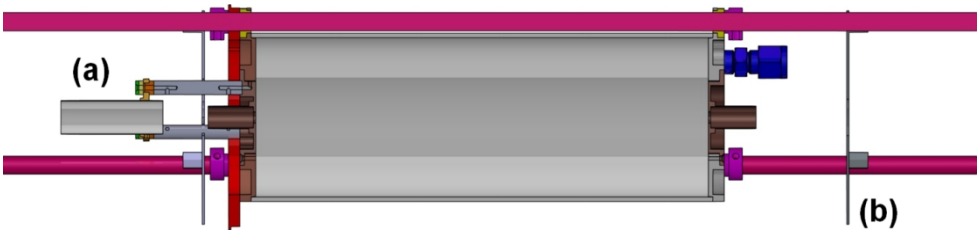

Fig. 2.28. Schematic drawing of the scattering cell, together with (a) the first retarding potential analyser and (b) a shielding mesh that prevents any voltage penetration from the scattering cell into the positron beam transport region (Sullivan *et al.*, 2008b).

The scattering cell is a 200 mm long gold-plated hollow copper cylinder, with an internal diameter of 90 mm, and entrance and exit apertures with a 5 mm diameter orifice (Fig. 2.28). The target gas is injected into this cell, through a small inlet situated at the exit of the cylinder. The present geometry of the cell was found to result in a well-defined symmetrical pressure profile. In fact, as the aperture diameters are small compared to the internal diameter of the cell, the pressure inside the cell is constant and uniform and falls off quickly at both ends. Indeed this drop in pressure is expected to be symmetrical throughout each aperture. This behaviour justifies the assumption that the effective positron path length, through the cell, can be considered to be equal to the geometrical length of the cell. The only exception to this is for any eventual correction accounting for the spiral motion of the charged particles in the magnetic field. This latter effect, however, is expected to be negligible in the present experimental configuration, as we will see later in this chapter. The pressure of the target gas in the scattering chamber is measured by a high accuracy (±0.05%) MKS model 690A Baratron capacitance manometer (resolution ~1×10^{-5} Torr, full range 1 Torr), operated at 45 °C.

Small cylindrical inserts, electrically connected to the scattering cell, are placed on the outside of each cell aperture. Their function is to avoid unwanted surface effects (e.g. stray potentials) to maintain the same potential in the scattering cell as at the exit and entrance apertures. Hence, any scattering that may occur immediately outside the cell takes place at the same energy as that on the inside. A Teflon collar surrounds the beginning of the scattering cell, in order to prevent the trap gases diffusing downstream from it, and becoming a possible source of additional background scattering. A supplementary mesh grid is additionally placed a few centimetres after the exit of the cell, in a perpendicular position with respect to the axis, to stop any possible voltage penetrating from the scattering cell into the next stage of the apparatus.

2.2.1.4 The retarding potential analyser

The RPA element is also immersed in a uniform (to within ~5% throughout the region of interest) magnetic field, with a field strength that has the capacity to be independently changed with respect to that in the

interaction region. This need arises, for instance, if cross section measurements of specific scattering channels are required (see Section 2.2.3.2.2). This RPA element is a 230 mm long meshed gold-plated copper cylinder, with a diameter of 70 mm. The purpose of the RPA is to carry out an analysis of the energy distribution of the beam and it is essential to enable one to accurately calibrate the energy scale and thus determine the energy zero. This analysis is achieved by scanning the retarding potential applied at the scattering cell first and then at the RPA element. The RPA also has another very important task. Namely it measures the energy of the beam in the axial direction of motion, and thus directly quantifies whether the positrons have lost some of their energy in the parallel direction as a result of elastic angular scattering or due to inelastic collisions.

2.2.1.5 The detection system

In the final vacuum chamber, a detector is positioned to collect the positron beam, after it has interacted with the target and has been energy-analysed. The detector in this case is a 40 mm diameter, double-stack, multi-channel plate. The multi-channel plate (MCP) is an electron multiplier with a continuous dynode structure (Ladislas Wiza, 1979), and has a similar operation to a channeltron (see Section 2.1.1.5). It consists of a 2-dimensional parallel array of very small electron multipliers.

The MCP unit is combined with a charge-sensitive pre-amplifier, a capacitively coupled trans-impedance amplifier, and counting electronics. These facilities allow the detection system to count the number of particles and to amplify the positron current collected by the MCP anode by a factor of ~10^7. This raises the current from the ~0.05 pA usually measured at the entrance of the detector, up to the μA range. The controlled data acquisition system of the central computer picks up and stores the signal. By integrating the positron signals, that have so been obtained, it is then finally possible to determine the relative positron current. Note that in order to establish values, with a good statistical accuracy, the positron signals are averaged over multiple pulses.

Finally, the pulses can also be imaged using a phosphor screen anode incorporated into the MCP assembly. This provides information about the size and the spatial density distribution of the positrons in the beam.

2.2.1.6 Computer control

The operation functions of the experiment, such as the trap control, voltage settings, pressure readings and data collection, are almost entirely under computer control. The various measurement functions are run by code developed within the National Instruments LabView software environment (http://www.ni.com/labview/), for use on a personal computer, and are then executed by another more sophisticated computer, a PXI-8186 Embedded Controller, purchased directly from National Instruments and which incorporates several interface hardware cards. The setting of the potentials on the various electrodes of the trap, and on the other electrostatic elements like the moderator, the scattering cell and the RPA analysers, is achieved by

means of digital-to-analog converters (16 bit, output ±10 V), coupled to fast, high voltage amplifiers (gain factor 10). The resolution in the voltages that can be applied to the various electrostatic elements can be as small as 3 mV, thus allowing one to carry out high-resolution measurements of the scattering cross sections.

2.2.2 Measurement procedures

In this section we now describe the procedures employed to carry out the measurements with the ANU beamline.

2.2.2.1 Positron moderation technique

The process of growing a Ne-moderator is entirely computer automated, and is guided through the different stages by commercial software developed specifically for this operation. The source of the moderator gas is a high-pressure bottle containing a high-purity (99.999%) Ne sample. This bottle is coupled to a pressure regulating valve, in order to decrease the gas pressure at the entrance of the gas management system to a few atmospheres, before injecting the gas into the vacuum system. Admission of the Ne into the system is controlled by a small needle valve, and by some diagnostic equipment that checks the flow rate and pressure of the gas into the chamber. The gas flow is directed at the copper cone that forms the moderator. During the moderator growth phase the gas is allowed into the vacuum chamber for about 20-30 minutes. This only occurs after the gate valve separating the source and moderator stage from the rest of the apparatus has been closed, to seal-off this part of the system, and after the ion pump has been switched off. The pressure in the source and moderator chamber, during the growth process, increases from the typical background vacuum (10^{-7} Torr range) up to ~10^{-4} Torr. This latter value is the pressure reached upon equilibrium of two competing processes, the gas being injected into the chamber and the frozen solid Ne accumulating to form the moderator. After the moderator growth is completed, the influx of Ne gas is stopped and the residual gas in this chamber is gradually pumped out of the system. Once the pressure has dropped below a certain threshold, the ion pump can be restarted. At this point the new Ne moderator is ready to be used for the experiments.

The moderated positrons form a continuous low-energy beam with a current of up to 1.6 pA with a 50 mCi source. The measured energy distribution of this beam is approximately Gaussian, with a full width at half maximum in the range ~1.5-2 eV. Note that this spread is somewhat larger than that normally associated with moderating materials like tungsten or nickel (see Section 2.1.2.1 and Zecca, 2002; Hugenschmidt *et al.*, 2002). Nevertheless the moderation efficiency of the neon moderator is about 1%, that is a factor of ~10-25 and ~100-200 higher than that of typical tungsten and nickel moderators, respectively (Mills and Gullikson, 1986; Zecca, 2002). Therefore the slightly wider energy distribution of the positron beam, emitted by neon, is more than compensated for by the considerably larger yield of moderated positrons, compared to tungsten or nickel, for the same

number of incident positrons. The combination of a neon moderator and a ~50 mCi source, in fact, produces a flux of up to ~10^7 positrons per second. However, the beam stability and the operational performance, over time, of a neon moderator is significantly more limited compared to those of the tungsten and nickel moderators (see Section 2.1.2.1). The number of moderated positrons emitted per second is usually a good indicator for the operational state of a moderator. In the ANU apparatus, this quantity can be easily monitored with a thallium-doped sodium iodide gamma ray detector. That detector is mounted near the gate valve between the source and the trap stage, and it collects the 511 keV photons generated by the annihilation of the moderated positrons when they collide with the chamber walls or when the gate valve is shut. Now, recall that the positron current obtained with a tungsten moderator is stable over periods of a couple of months, while that of a nickel moderator remains stable for a week or so (see Section 2.1.2.1). Under high vacuum conditions the positron current generated by a neon moderator, instead, decays at a rate of about 10% per day. However, when the buffer gases present in the trap diffuse into the source and moderation stage, the neon moderator degrades more quickly and the positron pulse amplitude is typically reduced by 50% within the first 3 days or so since the moderator was grown. As a consequence of this quick loss in beam intensity, a new moderator has to be re-grown, usually every couple of days or so, in order to restore the original positron count rate.

The positrons are initially emitted by the neon moderator with an energy possibly lower than ~10 eV (see Section 2.2.2.2 and Zecca, 2002). However the moderator can be set to a bias potential of up to 100 V, in order to define the desired initial energy of the positron beam. Once the positron beam has been accelerated by this potential difference, it is magnetically guided into the trap.

2.2.2.2 Trap operation and positron beam formation

While the strong magnetic field in the trapping region limits the radial extent of the positron beam, confinement in the axial direction is achieved by driving the positrons into a multi-stage (stepped) electrostatic potential. This potential is generated within the trap and can be appropriately tuned by applying relevant potentials to each of the trap electrodes. Note that the configuration of the electrode potentials changes during the three different phases of the entrapment process. The trap is operated in a fast cycling mode, both to account for the relatively short lifetime of the positrons in the trap and to limit the number of positrons in each pulse. This latter criterion is met in order to avoid saturating the detector. Those operations are attained thanks to a very high slew rate (up to 300 V/μs) characterizing the entire electrical system of the apparatus. In addition, such a high slew rate guarantees that the achievable energy resolution in the pulsed beam is independent of the particular trap operating frequency.

A trap cycle usually consists of three stages: a loading phase, where the incident moderated positrons are accumulated into the trap, a cooling stage, where the positrons thermalize to room temperature via inelastic collisions with the buffer-gases and finally a dumping stage, where the cold positrons,

forming a beam of high intensity and energy resolution, are released from the trap. Each trap stage has a different time duration, which is ~ a few ms for each phase. Thus the total trap time is typically ~13 ms. A schematic diagram representing the different potential configurations of the trap electrodes, during the three stages of a trapping cycle, is shown in Fig. 2.29. This cycle is repeated many times per second, so that a pulsed beam is ultimately formed and can then be used in a scattering experiment.

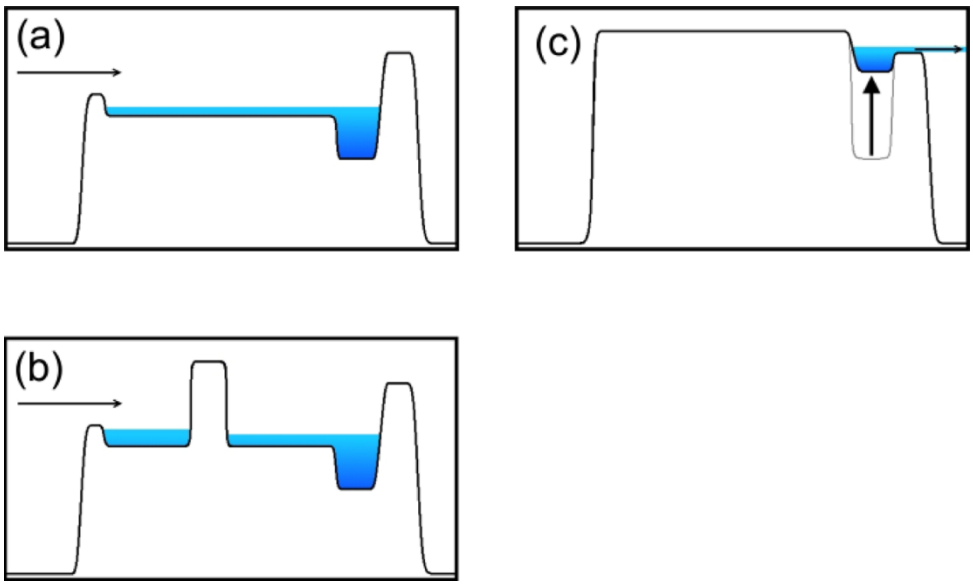

Fig. 2.29. Schematic representation of the potential configurations of the various trap electrodes (1 to 9, from left to right) during the three stages of a typical trapping cycle: (a) loading, (b) cooling and (c) dumping (Sullivan *et al.*, 2008b). The arrow shows the direction of the positrons entering the potential well.

In the loading phase the moderated positrons are magnetically guided into the trap and "fall" into the first of a two-stage potential well (Fig. 2.29a). Spatial confinement of the positrons is achieved on one side of the trap by raising the potential of the first electrode. Note, however, that this potential remains low enough to still allow a significant fraction of the incident moderated positrons to enter the trap (Fig. 2.29a). On the other side the final electrode also acts as a potential barrier, with a voltage typically a few V above the incident positron energy. This is done in order to prevent the moderated positrons passing directly through the trap. The duration of the accumulation/collection stage represents the longest phase in an entire trap cycle.

Trapping occurs through inelastic collisions between the incident positrons and the buffer gases present in the trap. In the initial electrodes, the positrons lose most (~8.3-8.5 eV) of their impact energy (~10 eV) by near-threshold excitation of the $a^1\Pi_g$, $a'^1\Sigma_u^-$ and, to a lesser extent, $w^1\Delta_u$ electronic states of the N_2 molecule and, as a consequence, become trapped

into the potential well. A positron with ~10 eV incident energy can, in fact, excite the singlet ground state ($X^1\Sigma_g^+$) of the N_2 molecule to any one of those three excited states. N_2 turns out to be a particularly effective buffer gas, as the threshold energies of the first two excited states (8.399 eV for $a^1\Pi_g$ and 8.549 eV for $a'^1\Sigma_u^-$; Sullivan *et al.*, 2001b) are below the positronium formation threshold (8.78 eV; Marler and Surko, 2005) and also because the cross section of the $a^1\Pi_g$ state turns on quite sharply at its threshold (Sullivan *et al.*, 2001b). In addition, at the typical incident energy of the incoming positrons, the $a^1\Pi_g$ excitation cross section dominates in magnitude over that for positronium formation. This allows one to limit the positron loss owing to positronium formation in the trap and, at the same time, make the trapping process very efficient. As a result of the energy losses via these inelastic collisions, the positrons end up with a residual energy of ~1 eV in the first well of the trap.

During the cooling stage, the positrons in the second part of the first well, and those in the second well, are isolated from the incoming beam by raising the potential on an intermediate electrode above that for the incident positron energy and the potential barrier produced by the last electrode (Fig. 2.29b). This configuration allows the positrons to further cool, and thus ultimately to become trapped in the bottom of the second potential well. At the same time, it enables positrons to still be collected within the potential well of the first part of the trap. Full thermalisation to room temperature (~40 meV) occurs in the penultimate element of the trap, electrode 8, again through inelastic collisions with buffer gas molecules (Murphy and Surko, 1992; Greaves and Surko, 2000). The inelastic processes responsible for these further energy losses, however, are now different, as the energy of the positron beam is reduced. Note that in this part of the trap the buffer gas CF_4 is also present, in addition to N_2, so that the positrons here lose energy by excitation of the vibrational and rotational modes of both the N_2 (Gianturco and Mukherjee, 1997) and the CF_4 (Gilbert *et al.*, 1999) molecules. However, due to the comparatively much larger vibrational cross sections in CF_4, this molecule is, in principle, nearly two orders of magnitude more effective than N_2 in further cooling the positrons in this stage of the trap. The presence of a small amount of CF_4 here is thus essential to increase the cooling efficiency, by a factor of ~10 as compared to if only N_2 was present (Greaves and Surko, 2000).

The cloud of cold positrons obtained in this manner is used as the reservoir for a beam pulse. A positron pulse is released from the trap, during the dump phase, by appropriately modulating the potentials of the last electrodes. In particular, the bottom of the confining well, i.e. the potential on electrode *E*8, is raised to just above the value of that on electrode *E*9. This defines the transport energy of the positron beam and forces the positrons over the potential barrier thereby causing them to leave the trap, as can be seen in Fig. 2.29(c). In this operation care must be exercised, in order to avoid inducing heating of the trapped and cooled positrons, so that their energy distribution is maintained as narrow as possible. This is achieved in practice by carefully, i.e. relatively slowly, raising the potential on electrode

E8 as a function of time, as a quick ejection might jeopardize the energy resolution of the beam.

By repeating this trapping cycle many times per second, a pulsed beam of several microseconds duration (typically ~2 μs) is generated by the trap at a frequency of 80-300 Hz. Under these circumstances a number of positrons ranging from 100 up to 500, are emitted in each individual pulse. The energy width of the beam created with this procedure is well-defined (Gilbert *et al.*, 1997), and should be about, or even slightly lower than, the temperature of the cooled positron cloud (ΔE ~25-40 meV). However, in practice the narrowest energy spread typically achieved at ANU is 40-60 meV. In any event, the pulsed positron beam is now ready to be used for the scattering experiments.

The efficiency of the present trap, i.e. the ratio of the number of positrons "caught" by the trap to that of the incoming moderated positrons, is essentially determined by two parameters: the number of positrons that can be trapped and the efficiency of the trap cycle. The trapping efficiency (trap throughput) is optimised by tuning the various operational parameters, like the duration of the different trap stages. The overall efficiency of the entire trapping process is usually ~5%.

2.2.2.3 Preparation of the target sample and scattering in the cell

Initially, prior to starting an experiment, the sample of interest has to be put into a suitable container. This is then connected to the gas handling system that feeds the scattering cell, with the target gas or vapour. Only high-purity targets are typically used for studies undertaken with the ANU apparatus. As noted in our previous description of the Trento apparatus, if the target is gaseous at room temperature, then the gas bottle is coupled to a pressure reducing valve and directly connected to the system. In contrast, if the target is a volatile liquid at room temperature, then the sample is first degassed through several freeze, pump and thaw cycles before it is used for the desired experiment.

We noted in Section 2.2.2.2 that the spread in $E_{\|}$ of the positron beam gets larger, in traversing from the moderation to the trap stage. This observation is also true for the spatial distribution of the beam. However, in this case the expansion of the trapped positrons with respect to the moderated beam is mainly due to cross-field transport in the trapping process. The spatial distribution of the beam depends on the strength of the magnetic fields. In a ~530 G magnetic field the diameter of the trapped beam pulse is ~12 mm, as compared to the ~3 mm width of the incident moderated beam. As the size of the scattering cell apertures is 5 mm in diameter, the apertures are clearly too small to transmit the entire positron pulse. As a consequence, only a portion of the incident beam is transmitted (usually about 40-50% of the beam intensity).

During a cross section measurement the target gas is injected into the scattering cell. It subsequently exits the cell through the two apertures, where it is ultimately pumped out of the system by the two adjacent

turbomolecular pumps. The gas is admitted from the target sample into the scattering cell via a manual leak valve. The pressure in the scattering cell is carefully set so that the number of positron scattering events in the interaction region is limited to a maximum of 10% of the unscattered beam. This is a general precaution to make sure that the measurements are undertaken within a pressure regime where multiple scattering events are minimised. This can also be checked by measuring the cross sections as a function of the pressure, in order to make sure that they are independent of each other. For the typical targets investigated within this thesis, the pressure in the scattering cell is generally within the range 0.1-1 mTorr.

Positrons scattered in the forward direction, i.e. with a scattering angle $\theta < 90°$, as well as the unscattered positrons, exit the scattering cell and are then transmitted to the retarding potential analyser. Positrons scattered in the backward hemisphere ($90° < \theta < 180°$), instead, exit the cell from the entrance aperture, are reflected back by the potential wall at the third stage of the buffer-gas trap, pass through the cell again and finally are guided into the RPA. We can assume (to first order) that during this second run through the cell the positrons do not collide again with the target molecules, that is we neglect any further scattering events. The positrons scattered through a small angular range about 90° also have a probability of rescattering or being lost from the beam, as their path length inside the gas cell after the scattering event is considerably increased compared to the particles scattered to lower angles. Positrons that form positronium annihilate within the cell, as they are no longer magnetically confined, and thus are removed from the beam.

2.2.2.4 Beam energy calibration and analysis

The positron energy during the interaction with the target (E_{scatt}) is given by the difference between the potential on the last electrode in the trap (V_{trap}), which defines the mean transport energy of the beam, and the scattering cell potential (V_{cell}) (see Fig. 2.30):

$$E_{scatt} = e\left(V_{trap} - V_{cell}\right). \tag{2.30}$$

The collisional energy can be tuned from ~0.5 to 200 eV. However, as in a "real" experiment there can be an offset between the applied and the effective potential on the elements and this offset can be relatively large (10-100 meV), this is not the most accurate way to determine the scattering energy. An RPA cut-off measurement of the beam, in the absence of the target gas in the system, is of help in this regard. In fact, the beam energy is defined by the cut-off point, i.e. the potential at which half of the beam is transmitted or blocked. The zero energy of the scattering cell corresponds to the potential at which the gas cell cuts off the positron beam and this can be precisely established with a RPA analysis. The energy scale is then defined relative to the cut-off position of the beam. The peak of the derivative of the RPA cut-off curve indicates the position of the zero of the energy scale, whereas the full width at half maximum of the derivative function provides

an estimate of the energy resolution of the beam (Gilbert *et al.*, 1997). The accuracy that is typically achievable in this procedure results in an uncertainty in the energy scale of ±20 meV at most. The energy distribution of the positron beam was typically found to vary from 40 to around 80 meV (FWHM).

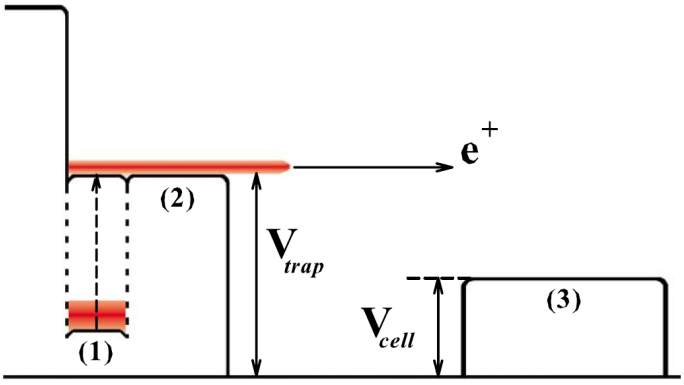

Fig. 2.30. Schematic representation of the potentials applied during the various stages of the apparatus: (1) the dump stage and (2) the exit gate of the trap with a potential V_{trap}, and (3) the scattering cell at a potential V_{cell} (Caradonna *et al.*, 2009).

A typical example of such an RPA cut-off curve, for a scattering energy of 25 eV, is shown in Fig. 2.31. In this figure the experimental amplitude of the positron pulse area as a function of the RPA potential is given between 25.0 and 25.3 V with 0.01 V steps. Also shown in Fig. 2.31 is a Gaussian fit to the RPA curve derivative. In this particular case we find that the energy zero corresponds to a retarding potential of 25.14 V and that the energy width of the positron beam is 63 meV.

An RPA energy spectrum of the beam after the positrons have interacted with the target (i.e. in the presence of the target gas in the system) is very important, as it contains the information that ultimately allows a calculation for the scattering cross section of interest (Sullivan *et al.*, 2001b). In fact, we note that electrodes having a cylindrical symmetry with their axis parallel to that of the magnetic field can only couple with the $E_{\parallel}$ component of the positron beam. Hence, when performing an RPA analysis, the obtained spectrum is actually a measurement of $E_{\parallel}$ only. Initially we can assume that the positrons have energy only in the parallel direction. However, when undergoing a collision with a target atom or molecule in the scattering cell, they can elastically be scattered to some angle and so part of their $E_{\parallel}$ is transferred into the perpendicular direction of motion. As the RPA is exclusively sensitive to $E_{\parallel}$, only those positrons with an energy such that $E_{\parallel}/e$ is above the retarding potential can pass through, whereas any positrons that have been elastically scattered to some angle, and consequently have lost some $E_{\parallel}$, are rejected. Therefore, an RPA energy spectrum contains information about the redistribution of the positron beam

energy into the $E_{\parallel}$ and $E_{\perp}$ components, which is in turn related to the angular distribution of the positrons after the scattering events. In summary, an RPA measurement can be interpreted in terms of the positron scattering cross sections.

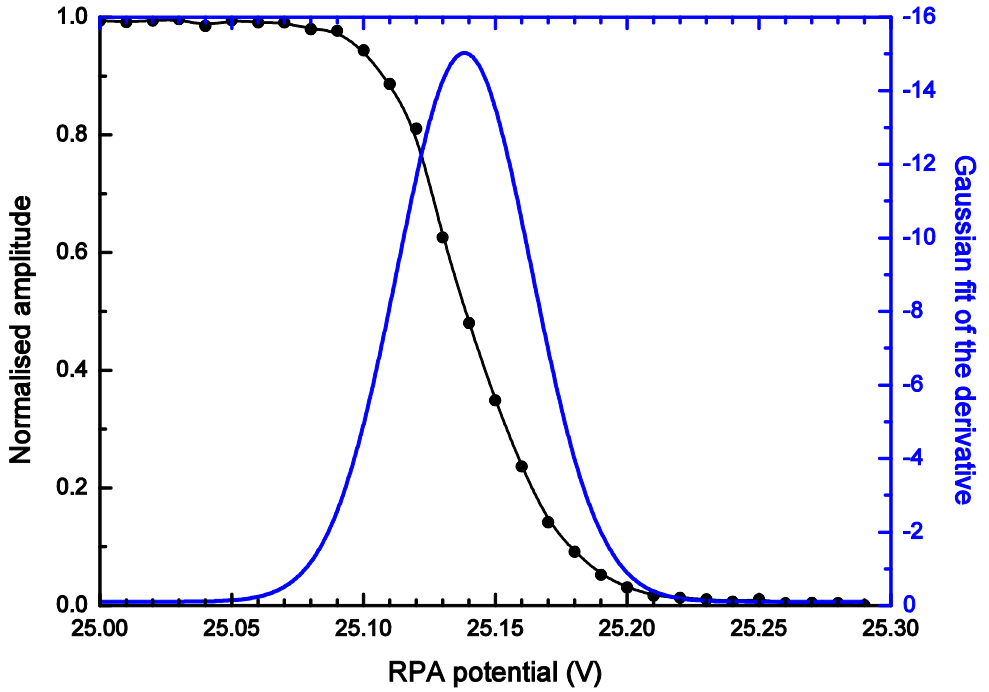

Fig. 2.31. A typical RPA cut-off curve for a nominal scattering energy of 25 eV. The normalized amplitude of the positron pulse area is shown as a function of the retarding potential of the RPA element. Also shown is a Gaussian fit to the derivative of the RPA data points, which represents the energy distribution of the beam. No target gas is present in the scattering cell.

The positrons can also lose some of their total energy during a collision with a target atom or molecule in the interaction region, if inelastic processes are energetically allowed (Sullivan *et al.*, 2002). As we will see later on more in detail, by taking advantage of the fact that the quantity $E_{\perp}/B$ is an adiabatic invariant in a magnetic field, it is possible to separate the elastic scattering channel from the inelastic channels with an RPA measurement under particularly favourable experimental conditions. This situation can be achieved by suitably varying the intensity of the magnetic fields between the scattering and the RPA region. An increase or decrease of the magnetic field intensity can, in fact, enhance or reduce the $E_{\parallel}$ distribution, respectively.

2.2.3 Data analysis and correction

Before describing the procedures for the analysis and computation of the various cross sections of interest, from the raw data of an RPA

measurement, we briefly review the theoretical basis underlying positron scattering measurements in a strong magnetic field. Then we outline the instrumental effects that may affect the cross section measurements. Finally, we discuss the overall uncertainties on the data that typically affect the measurements taken with the ANU beamline.

2.2.3.1 Positron scattering in a strong magnetic field

As we have qualitatively observed in Section 2.2.2.4, the scattering cross sections can be calculated with the present spectrometer by starting from an RPA cut-off measurement in the presence of the target gas in the interaction region and by taking advantage of the properties of the beam when the scattering occurs in a strong magnetic field. In order to give a quantitative description of this approach, we refer in the rest of this section to the techniques developed by the San Diego group and thoroughly explained in the paper by Sullivan *et al.* (2002). In that paper the differential cross section σ, relative to the process of an incident beam of intensity I_{0R} and initial energy E scattering with intensity I and energy E' into an angle θ, is given by:

$$\frac{d^2I}{dE'd\Omega}(E,E',\Omega) = nlI_{0R}\frac{d^2\sigma}{dE'd\Omega}(E,E',\Omega), \tag{2.31}$$

where $d\Omega = 2\pi \sin\theta d\theta$ is the solid angle corresponding to the elevation angle θ, n is the target number density and l is the positron path length.

We noted earlier in this Chapter that, in general, in a uniform and constant magnetic field B a charged particle moves in a spiral through the field with a well-defined gyroradius (Eq. 2.22). Therefore, the energy E of the particle can be split into the components parallel and perpendicular to the field ($E_\parallel$ and $E_\perp$, respectively). In the incident beam the energy E of a particle is almost entirely in the parallel direction of motion, i.e. $E_\perp \ll E_\parallel \simeq E$. However, after a collision with a target molecule, the particle is scattered to some angle θ and hence its energy E' is redistributed between $E_\parallel$ and $E_\perp$, if the collision is purely elastic. If inelastic processes are energetically allowed, then additionally the internal energy E_{ex} of the target molecule comes into play, so that $E' = E'_\parallel + E'_\perp + E_{ex}$. In addition, positronium formation is also possible above the corresponding threshold.

Recall that in the present experimental configuration the intensity of the magnetic fields in the scattering region (B_C) and in the RPA region (B_A) are independently adjustable. Now, let us define M as the "beach ratio" between the magnetic fields in these two sections of the apparatus:

$$M = B_C/B_A\,. \tag{2.32}$$

Note that in a slowly varying magnetic field the magnetic moment of a charged particle $(E_\perp/B)$ is an adiabatic invariant. As a result, a change in the magnetic field intensity will change the values of $E'_\parallel$ and $E'_\perp$. In particular, a reduction in the magnetic field intensities by an amount equal

to $M > 1$ (i.e. $B_A < B_C$) causes $E'_\perp$ to decrease by the same factor M and transfers the energy back into $E'_\parallel$. The related energy spread is also correspondingly reduced by M. As the RPA measures only the $E'_\parallel$ component of the beam energy, for $M \gg 1$ an RPA measurement provides a direct measure of the total energy distribution of the scattered particles.

As, in general, an RPA curve is the standard measurement taken in an experiment, it is more useful to rewrite Eq. (2.31) in terms of the quantity $E'_\parallel$ that is actually measured by the RPA. In doing so, one obtains the following expression:

$$\left.\frac{d\sigma}{dE'_\parallel}\right|_{E_C} = -\frac{1}{nlI_{0R}}\frac{dI_C}{dE_c}\left(E, E'_\parallel\right). \tag{2.33}$$

Eq. (2.33) is a very important relation, because it relates the differential cross section with respect to $E'_\parallel$ to an RPA measurement. The differential cross section is, in fact, essentially determined by the derivative of the transmitted positron beam intensity I_C with respect to the scattering energy $E_C = eV_C$ at the cut-off potential V_C. From Eq. (2.33) it is then possible to derive the expressions of the cross sections for all the scattering channels in the single scattering regime.

2.2.3.2 Calculation of the cross sections

The basis of all linear transmission experiments is the Beer-Lambert attenuation law. An RPA cut-off curve is effectively an empirical measurement of the attenuation of the positron beam intensity for a given scattering energy and can be related to the desired scattering cross section (see Section 2.2.3.1), provided that the target pressure and the scattering path length are known. The different physical processes that can take place during the scattering events correspond to various fractions of the incident beam, which are transmitted through the RPA at some values of the retarding potential. Let us see how this information can be used to calculate the cross sections of the corresponding scattering channels.

A schematic representation of a typical RPA profile for a given collisional energy of 60 eV is shown in Fig. 2.32. The normalised transmitted positron beam intensity is measured as a function of the retarding potential when the target gas is admitted into the scattering cell. I_{0R} is the intensity of the incident beam measured when the energy in the scattering cell is below the positronium formation threshold and with the RPA set to allow the transmission of all scattered and unscattered positrons (i.e. set to a zero retarding potential). I_0 is the transmitted intensity after a portion of beam has undergone positronium formation inside the scattering cell and is consequently lost. Hence, the difference between I_{0R} and I_0 reflects the fraction of the incident positrons that form positronium. I_0 is again measured by setting the retarding potential to 0 V, however, only when the scattering energy is higher than the positronium formation threshold. If the scattering energy is lower than the positronium formation threshold, then I_{0R} coincides with I_0. I_0' is the transmitted intensity measured

just before the onset of any scattering process (taking into account both inelastic and angular scattering) and is measured with the RPA set to retard any positrons with a parallel energy component smaller than the scattering energy. If I_0 and I_0' are different, then it means that some background scattering has occurred outside the scattering cell in the positron path between the scattering cell and the RPA element. If this is the case, then this discrepancy is taken into account in the analysis of the raw data in order to correctly compute the scattering cross sections and is also treated as an additional contribution to the overall uncertainties on the cross section values. I_m is the residual beam intensity after the elastic and inelastic scattering events, with the target gas, have occurred within the scattering cell and have caused the loss of a portion of the parallel positron energy. Hence, I_m represents a measure of the unscattered portion of the incident beam. The position of I_m is established by setting the retarding potential to a small fixed voltage offset ΔV from the cut-off potential V_C. Finally, I_b is a measure of the intensity above the cut-off potential V_C. I_b is used to estimate the background noise of the positron detection system and is properly taken into account when scaling the ratios between the various beam intensities.

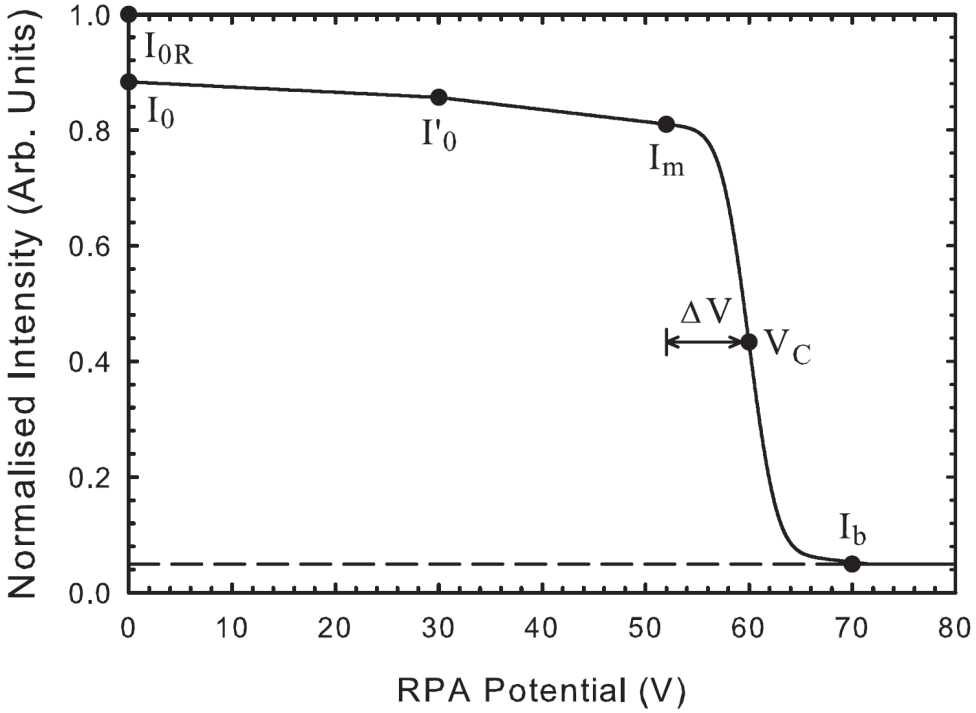

Fig. 2.32. Schematic of the typical profile for a retarding potential analysis of the positron beam with the target present in the scattering cell and for a given collisional energy of 60 eV (Jones *et al.*, 2011). See text for further details.

This interpretation of a typical RPA curve, in terms of the various scattering processes responsible for the loss of a part of the transmitted positron beam intensity, as defined in Fig. 2.32, enables us to calculate the

cross sections for the various scattering channels we are interested in. In fact, as we will see in more detail in the following subsections, the various integral cross sections can be simply expressed as a function of the fractions of the measured transmitted intensities.

2.2.3.2.1 Total cross section

The total cross section σ_T can be calculated from the measurements of the full incident positron intensity (I_{0R}) and the unscattered transmitted intensity (I_m), by using the Beer-Lambert law:

$$\sigma_T = \frac{1}{nl}\ln\left(\frac{I_{0R}}{I_m}\right). \tag{2.34}$$

In Eq. (2.34) n is the target number density and l is the particles path length. The total cross section is given by the sum of all the partial cross sections for the open channels:

$$\sigma_T = \sigma_{el} + \sigma_{Ps} + \sigma_{ex} + \sigma_{ion} + \ \ldots\ . \tag{2.35}$$

The integral cross sections σ_X, for each scattering channel (elastic, inelastic and positronium formation), can be calculated by partitioning the total cross section into the components corresponding to the individual scattering channels. This is simply done by scaling σ_T by the fraction of the scattering related to that particular process:

$$\sigma_X = R_X \times \sigma_T. \tag{2.36}$$

In Eq. (2.36) R_X is the partitioning ratio corresponding to the relevant portion of the total measured intensity attenuation attributable to that specific scattering process.

2.2.3.2.2 Differential cross sections

For each integral cross section information about the scattering angular distribution can also be obtained. In the following we discuss differential cross sections in the case of elastic scattering only (Gilbert *et al.*, 2000). However, the same approach can be used to derive a similar expression for inelastic scattering.

By multiplying both sides of Eq. (2.33) by $dE_\parallel/d\Omega$, we can rewrite it in the following way:

$$\frac{d\sigma}{d\Omega} = -\frac{1}{nlI_{0R}}\left(\frac{dI_C(E)}{dE_\parallel}\right)\left(\frac{dE_\parallel}{d\Omega}\right). \tag{2.37}$$

After deriving an explicit expression for $dE_\parallel/d\Omega$ as a function of E and θ, from simple geometry and energy considerations, and by substituting that into Eq. (2.37), one obtains:

$$\frac{d\sigma}{d\Omega} = \frac{\sqrt{EE_{\parallel}}}{\pi n l I_{0R}} \left(\frac{dI_C(E)}{dE_{\parallel}} \right). \tag{2.38}$$

Hence, a differential cross section can be easily calculated with an RPA measurement of the transmitted current I_C as a function of $E_{\parallel}$.

In an elastic scattering process, the maximum energy that can be transferred from $E_{\parallel}$ to $E'_{\perp}$ is of course the incident beam total energy E. Thus the information about the elastic angular scattering is contained in a region of retarding potential equal to E/e down from the cut-off V_C, and there is a direct correspondence between the scattering angle θ and $E'_{\parallel}$, or equivalently the retarding potential:

$$\theta = \cos^{-1} \sqrt{E'_{\parallel}/E}\,. \tag{2.39}$$

The scattering angle $\theta = 90°$ (i.e. when $E'_{\parallel} = 0$ and $E'_{\perp} = E$) coincides with the retarding potential $V_C - E/e$, while the $\theta = 0°$ scattering angle (i.e. when $E'_{\parallel} = E$ and $E'_{\perp} = 0$) corresponds to the cut-off voltage point V_C. Positrons scattered into the backward hemisphere ($90° < \theta < 180°$) are reflected back into the forward direction by the potential barrier of the last stage of the trap, and thus contribute to the differential cross section measured at a forward angle. In particular, a cross sections at any forward angle θ contains also the information of the scattering at an angle $180° - \theta$, so that that the measured differential cross section is actually "folded" around 90°.

Note that as I_m is measured at a small voltage offset ΔV from the cut-off potential V_C, the differential cross section around the scattering angle $\theta = 0°$ is experimentally inaccessible. Hence, only the range $\theta_{min} < \theta < 90°$ can be explored, where θ_{min} corresponds to $V_C - \Delta V$ (i.e. the position of I_m). In terms of the measured differential cross section this experimental issue limits just the angular range that can be investigated. As a result, the magnitude of the measured elastic integral and, therefore, also the total cross section, can be significantly underestimated as compared to its "real" value (see Section 2.2.3.3).

If the extent of the RPA portion containing the information about the angular scattering is determined by the beam energy E, so also is the smallest angle that can be resolved in an elastic differential cross section measurement. However, the latter also depends on the energy resolution of the positron beam. The angular resolution $\delta\theta$ is in fact given by (Sullivan *et al.*, 2002):

$$\delta\theta = \frac{\delta E'_{\parallel}}{2\sqrt{EE'_{\parallel} - E'^{2}_{\parallel}}}, \tag{2.40}$$

where δE is the energy distribution of the beam. The angular resolution clearly changes with the energy and therefore is not the same for different retarding potential values. The best angular resolution occurs at the centre of

the RPA range containing the information about the elastic scattering, i.e. at the scattering angle θ = 45°, whereas a poorer angular resolution is found towards the range edges (i.e. $\theta \rightarrow 0°$ and $\theta \rightarrow 90°$). Table 2.8 reports some typical values of the angular resolution for selected positron energies in the case of a beam with an energy resolution of 25 meV. We note that the angular resolution is largest at low energy and decreases with increasing energy.

Table 2.8. The angular resolution achievable in a differential cross section measurement at selected incident positron energies, as calculated with Eq. (2.40), for a beam of resolution ΔE = 25 meV (Sullivan *et al.*, 2002).

Energy (eV)	**$\delta\theta$ (°)**
0.2	7-11
1	1.5-5
10	0.15-1.5

Note that Eq. (2.38) is applicable for the calculation of an elastic differential cross section both below and above any of the inelastic thresholds. However, the experimental method used for the measurements above the threshold of the first inelastic process is slightly different to the case when there is only the elastic scattering. This is a consequence of the need for separating the purely elastic channel from the inelastic ones, in order to be able to make a measurement of a purely elastic differential cross section. In the case of a molecular target, if we neglect rotations and vibrations, whose contribution is expected to be negligible (Sullivan *et al.*, 2002), the lowest inelastic threshold corresponds to the first electronic excited state of the target in question. Positronium formation is an inelastic channel, however, the positrons undergoing this process are removed from the transmitted beam and so are not ultimately detected. Direct ionisation is another inelastic process that becomes viable at higher energy, and so that also needs to be taken into account when performing elastic differential cross sections above the first ionisation potential.

In the case where only elastic scattering is present, $E = E' = E'_{\parallel} + E'_{\perp}$. However, at energies above the first electronic excitation threshold, i.e. where also inelastic scattering is energetically allowed, $E \neq E' = E'_{\parallel} + E'_{\perp} + E_{ex}$, as part of the energy lost by $E_{\parallel}$ is transferred not only into $E'_{\perp}$ but also into the excited state E_{ex}. As a consequence, in the latter case there is no longer the direct correspondence between $E'_{\parallel}$ (or the retarding potential) and θ in an RPA measurement. In order to obviate this issue, the beach ratio is changed to an appropriately chosen value of $M > 1$. In this way it is possible to split up the $E_{\parallel}$ losses, due to various inelastic scattering events, from those simply originating from the transfer of energy from $E_{\parallel}$ into $E'_{\perp}$ as a result of angular elastic scattering. Now, in order to effectively achieve the separation of the elastic channel from the inelastic channels, the M value must be properly selected for a given scattering energy E, depending on the energy threshold of the first inelastic process E_{ex}, such that:

$$M \geq E/E_{ex}\,. \tag{2.41}$$

The only significant negative side effect of this technique is a reduction in the angular resolution (see Section 2.2.3.3). This fact must be taken into account when choosing the most appropriate M value.

2.2.3.2.3 Inelastic scattering

We observed in Section 2.2.3.2.2 that in an experiment where inelastic scattering is energetically viable, if the magnitude of the magnetic fields in the interaction region and in the RPA section are different by a factor M, such that $M > 1$, and its value is appropriately chosen, then the separation of the elastic channel from the inelastic ones becomes experimentally feasible. Therefore, it is possible to determine individually the elastic and inelastic integral cross sections. The procedure showing how this is achieved is illustrated in Fig. 2.33.

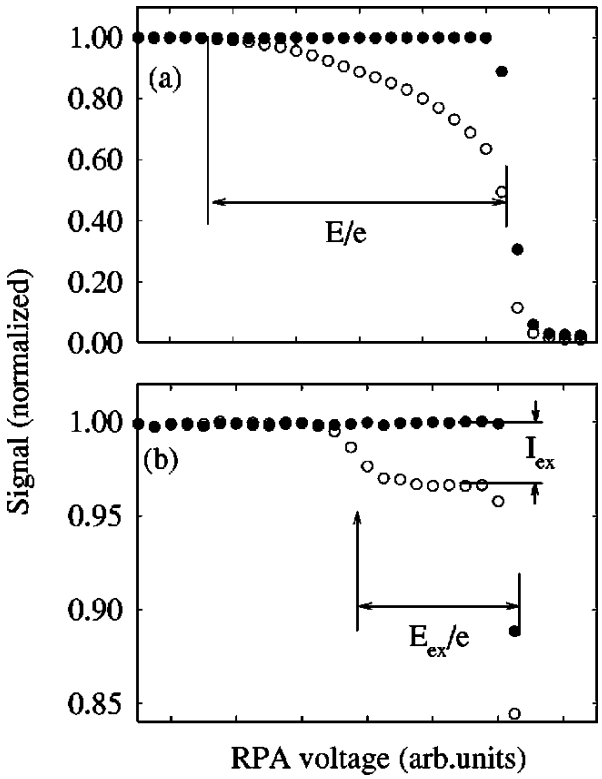

Fig. 2.33. RPA cut-off curves for positrons with incident energy higher than the first inelastic threshold in the absence of the target (full circles) and after scattering from the target (open circles), with (a) M = 1 and (b) M = 35 (Sullivan *et al.*, 2002).

Fig. 2.33 shows some examples of RPA cut-off curves for positrons with incident energy E higher than the first inelastic threshold, in the absence of the target and then after scattering from the target, with two different beach

ratios: (a) $M = 1$ and (b) $M = 35$. Now, if $M = 1$, the information about the angular distribution for the elastic scattering is confined in a region of retarding potential equal to E/e down from the cut-off potential V_C, as we can clearly observe in Fig. 2.33(a). Instead, if $M \gg 1$, the elastic scattering channel is reduced only to a region of the RPA spectrum equal to $\delta \sim E'/(eM)$ below V_C (see Fig. 2.33b), and now the distribution of $E'_{\parallel}$ measured by the RPA depends only on the total energy loss of the positrons in the collision. The inelastic scattering corresponds to the step evident in the RPA profile of Fig. 2.33(b), at a voltage corresponding to E_{ex}/e. The height of this step is given by I_{ex} and is proportional to the integral inelastic cross section σ_{ex} of this inelastic scattering process. Clearly, if more than one inelastic channel is open at some scattering energy E, then the RPA profile in the presence of the target in the interaction region, measured with $M \gg 1$, will show a series of steps arising in correspondence to the respective thresholds of the various inelastic channels. The integral cross section for all inelastic processes will then be determined by the sum of the fractions of transmitted beam I_{ex} of each of these processes.

2.2.3.2.4 Positronium formation cross section

Positronium formation is often referred to as a loss process, as those positrons that form positronium in the cell are ultimately lost to annihilation. In Section 2.2.3.2 we observed that the fraction of the incident beam that is removed from the transmitted beam, owing to positrons undergoing positronium formation, is given by $I_{0R} - I_0$. Therefore the partitioning ratio R_{Ps}, attributable to the positronium formation process, is determined by the following ratio of measured intensities:

$$R_{Ps} = \frac{I_{0R} - I_0}{I_{0R} - I_m}. \tag{2.42}$$

By substituting Eq. (2.42) into Eq. (2.36) we obtain the following expression for the positronium formation cross section σ_{Ps}:

$$\sigma_{Ps} = \frac{I_{0R} - I_0}{I_{0R} - I_m}\sigma_T. \tag{2.43}$$

2.2.3.3 Missing angles and forward angle scattering effects

We have previously observed that there are some angular ranges that are missed in the ANU experiment, owing to some restrictions in the measurement techniques. These missing angles are the ranges $0° < \theta < \theta_{min}$ and $\theta_{max} = 180° - \theta_{min} < \theta < 180°$, corresponding to the fraction of forward-angle elastic scattering that is inaccessible in an RPA measurements and also to the corresponding range in the backward direction (refer to Section 2.2.3.2.2).

As mentioned in Section 2.1.3.4, any experiment based on a linear-transmission technique inevitably suffers from some angular discrimination limitations. In the ANU beamline these originate from the finite energy

resolution of the positron beam. In a total cross section measurement these limitations result in some particles scattered to small angles being able to reach the detector, as if they had not been scattered. These events cause a miscounting (overestimation) of the transmitted current, which in turn leads to an error (underestimation) in the measured cross section. At very low energies, in some particular experimental conditions and for highly polar targets, this effect on the measured cross sections can result in a significant underestimation of the "real" cross section. As a consequence, the forward angle scattering effect should be at least taken into account in the discussion of the results, if not corrected for if that is possible.

The extent of the forward angle scattering effect depends on the angular resolution of the apparatus and the nature of the differential elastic scattering cross section of the target in the forward angle region (Sullivan *et al.*, 2011). If these two parameters are known at each investigated energy, then the measured cross section can be corrected for the forward angle scattering effect. Note that this issue is exclusively a feature of elastic scattering processes for the ANU apparatus, while this is not true for the other experiments limited by geometry. As a consequence, only the elastic integral cross section and the total cross section need to be corrected for this effect, whereas the integral cross sections for positronium formation and the inelastic channels are not affected by this at all.

The critical angle $\theta_{\min}$, below which elastically scattered positrons cannot be distinguished from the incident beam, corresponding to the angular discrimination of the cross section measurement, can be calculated in the following way:

$$\theta_{min} = \sin^{-1}\sqrt{\frac{e\Delta V \cdot M}{E}}, \tag{2.44}$$

where E is the scattering energy, M is the beach ratio, e is the positron charge and ΔV is the offset between the cut-off potential V_C and the potential at which the transmitted beam intensity I_m is measured (see Section 2.2.3.3). In general ΔV is determined empirically from the cut-off measurement. However, as a guiding rule, it usually is $\Delta V \geq 3\sigma$, where σ is one standard deviation of the energy distribution of the positron beam.

We see in Eq. (2.44) that the minimum scattering angle basically depends on the energy resolution of the incident beam and on the beach ratio employed in the measurement. It is also clear from Eq. (2.44) that the discrimination angle decreases with increasing energy, in contrast to what used to happen in earlier conventional experimental setups, where the ability to discriminate against small forward-angle scattering was fundamentally limited only by geometrical aspects. On the opposite, the critical angle $\theta_{\min}$ becomes larger with increasing beach ratio. These qualitative conclusions are quantified in Table 2.9, where the angular discrimination $\theta_{\min}$ in a typical experiment, employing a beam resolution of ΔE = 60 meV and a beach of M = 1, is reported as a function of selected incident positron energies. We note in Table 2.9 that the angular discrimination can be as high

as 61° at very low energy (0.1 eV), but drops to 2° at 60 eV. We further note that these values are slightly lower than the angular discrimination characterising the measurements undertaken with the spectrometer at the University of Trento (Table 2.5), ranging from 71.6° at 0.1 eV to 2.4° at 50 eV. This is due to the present experimental configuration employing magnetic fields that are much stronger than that used in the Trento apparatus, so that virtually all unscattered and scattered positrons are carried through to the detector. A second reason is that there is no geometrical limitation to the angular discrimination in the ANU apparatus, as compared to the Trento spectrometer.

Table 2.9. The angular discrimination at selected incident positron energies, for a typical cross section measurement undertaken with the ANU beamline, as estimated using Eq. (2.44) with $M = 1$ and for a beam of energy resolution $\Delta E = 60$ meV.

Energy (eV)	θ_{min} (°)	Energy (eV)	θ_{min} (°)	Energy (eV)	θ_{min} (°)
0.1	61.0	1	16.0	10	5.0
0.2	38.2	2	11.3	20	3.5
0.3	30.3	3	9.2	30	2.9
0.4	25.9	4	7.9	40	2.5
0.5	23.0	5	7.1	50	2.2
0.6	20.9	6	6.5	60	2.0
0.7	19.3	7	6.0		
0.8	18.0	8	5.6		
0.9	16.9	9	5.3		

As a consequence of the angular discrimination decreasing with the impact energy, the forward angle scattering correction will be largest at the lowest energies and become smaller as the energy increases. The precise extent of this correction, though, depends on the nature of the elastic differential cross section of the target in question and therefore is not uniquely determined, but is species-dependent. Unfortunately, positron elastic differential cross sections for the species of interest, either theoretical or experimental, are typically unavailable at all relevant energies. Even in the very few cases in which these are available, the accord between theory and experiment is still not good enough at all energies, to reliably allow employing that data in order to calculate the forward angle scattering correction by following the procedure outlined in Section 2.1.3.4. Therefore this effect cannot be corrected for at this stage and so the measured elastic integral and total cross sections presented in this thesis represent only a lower bound on the true cross sections. We anticipate, however, that this correction would be largest for polar molecules, as the elastic differential cross section for those species is expected to be more forward-peaked, especially at the lowest energies. Large values of the dipole polarisability and/or permanent dipole moment, in fact, typically result in an overall attractive interaction between the incident positron and the target, that can

significantly increase the probability of scattering particularly in the forward direction.

Most of the total and elastic integral cross sections published in the literature, so far, have not been corrected for forward angle scattering effects (Sullivan *et al.*, 2011). This is almost certainly because of the lack of accurate differential cross sections. However, in some cases corrections have been applied (see for instance Hamada and Sueoka, 1994 and Kimura *et al.*, 2000) to account for this effect. The ANU group has recently corrected some of their cross section measurements (on a few targets) for the forward angle scattering effect, by employing their estimates of the angular discrimination affecting their measurements together with the calculated elastic differential cross sections for those targets (see Section 2.1.3.4). In doing so they found that correction can be as large as 67%, at very low energy, for water (Makochekanwa *et al.*, 2009) and that it becomes smaller at higher energies. Although the forward angle scattering correction turned out to vary significantly from target to target, it was found to be generally smaller for other less polar targets. This demonstrates how significant the forward angle scattering effect can be, especially at the lowest incident energies.

The ANU beamline represents a versatile apparatus for investigating the forward angle scattering effects on the measured total and elastic integral cross sections, since it allows one to arbitrarily select the angular discrimination of the desired experiment (although with an upper limit). This can be achieved, for instance, by varying the intensity of the magnetic field in the RPA section of the beamline, so that the beach ratio is increased to $M > 1$ and, as a result, the angular discrimination becomes somewhat larger (see Eq. 2.44). Therefore, by suitably selecting the M value, it is possible to obtain the desired angular discrimination. As a more precise alternative, one can just select a different value of the RPA cut-off at which the measurement at a given scattering energy is performed. By doing so, the ANU group (Sullivan *et al.*, 2011) found that their cross section results for argon and xenon could be adjusted to match the early measurements of the Detroit group (Kauppila *et al.*, 1976; Dababneh *et al.*, 1980), on those same species, provided that the contribution of the forward 20° of scattering at each energy was removed from the ANU measurement. This was achieved by deliberately degrading their angular discrimination. Note that the stated angular discrimination of the Detroit apparatus is precisely 20° at 2 eV (Kwan *et al.*, 1984). In other words, those early measurements of the Detroit group would agree with the most recent ANU results, if the Detroit data was corrected for a 20° angular discrimination effect at each energy. This result indicates that those older measurements were likely affected by a fairly large forward angle scattering effect, leading to a significant underestimation of the cross sections compared to the more recent measurements.

2.2.3.4 Background scattering

Background scattering of the positrons in the beam can occur in their path from the trap, where they are emitted, to the RPA, where they are

finally energy-analysed in order to ultimately calculate the relevant scattering cross sections. Background scattering takes place mainly between the trap and the scattering cell, owing to the residual presence of the buffer gases diffusing from the trap, and between the scattering cell and the RPA, where some amount of target gas spreads out from the scattering cell. At least in the first case, though, the implementation of the first small RPA element before the scattering cell helps to reduce this effect, by rejecting the positrons that have undergone background scattering before entering the interaction region.

The difference in intensity between I_0 and I_0' is a measure for the extent of the background scattering effect, so that it can be taken into account and eventually corrected for when analysing the RPA profile and computing the cross sections of interest from it.

2.2.3.5 Thermal transpiration

We observed in Section 2.2.1.3 that the target pressure in the scattering cell is measured by a MKS model 690A Baratron capacitance manometer operated at 45 °C, in order to continuously monitor the pressure. As the scattering cell temperature is typically maintained at a temperature of ~30 °C, which is different from the gauge temperature, the pressure readings need to be corrected for the thermal transpiration effect. This correction is calculated according to the model of Takaishi and Sensui (1963) that has already been described in Section 2.1.3.2. Therefore, we do not repeat those details here again, except to note that in this experimental configuration the tube connecting the cell to the manometer has a diameter of 4 mm. The thermal transpiration correction to the pressure readings typically results in an increase of the measured cross section by +3%, over the entire energy range of the measurements.

2.2.3.6 Overall uncertainties

The total uncertainties on the cross sections measured with the ANU apparatus are formed from the contribution of the individual error components. The main contribution to the absolute errors at most energies is the statistical uncertainty in the measured positron beam intensity. Those statistical errors typically vary between 3% and 5% for the total, elastic and inelastic integral and positronium formation cross sections, whereas for the elastic differential cross sections they can be significantly larger in some cases (>10%).

With respect to sources of systematic error, like thermal transpiration and the uncertainty in its correction, they have in general been accounted for. Consistency checks, for instance, are usually undertaken for each measurement by overlaying the results in the overlapping energy range in order to check for any potential systematic source of discrepancy. The largest source of systematic uncertainty is typically the zero drift in the capacitance manometer used for pressure measurements. This effect is responsible for an uncertainty in the total cross section on the order of a few percent, but in particular cases can be as large as 10%. Owing to the strong

intensity of the magnetic fields employed in this experimental setup, the gyroradius of the positrons moving in the magnetic field is very small. Therefore, the correction for the increased effective positron path length in the interaction region is estimated to be negligible (~1% at 1 eV scattering energy and smaller than that at higher energies) and is generally not applied to the data. Another possible source of systematic error stems from the pressure measurements accuracy. As the manometer used for these readings is a high-accuracy gauge, the related uncertainty is possibly smaller than 0.1%. Pressure end effects, due to the finite size of the scattering cell apertures, are minimised by employing small apertures. Overall, systematic effects typically account for an uncertainty of less than 5%.

In the end, the total uncertainties on the measurement results obtained with the ANU spectrometer are usually in the range 5-7%, and are 10% at most for the total, elastic and inelastic integral and positronium formation cross sections. However, for the elastic angular distributions the absolute errors are typically between 7% and 15%, although in some cases they can be significantly larger.